Preparation and Characterization of Components for Intermediate Temperature Fuel Cells And Electrolyzers

Jensen, Annemette Hindhede; Bjerrum, Niels J.; Christensen, Erik; Li, Qingfeng; Barner, Jens H. Von

Publication date:
2014

Document Version
Publisher's PDF, also known as Version of record

Preparation and Characterization of Components for Intermediate Temperature Fuel Cells and Electrolyzers

PhD Thesis

Annemette Hindhede Jensen

Kgs. Lyngby, August 2014

This thesis was submitted in partial fulfillment of the requirements for the degree of Doctor of Philosophy

Author:
Annemette Hindhede Jensen

Supervisor:
Professor Niels J. Bjerrum
Co-supervisors:
Senior Researcher Erik Christensen
Associate Professor Qingfeng Li
Associate Professor Jens H. von Barner

This work has received financial support from the Danish National Research Foundation (the PROCON center).

Proton Conductors Group
Department of Energy Conversion and Storage
Technical University of Denmark
Kemitorvet building 207
2800 Kgs. Lyngby
Denmark

www.pro.ecs.dtu.dk
Tel:(+45) 45252312
Fax: (+45) 45883136
E-mail: ahije@dtu.dk

Abstract

The intermediate temperature region for fuel cells (200-400°C) is of interest as it may combine advantages from low and high temperature technologies. Increasing the temperature above what is used in polymer electrolyte membrane (PEM) fuel cells enhances the catalyst kinetics, and therefore it might become possible to use non-noble metal catalysts. On the other hand, the temperature is low enough for a wide range of materials to be used as construction materials.

In this work a set-up was built and fuel cell hardware was made for demonstration of fuel cells for the intermediate temperature range. For the electrodes, carbon cloth and carbon paper were tested as gas diffusion layers with different catalytic compositions, and of the two, carbon paper with a platinum loading of 7 mg cm^{-2} had the better performance. However, carbon is unstable at the conditions in the fuel cell cathode and other materials must be sought for. It was attempted to use stainless steel (316L), this however corroded and therefore a protective tantalum coating was applied. The tantalum coatings were found to be corrosion resistant and furthermore provided extremely low interfacial contact resistances of only 1.3 mΩ cm^2.

From a literature review it was found that the most promising results for this temperature range have been performed using cesium dihydrogen phosphate (CsH_2PO_4) electrolytes. CsH_2PO_4 undergoes a phase transition at around 230°C, with a rise in conductivity from 8.5 x 10^{-6} at 223°C to 1.8 x 10^{-2} S cm^{-1} at 233°C this is called superprotonic. This electrolyte as well as other electrolytes for this temperature range, however, suffers from poor mechanical properties, and stable fuel cell performance had only been achieved by use of thick electrolytes. Furthermore to maintain high conductivity of the electrolyte, a high level of humidification was necessary.

Composites with CsH_2PO_4 were made to improve the properties of the electrolyte material. Composites in formation with mechanically strong materials including ZrO_2, TiO_2 and $NdPO_4{\cdot}0.5H_2O$ improved the densification of the electrolyte, which further resulted in improved stability of the fuel cell. Open circuit voltages (OCVs) using such fuel cells were found to be high, above 0.9 V, and stable up to 250°C.

Composite formation with ZrO_2 furthermore resulted in increased conductivity at higher temperatures probably due to the physical stabilization of the high conducting phase. At 250°C the cell was stable for more than 60 hours with a partial pressure of water of only 0.12 atm, and it was operational up to 275°C, where the fuel cell using pure CsH_2PO_4 no longer performed.

When CsH_2PO_4 was used in composite with $NdPO_4{\cdot}0.5H_2O$ there were indications of a new phase formed, $CsH_5(PO4)_2$, which has been reported to have high conductivity from 150°C. The mechanism behind an increase in conductivity for the CsH_2PO_4/$NdPO_4{\cdot}0.5H_2O$ of

several orders of magnitude was not fully clarified. Using an $29CsH_2PO_4/71NdPO_4{\cdot}H_2O$ electrolyte enabled fuel cell performance measurements up to 285°C, where the highest performance was recorded. At this temperature current and power densities were found to be 117 mA cm^{-2} and 27.7 mW cm^{-2}, respectively.
Composite formation with melamine cyanurate resulted in increased conductivity in the entire temperature interval measured *i.e.* from 120°C to 260°C. A conductivity as high as 0.18 S cm^{-1} was measured for a $90CsH_2PO_4$/10melamine cyanurate composite at 250°C. Good mechanical properties were furthermore observed for the composites.

Within the research project a screening was made in order to search for new electrolytes. From this screening niobium and bismuth phosphates were found to have high conductivities (>10^{-2} S cm^{-1}) with reasonable stability, and it was therefore attempted to fabricate electrochemical cells from these. The pure phosphates were however suffering from poor mechanical stability and therefore polybenzimidazole (PBI) was added. By adding high amounts of PBI stable OCVs were achieved, these remained stable for around 10 and 70 hours for niobium and bismuth phosphates, respectively. At high temperatures, however, the OCVs were found to drop, at 200°C the OCVs were below 0.9 V.

Tungsten carbide was evaluated as a non-noble catalyst for the hydrogen evolution and oxidation reactions. Tungsten carbides were prepared in different ways in order to achieve higher surface areas compared to the very low surface area of the commercial carbide which was too low to be quantified. By preparing the carbide from WO_3 (WC-mWO_3) which had been prepared by use of a mesoporous silica template by carburization with methane at 900°C for 3 hours, a surface area of 6 m^2 g^{-1} was measured. By introducing an extra synthesis step by first converting the WO_3 into W_2N which was then converted into WC (WC-mW_2N) a higher surface area of 18 m^2 g^{-1} was measured.
The use of methane *versus* ethane as carburizing agents were investigated, by carburizing commercial WO_3 with both agents under the same conditions. From carburization with methane no surface area could be quantified, while the carburization with ethane resulted in a carbide (WC-ethane) with a surface area of 12 m^2 g^{-1}. An additional tungsten carbide (WC-05-VN) with a BET area of 31 m^2 g^{-1} was used for comparison.
Hydrogen evolution activities for the carbides were measured in phosphoric acid at 185°C and -100 mV. It was found that apart from WC-mW_2N, the activities were increasing with surface area, this deviation may be due to an amorphous carbon surface layer. Activities were found as 1.5, 2.07, 10.7 and 18.73 A g^{-1} for WC-mWO_3, WC-mW_2N, WC-ethane and WC-05-VN, respectively.
The carbides were furthermore investigated as fuel cell anode catalysts. The best performances were achieved at the highest temperature measured *i.e.* 270°C where power densities of 2.7, 3.1, 7.4 and 8.2 mW cm^{-2} for WC-mW_2N, WC-mWO_3, WC-05-VN and WC-ethane, respectively, using CsH_2PO_4 electrolytes and WC loadings of 10 mg cm^{-2}.

Resumé

Brændselsceller ved 200-400°C er af interesse da de kan kombinere fordele fra lav- og højtemperaturteknologier. En forøgelse af temperaturen i forhold til hvad der bruges for polymer elektrolyt membran (PEM) brændselsceller forbedrer kinetikken af katalysatorerne, og dermed åbnes der mulighed for anvendelse af ikke-ædelmetal katalysatorer. Dog er driftstemperaturen lav nok til at også relativt billige materialer kan anvendes som konstruktionsmaterialer.

I dette arbejde er et formålsbygget set-up og brændselscellehardware konstrueret til demonstration af brændselsceller til mellemtemperaturområdet. Til elektroderne blev karbonklæde og karbonpapir testet som gasdiffusionslag med forskellige katalytiske lag. Af de to havde karbonpapir med en platinmængde på 7 mg cm^{-2} en bedre virkning. Karbon er ustabilt under driftsforholdene i en brændselscellekatode og andre materialer må findes. Det blev forsøgt at anvende rustfrit stål (316L), hvilket imidlertid korroderede og stålet blev derfor belagt med tantal. Tantalbelægningerne blev fundet til at være korrosionsmodstandsdygtige og resulterede endvidere i ekstrem lav kontaktmodstand på 1,3 $m\Omega\ cm^2$.

I litteraturen rapporteres celler med cæsium dihydrogen fosfat (CsH_2PO_4) elektrolyt som de mest lovende for mellemtemperaturområdet. CsH_2PO_4 gennemgår faseovergang ved 230°C. Med en stigning i ledningsevne fra 8,5 x 10^{-6} ved 223°C til 1,8 x 10^{-2} S cm^{-1} ved 233°C kaldes denne overgang for superprotonisk faseovergang. Denne elektrolyt, ligesom andre elektrolytter til dette temperaturområde, lider af dårlige mekaniske egenskaber og stabile brændselsceller er kun demonstreret med tykke elektrolytter. Derudover, for at bibeholde høj ledningsevne af elektrolytten, er en høj befugtning af fødegasserne nødvendig.

Kompositter med CsH_2PO_4 blev i dette arbejde lavet for at forbedre egenskaberne af materialet. Kompositter i formation med mekanisk stærke materialer inkusiv ZrO_2, TiO_2 og $NdPO_4{\cdot}0.5H_2O$ mindskede permeabiliteten af elektrolytten, som ydermere resulterede i forbedret stabilitet af brændselscellen. Open circuit voltage (OCV) for sådanne celler var høje, over 0,9 V, og stabile op til 250°C. Kompositdannelse med ZrO_2 resulterede desuden i forøget ledningsevne ved højere temperaturer sandsynligvis på grund af fysisk stabilisering af den superprotoniske fase. Ved 250°C var cellen stabil i mere end 60 timer med et partial tryk af vand på kun 0,12 atm, og blev opereret op til 275°C hvor brændselscellen med en ren CsH_2PO_4 elektrolyt ikke længere var funktionsdygtig.
Kompositdannelsen mellem CsH_2PO_4 og $NdPO_4{\cdot}0{,}5H_2O$ gav sandsynligvis anledning til dannelsen af en ny fase, $CsH_5(PO_4)_2$, som har en høj ledningsevne fra omkring 150°C. Mekanismen bag stigningen i ledningsevnen for $CsH_2PO_4/NdPO_4{\cdot}0{,}5H_2O$ kompositten blev dog ikke fuldt afklaret. Ved at bruge sådanne elektrolytter kunne brændselscellen opereres ved 285°C hvor den højeste ydelse blev målt. Strøm- og effekttætheder blev målt

til henholdsvis 117 mA cm^{-2} og 27,7 mW cm^{-2}.
Kompositdannelse med melamin cyanurat resulterede i øget ledningsevne i hele det målte temperaturinterval *i.e.* fra 120 til 260°C. En ledningsevne så høj som 0,18 S cm^{-1} blev målt for en 90CsH_2PO_4/10melamin cyanurat komposit ved 250°C. Ydermere blev det observeret at disse kompositter havde gode mekaniske egenskaber.

Indenfor PROCON projektet blev en screening udført for at søge efter nye elektrolytter. Fra denne screening blev niobium og bismut fosfat fundet til at have høje ledningsevner (>10^{-2} S cm^{-1}) med fornuftig stabilitet, og det blev derfor forsøgt at fabrikere elektrokemiske celler med disse. De ublandede fosfater havde dårlig mekanisk stabilitet og derfor blev polybenzimidazole (PBI) tilført. Ved at tilføre PBI i stor mængde blev der målt stabile OCVer, disse forblev stabile i 10 og 70 timer for henholdsvis niobium og bismuth fosfat. Ved højere temperaturer faldt OCV, som ved 200°C var under 0,9 V.

Wolframkarbid (WC) blev evalueret som en ikke-ædelmetal katalysator til hydrogen udvikling og oxidation reaktionerne. Karbider blev fremstillet på forskellig vis for at opnå højere overfladeareal i forhold til det meget lave overfladeareal som kommercielt karbid har, dette havde så lavt et overfladeareal at det ikke kunne kvantificeres. Ved at fremstille karbid fra WO_3 (WC-mWO_3) som blev fremstillet fra en mesoporøs silica skabelon ved karburisering med methan ved 900°C i tre timer blev et overfladeareal på 6 m^2 g^{-1} målt. Ved at introducere et ekstra syntheseskridt ved først at omdanne WO_3 til W_2N som derefter blev omdannet til WC (WC-mW_2N) blev et højere overfladeareal på 18 m^2 g^{-1} målt.
Brugen af methan i forhold til ethan som karburiseringsmiddel blev undersøgt ved karburisering af commercielt WO_3 under de samme betingelser. Fra karburisering med methan kunne der ikke måles noget overfladeareal, mens karburiseringen med ethan (WC-ethane) resulterede i et overfladeareal på 12 m^2 g^{-1}. En ekstra wolframkarbid (WC-05-VN) med et overfladeareal på 31 m^2 g^{-1} blev undersøgt for sammenligning.
Hydrogen evolution aktiviteter for karbiderne blev målt i fosforsyre ved 185°C og -100 mV. Det blev fundet at bortset fra WC-mW_2N steg aktiviteten med stigende overfladeareal, og afvigelsen for WC-mW_2N kan skyldes et amorft karbon overfladelag. Aktiviteterne blev fundet til 1,5, 2,07, 10,7 og 18,73 A g^{-1} for henholdsvis WC-mWO_3, WC-mW_2N, WC-ethane og WC-05-VN.
Karbiderne blev desuden undersøgt som katalysatorer til anoden i brændselscellen. Den bedste ydelse blev fundet ved den højest målte temperatur (270°C) hvor effekttæthederne blev fundet til henholdsvis 2,7, 3,1, 7,4 og 8,2 for WC-mW_2N, WC-mWO_3, WC-05-VN og WC-ethane. Til disse målinger blev CsH_2PO_4 brugt som elektrolyt og WC loadingen var 10 mg cm^{-2}.

Acknowledgments

The work reported in this thesis is conducted in the period from August 15th 2011 to August 15th 2014 as partial fulfillment of the requirements for the degree of Doctor of Philosophy in the Section for Proton Conductors at DTU.

Special thanks are directed to my main supervisor Professor Niels J. Bjerrum and co-supervisors Senior Researcher Erik Christensen, Lektor Jens H. von Barner and Associate Professor Qingfeng Li for giving me the opportunity to complete the project. Thanks to everyone in the Section for Proton Conductors and participants of PROCON and MEDLYS projects, who has helped in their own ways during the three years.

It should be mentioned that this work could not have been achieved without extensive collaboration. Many discussions during PROCON and MEDLYS meetings have added to the thesis and some results have been achieved in collaboration with partners from these projects.
Neodymium phosphate was synthesized and characterized by Tatiana Anfimova. The preparation of tungsten carbide was performed during a research stay at the Technical University of Munich, Germany, in close collaboration with Professor Klaus Köhler and PhD Simon Meyer. Measurements of tungsten carbide performed in phosphoric acid were performed in close collaboration with Antonio L. T. Garcia who furthermore provided an additional material (WC-05-VN) for comparison. Preparation and characterizations of niobium and bismuth phosphates were done by colleagues from the University of Changchun, China.

Gratitude should be expressed to Simon Meyer and Klaus Köhler for a beneficial research stay in their group, and for generously sharing their knowledge.
Thanks are due to Tatiana Anfimova, Antonio L. T. Garcia, Danish Power Systems and colleagues from the Changchun Institute for collaboration on experimental work and discussions.

Special thanks are extended to Martin Kalmar Hansen for generous help with proof-reading.

This thesis is dedicated to everyone interested - may you benefit from my mistakes.

Technical University of Denmark, August 15th 2014

Annemette Hindhede Jensen

Contents

Chapter 1

Introduction

The worldwide demand for steady and reliable energy from renewable sources is growing. A combination of short and long term problems as supply shortage and pollution calls for a more clean and sustainable energy supply. In Denmark one of the political goals is to achieve a better climate by solely using renewable energy by 2050. For this to be fulfilled the entire energy system must be restructured. [1]
Renewable energy is energy coming from sources which are naturally replenished. Being the biggest energy reserve the sun is the most obvious alternative, however solar based technologies suffer the disadvantage of low conversion efficiency. Amongst other alternatives are wind and hydrothermal energy, although they have, as solar energy, the disadvantage of varying output due to varying weather conditions. By using hydrogen as a bridge between renewable energy sources and fuel cells it may become possible to create a sustainable energy cycle with stable output. [2, 3]

Fuel cells are devices which in an efficient and clean way convert chemical energy into electrical energy and heat, by electrochemical conversion of hydrogen-rich fuel and oxygen into water. The fuel cell technology has been known for many years. It was invented by William Grove in 1839 and first used in the 1960s by NASA in the Gemini program, and have been operated in space crafts since. [4, 5] Only in the 1990s fuel cells for terrestrial and more conventional applications have been developed. In 1993 Ballard Power Systems demonstrated a fuel cell driven bus. Later, in 2005, Samsung revealed a fuel cell powered computer with a proven runtime of 15 hours. [6] Importantly, fuel cells cars have the possibility of replacing gasoline and diesel vehicles and are slowly being integrated. For instance, Toyota have planned to launch a new generation fuel cell car in Japan, the US and Europe in 2015. [7]

Different fuel cell technologies exist usually categorized based on the electrolyte, operating temperature and application. Electrolytes may be liquid such as phosphoric acid, potassium hydroxide or molten carbonate, or it may be solid as in solid oxide fuel cells. Solid electrolytes are preferred since these are sturdier, and more compact cells can be fabricated. [8, 9, 10] The system design of fuel cells is flexible, as they are fabricated in stacks depending on the power requirement for a wide range of applications. Applications range from small scale *e.g.* computers and mobile phones to large scale *e.g.* backup power. For instance, at Toyota Motor Sales, a 1.1 MW hydrogen fuel cell is supplying electricity, while

for a mobile phone charger a 2 W fuel cell is available. [11, 12]

Table 1.1: *Different types of fuel cells, their most common electrolytes, mobile ions and catalysts. [4, 13]. MO = metal oxides, **YSZ=Yttria stabilized zirconia.*

	AFC	**DMFC**	**PEMFC**	**PAFC**	**MCFC**	**SOFC**
Electrolyte	KOH	Polymer	Polymer	H_3PO_4	(Li,Na,K)CO_3	YSZ**
Mobile ion	OH^-	H^+	H^+	H^+	CO_3^{2-}	O^{2-}
Operating temp. (°C)	< 200	<200	<200	150-220	600-700	500-1000
Catalyst (anode)	Ni, Ag, MO*	Pt/Ru	Pt	Pt	Ni	(Ni,Co)-ZrO_2
Catalyst (cathode)	Ni, Ag, MO*	Pt	Pt	Pt	NiO	La(Sr)MnO_3

Table 1.1 summerises the main types of existing fuel cell technologies: alkaline (AFC), direct methanol (DMFC), polymer electrolyte membrane (PEMFC), phosphoric acid (PAFC), molten carbonate (MCFC) and solid oxide fuel cells (SOFC). As can be noticed from the table, the operating temperatures of the various types of fuel cells are characterized by being either low <220°C or high >500°C thus leaving a gab in the temperature range intermediating those.

Fuel cell research at low temperatures is dominated by the PEM technology which seems to be most viable for mobile applications. It is particularly interesting that operation temperatures and compact design render polymer-based fuel cells the best candidates for automotives. In PEM fuel cells a polymer membrane (*e.g.* Nafion®) is used as electrolyte. A liquid, in this case water, must be kept in the polymer membrane to maintain the conductivity. This means that the operation temperature must be kept below 100°C and thus the most efficient and expensive catalyst, platinum, is used. [2, 8] Moreover, the expensive platinum catalyst for PEM fuel cells suffers from the CO poisoning effect, which has shown to be very temperature dependent and is critical at low operational temperatures. For example a CO content as low as 20 ppm has shown to result in a significant loss of fuel cell performance. [8] To enable higher working temperatures of PEM fuel cells, other membranes have been sought for. In 1995, the finding of polybenzimidazole (PBI) was a breakthrough for PEMFC research technology, as it doped with phosphoric acid can reach working temperatures up to 200°C, *i.e.* high temperature PEMFC (HT-PEMFC). [14]
At high temperatures SOFCs are most promising candidates mainly for stationary applications. SOFCs produce a higher power output than other fuel cell technologies, however the high temperatures results in lack of materials stability. The high operation temperature used in these systems thereby limits the choice of materials to be used and causes sealing problems. A major limitation to a breakthrough in this area is the production of a cell with stable long term performance. [8]

The potential of zero CO_2 emission and other air pollution emissions combined with the

ability to provide continuous power makes fuel cells attractive for a future energy network. Given the problems of existing technologies, a goal is to combine the advantages from high and low temperature technologies. Fuel cells working at intermediate temperatures is an emerging technology and efforts have been devoted to develop proton conducting materials suitable for operation of such cells. This temperature range is of strategic importance, since it bridges the gap between the currently available low (*i.e.* PEM) and high (*i.e.* SOFC) temperature fuel cell technologies, and covering this temperature range is considered to be of particular importance for the development of fuel cells for practical applications. [15] Increasing the temperature above what is currently available in polymer based technologies enables biofuels to be oxidized *in situ*. Electrode kinetics will be greatly enhanced, heat can be recovered and the CO tolerance will be greatly increased. On the other hand, the temperature range is low enough to allow for more readily available source of heat for heating up the cell, and permits the use of a wide selection of construction materials, which may allow for simplified cell and stack construction as well as low costs and extended durability compared to the high temperature fuel cells.

1.1 Thesis objectives

In general, the scope of this thesis is to demonstrate a fuel cell working at intermediate temperatures. The work aims at demonstrating full electrochemical cells operational at intermediate temperatures and elucidates the challenges and future perspectives of such cells. In this project the intermediate temperature range is defined as temperatures intermediating those of PEM and SOFC technologies; temperatures from around 200 to 400°C are of particular interest. The work involved construction of a set-up, and the design and fabrication of a test cell. The assembling of the electrochemical cell is based on the most common intermediate temperature proton conducting electrolyte, cesium dihydrogen phosphate (CsH_2PO_4). Shortcomings in the use of CsH_2PO_4 electrolyte are addressed and improved by composite formation with oxides, neodymium phosphate and melamine cyanurate. Alternative electrolytes are considered for potential use. For this bismuth and niobium based electrolytes were investigated. Lastly, tungsten carbide is synthesized, characterized and demonstrated as a non-noble catalyst.

1.2 Thesis outline

The overall structure of the thesis consists of this introduction followed by a study of the published research within the field (Chapter 2). The experimental chapters are introduced by a description of the experimental techniques used throughout the work (Chapter 3). Two chapters are devoted to the description of the electrochemical cell: Chapter 4 describes the hardware, while Chapter 5 is devoted to a description of the fabrication of membrane

electrode assemblies. Development of the already described CsH_2PO_4 electrolyte is investigated in Chapter 6 by composite formation, and novel electrolytes (niobium and bismuth phosphates) are investigated in Chapter 7. Finally, in Chapter 8 tungsten carbide is considered as non-noble catalyst. The thesis is concluded with a discussion of the intermediate temperature fuel cell concept in a summery of the main results, followed by a perspective suggesting future investigations and directions.

Chapter 2

Intermediate Temperature Fuel Cells - Literature Study

The temperature range intermediating those used for low and high temperature fuel cells allows for good material stability, fast reaction kinetics, utilization of waste heat, CO tolerance and *in situ* reforming of *e.g.* methanol or ethanol.
This chapter highlights the work performed on intermediate temperature fuel cells so far. Electrolytes and their proton conduction mechanism, construction materials, non-noble metal-based electrode materials and fuels alternative to hydrogen are reviewed.

2.1 Electrolytes

In 1999 Norby [15] presented an overview of the proton conductivity of selected electrolytes as function of the inverse temperature (Figure 2.1). With this figure he illustrated that there is a 'gab' *i.e.* the shortage of a sufficiently proton conducting electrolyte in the temperature range from around 100 to 600°C. At low temperatures (<200°C) Nafion® and phosphoric acid are presented, and at higher temperatures (>500°C) oxides and a phosphates are ionic conductors. Two oxides, Gd-doped $BaPrO_3$ and Y-doped $BaCeO_3$ are shown in the high temperature range. The curve of $BaCeO_3$ is a calculated estimate and it was discussed by Norby [15] whether the interpretation of the conductivity of Gd-doped $BaPrO_3$ is somewhat ambigoues.

Later, two classes of proton conductors have been proven to have high conductivities in the gab. The first class is based on solid acids. Solid acids are known for their phase transitions giving rise to high conductivities and the finding of such class of solid proton conductors have resulted in more than 500 published papers. [16] Of the solid acids the most promising results have been reported from the use of CsH_2PO_4. The viability of CsH_2PO_4 as fuel cell electrolyte was demonstrated by Boysen *et al.* [17] in 2004. The second class is based on pyrophosphates, MP_2O_7, where M is a tetravalent cation. In 2006 Nagao and coworkers [18] showed promising characteristics of SnP_2O_7-based electrolytes for fuel cell applications.

The finding and demonstration of these two electrolyte types became the inception of a whole new research area focusing on the investigation of sufficient electrolytes for intermediate temperature fuel cells. The reported literature using these types of electrolytes for fuel

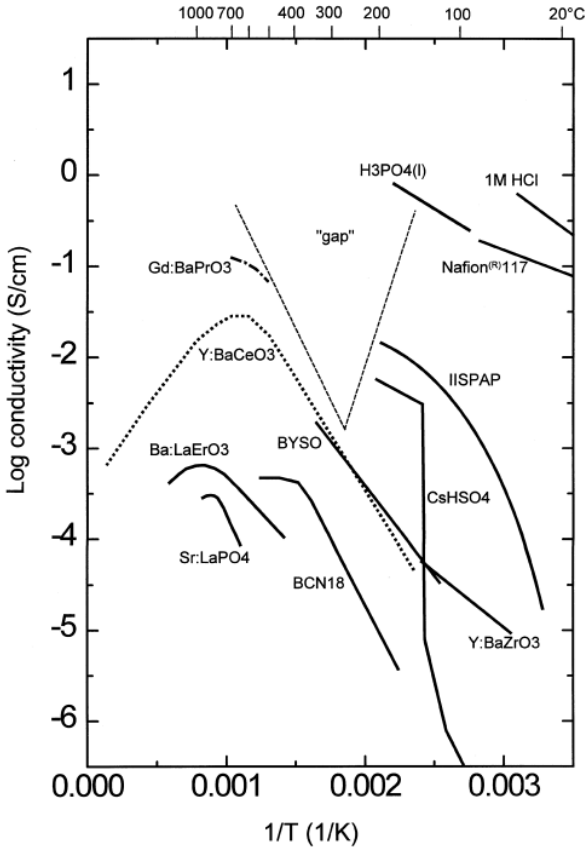

Figure 2.1: *Proton conductivity of selected electrolyte materials as function of inverse temperature. IISAP: imidazole-intercalated sulfonated polyaromatic polymer; BYSO: $Ba_2YSnO_{5.5}$; Gd:BaPrO3: Gd-doped $BaPrO_3$; Y:BaCeO3: Y-doped $BaCeO_3$; Ba:LaErO3: Barium-doped $LaErO_3$; Sr:LaPO4: Sr-doped $LaPO_4$; BCN18: $Ba_3Ca_{1.18}Nb_{1.82}O_{8.73}$; Y:BaZrO3: Y-doped $BaZrO_3$. [15]*

cell applications is described in more detail below.

2.1.1 Solid acids

Solid acids is a class of materials whose properties have been investigated for decades mainly for their proton conductivity. The proton conductivity of these materials is characteristic in terms of a phase transition temperature, above which the proton conductivity increases several orders of magnitude *i.e.* superprotonic phase transition. Although the physical and chemical characteristics of solid acids have been studied for more than 20 years, the exploration of such materials in fuel cells is very limited.

Of the solid acids, $CsHSO_4$ has been the model solid intermediate temperature proton conducting compound with high proton conductivity from the transition temperature of 140°C to the decomposition temperature at 200°C. In 2001, the first ones to test this electrolyte in a real fuel cell were Haile *et al.* [19]. With a high OCV (1.1 V) and a generated current density of 44 mA cm^{-2} at 160°C in humidified H_2 and O_2 and a platinum loading of 18 mg

cm^{-2}, a technical demonstration was given. This work proved the concept that a true solid acid proton conductor could be used in a real fuel cell assembly. However severe material difficulties such as softness in superprotonic phase, solubility in water and a narrow working temperature interval had a discouraging effect on the research of this compound.

A more encouraging breakthrough was achieved by the same research group by using CsH_2PO_4 above its transition temperature. In 2004, D.A Boysen *et al.* [17] fabricated a fuel cell with a membrane thickness of 260 μm. By suppressing dehydration of the electrolyte by humidifying the oxygen and hydrogen gases (pH_2O=0.3 atm) (Figure 2.2) the fuel cell remained stable for 100 hours at 235°C. With this cell current and power densities of more than 300 mA cm^{-2} and 50 mW cm^{-2} with a platinum loading of 18 mg cm^{-2} were reported. The viability of CsH_2PO_4 as a fuel cell electrolyte was later confirmed by Otomo *et al.* [20]. Later, in 2005, T. Uda *et al.* [21] showed a high performance CsH_2PO_4-based fuel cell made with a 25 μm thin membrane supported on porous stainless steel gas diffusion electrodes. They obtained high OCVs, above 0.9 V, and peak power densities of 415 mW cm^{-2} at temperatures of 240°C and a platinum loading og 7.7 mg cm^{-2}. Thus demonstrating the possibility of fabricating thin electrolytes from solid acids was successful. The stability of the cell was however hindered by the mechanical nature of the electrolyte and the performance was limited by the cathode kinetics rather than electrolyte resistance.

2.1.2 Pyrophosphates

The second class of materials for electrolytes for intermediate temperature fuel cells, is based on pyrophosphates. These materials are characterized by having high conductivities which can be further improved by doping.

Following the preparation of SnP_2O_7 with an anhydrous proton conductivity above 10^{-2} S cm^{-1} between 150 and 300°C [22], various metal pyrophosphates (MP_2O_7, M = Sn, Ti, Si, Ge, Ce and Zr) have been investigated for their possible use. [18, 23, 24, 25] The conductivity of SnP_2O_7 has been found to increase by doping with lower valence cations such as Al^{3+} and In^{3+}, Sb^{3+}, Sc^{3+} and Mg^{2+}. [23, 24, 26] For example, X. Wu *et al.* [26] achieved a conductivity greater than 0.1 S cm^{-1} at 300°C by Sb-doping SnP_2O_7. Nagao *et al.* [18] investigated the conductivities of doped and non-doped SnP_2O_7 under different partial pressures of water. At 250°C the conductivity was found to increase with increasing water content, a conductivity of 0.07 S cm^{-1} was measured at a partial pressure of water of 0.12 atm. Partial substitution of Sn^{4+} with In^{3+} was found to give even higher conductivities *e.g.* a raise from 5.56 x 10^{-2} to 1.95 x 10^{-1} S cm^{-1} at 250°C. Later, in 2006, encouraged by the high conductivities, the same group [27] demonstrated a working fuel cell using the same electrolyte ($Sn_{0.9}In_{0.1}P_2O_7$). High current and power densities of more than 0.9 A cm^{-2} (at *ca.* 0.3 V) and 264 mW cm^{-2}, respectively, were achieved at 250°C using dry air and electrolyte thickness of 0.35 mm (Pt loading unknown) (Figure 2.3). [27]

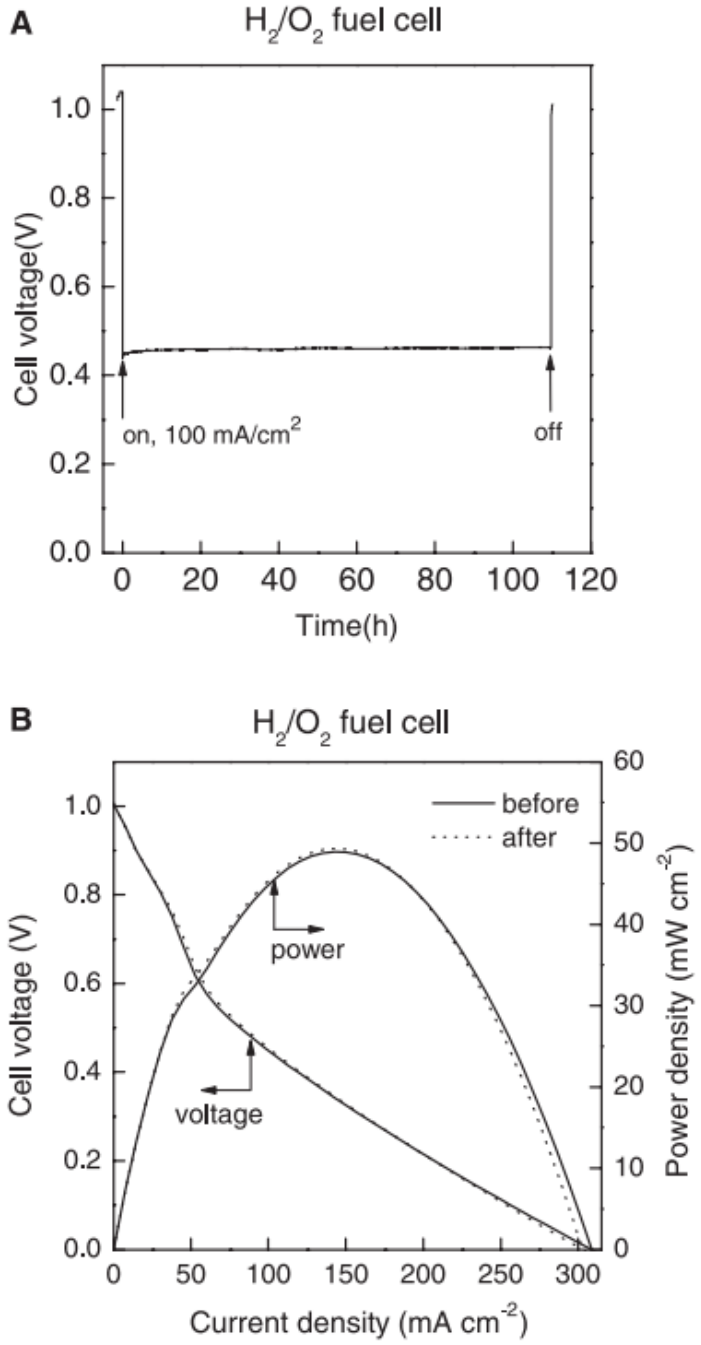

Figure 2.2: *H_2/O_2 fuel cell performance with CsH_2PO_4-based electrolyte of 260 µm. The cell was operated at 235°C while flowing the gases through water at 70°C. (A) Cell voltage and water partial pressure as function of time, while drawing 100 mA cm^{-2} continuous current for 100 hours. (B) Cell voltage and power density vs current density before and after the measurement at 100 hours. [17]*

Thus, a promising performance was demonstrated for such fuel cells. OCVs and peak power densities obtained in fuel cells of this type are lower than what could be expected

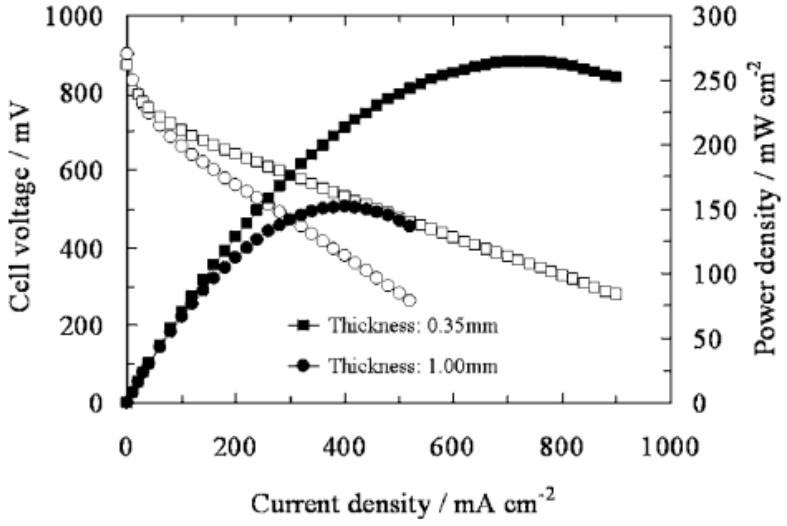

Figure 2.3: *Fuel cell polarisation in and power density curves in unhumidified hydrogen and air using $Sn_{0.9}In_{0.1}P_2O_7$ electrolytes at different thicknesses at 250°C. [27]*

from the ohmic resistance of the electrolyte, thus allowing for significant improvements. It was estimated that the cathodic overpotential contributed to more than 80% of the overall voltage drop during cell discharge. Therefore, improvement of such fuel cells requires development of a more active cathode. [28]

2.1.3 Electrolyte development by composite formation

Promising demonstrations have been reported for CsH_2PO_4 and SnP_2O_7-based fuel cells, which both have high conductivities (>10^{-2} S cm^{-1}). Other key criteria are chemical and mechanical stability, and ability to be manufactured into an appropriate shape. For example, to limit the ohmic resistance the electrolytes must be prepared as thin layers. Both types of phosphates suffer from mechanical instability which precludes the fabrication of thin layer electrolyte which is conducting and have mechanical properties suitable for fuel cell applications. Therefore, research on electrolytes for the intermediate temperature range have recently directed attention towards composite materials. Several phosphate based composites have been synthesized with the aim of improving mechanical properties, water retention, conductivity and enable the possibility of fabricating thin and dense electrolyte layers. [29, 30, 31, 32, 33] Limited information on fuel cell demonstrations have been reported and poor mechanical properties have limited the use almost exclusively to pressed pellets with thicknesses of a few millimeters. [23, 24, 25]

For solid acids improvements were achieved in terms of the enhanced low temperature (150-230°C) conductivity, extended superprotonic phase (>250°C) and strengthened mechanical behaviors. For example Matsui *et al.* [34] stabilised the superprotonic phase of CsH_2PO_4 with SiP_2O_7. At the interphases there was a formation of $CsH_5(PO_4)_2$ with a conductivity

higher than pure CsH_2PO_4. Maximum conductivity of the composite was found to be 66 mS cm^{-1} at 272°C. This electrolyte was demonstrated in a fuel cell. The OCV was despite the thickness of the electrolyte (1.8 mm) lower than 0.8 V, however good performance was obtained with a maximum current density of 150 mA cm^{-2} and maximum power density of 44 mW cm^{-2} at 220°C (Pt loading of 1 mg cm^{-2}). Such fuel cell is shown in Figure 2.4. [34]

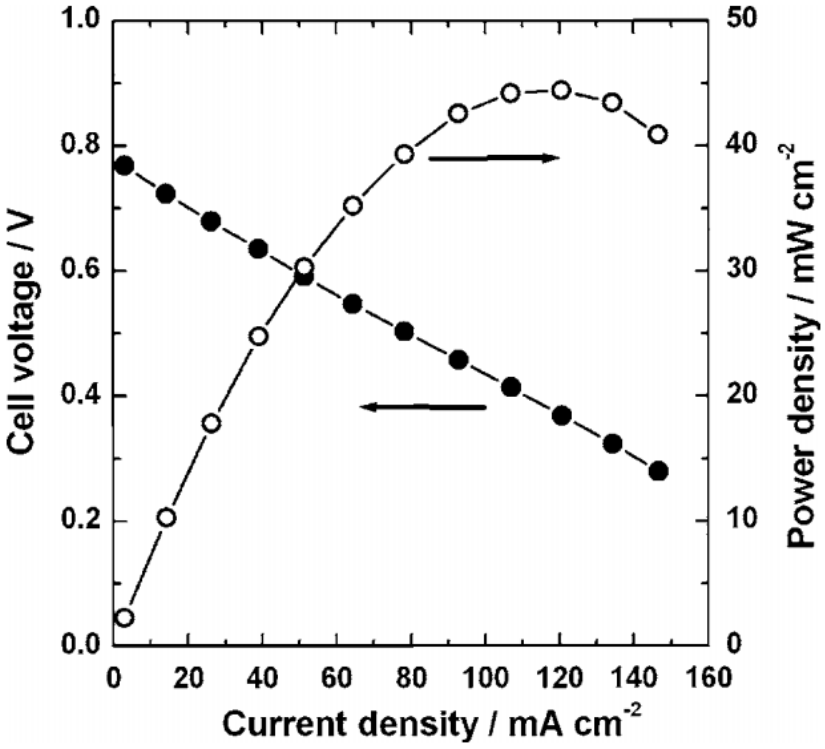

Figure 2.4: *I-V and I-P characteristics of a single cell at 220°C. [70% H_2/H_2O,Pt/C|CsH_2PO_4/SiP_2O_7(1:2)|Pt/C, 70% O_2/H_2O. Electrolyte thickness 1.8 mm. [34]*

Other authors improved the properties of solid acids by forming composites with oxides such as SiO_2, TiO_2, Al_2O_3. [35, 36, 37, 38] *E.g.* the low temperature conductivity of CsH_2PO_4 was improved by forming composites with SiO_2. High proton conductivities of 10^{-3}-10^{-2} S cm^{-1} were found for the composites, compared to around 10^{-8} for pure CsH_2PO_4 in an extended range from around 130°C to 250°C. [38]

For SnP_2O_7-based electrolytes, improvements of the electrolyte have been achieved in terms of enhanced proton conductivity and ease of preparation of thin layered electrolytes. *E.g.* N. Beck *et al.* [39] mixed SnP_2O_7 and LaP_3O_9 (Sn:La, 82:18) and reported higher conductivity (1.7 x 10^{-4} S cm^{-1}) for the composite than for the individual compounds. Using such a composite, high OCVs were achieved (0.983 V at 350°C) and the conductivity was found stable for a period of 40 h. [39]

Though at lower temperatures (>100°C), it should be mentioned that the group of Hi-

bino used polymers as supporting matrices for $Sn_{0.95}Al_{0.05}P_2O_7$ to prepare electrolytes with thicknesses less than 100 μm. [28, 40, 41] As an example, a resultant fuel cell of $Sn_{0.95}Al_{0.05}P_2O_7$ (50 μm) generated OCVs of approximately 1 V and power densities of 200 mW cm^{-2} between 100 and 150°C in H_2 and O_2 and Pt loading of 1 mg cm^{-2}. [40]

2.1.4 Other phosphate electrolytes

In addition to the solid acids and pyrophosphates, there are several reports on other phosphate based electrolytes. For example conductivities of phosphates of lanthanum, yttrium, neodymium and zirconium have been studied. Due to high chemical and thermal stability together with proton conductivity, their use as electrolytes have been suggested. Conductivity of such phosphates is temperature dependent, and has been studied from around 300°C and found to increase in turn with temperature. Probably the most important, lanthanum phosphate, is widely studied due to its conductivity and chemical stability. The proton conductivity of the pure $LaPO_4$ was reported to be around $10^{-6.5}$ S cm^{-1} at 500°C, [42] while doping rare-earth phosphates with Ca^{2+} or Sr^{2+} has shown to improve the conductivity significantly. [42, 43, 44, 45] *E.g.* Kitamura *et al.* [42] achieved conductivities between $10^{-5.5}$ and $10^{-3.5}$ S cm^{-1} for all $LnPO_4$ (Ln = La, Pr, Nd and Sm) from 500 to 925°C under wet atmospheres by doping with 1 mol% Sr (see Figure 2.5).

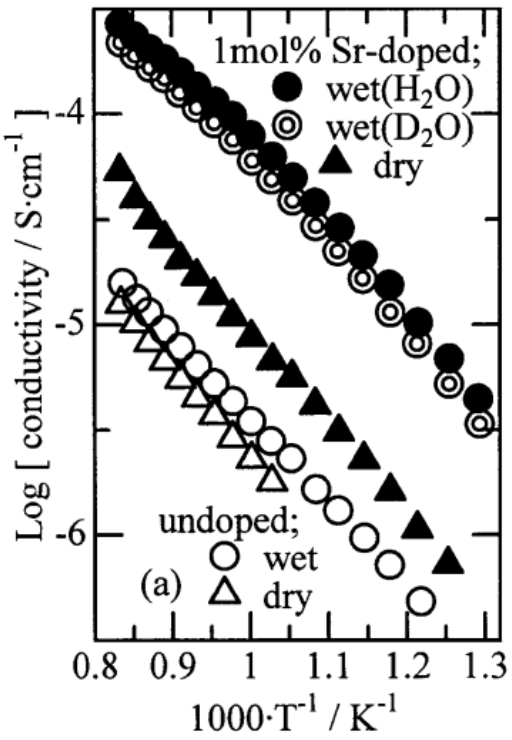

Figure 2.5: *Conductivities of 1 mol% Sr-doped $LaPO_4$ under wet (H_2O or D_2O) and dry atmospheres at p(O_2)=1 kPa. [42]*

2.2 Proton conduction

There are two overall mechanisms of proton diffusion, the vehicle mechanism and the Grotthus mechanism. In the vehicle mechanism the protons are transported as passengers on a a vehicle *i.e.* a larger ion (*e.g.* H_3O^+) and a counter diffusion of unprotonated vehicles (*e.g.* H_2O) ensures a net proton diffusion. The second mechanism is free migration (often termed Grotthus mechanism) in which the protons are transported between stationary sites within hydrogen bonds. Inherent to the proton conductivity, such sites show pronounced local dynamics such as reorientation for protons to move in their trajectory. [46]

Solid acid electrolytes are comprised of oxyanions (*e.g.* ${PO_4}^{3-}$) linked together with hydrogen bonds (O-H...O). The proton conduction in CsH_2PO_4 occurs by the Grotthus mechanism where the protons are transfered between neighboring ${PO_4}^{3-}$ tetrahedra. Below the phase transition temperature the oxyanion is in a fixed orientation, *i.e.* an ordered state where the phosphate groups are only allowed to vibrate. Above the phase transition temperature the structure is highly disordered allowing almost free rotation of the oxyanions thus facilitating high conductivities. [46]

In pyrophosphates there is no general consensus concerning the path of proton movement. High conductivities are reported to occur through a secondary amorphous layer or liquid and/or water adsorbed on the surface, and therefore reported conductivities of nominal similar compounds are in non-agreement, the main reason for this seems being varying synthesis route and thermal history of the prepared phosphates. Especially excess H_3PO_4 used in synthesis and insufficient annealing contribute to high conductivities in an amorphous surface layer. [47, 48] *E.g.* Nagao *et al.* reported conductivities of 10^{-1} S cm^{-1} for In doped SnP_2O_7, whereas Lan *et al.* [47] reported 10^{-11} S cm^{-1} for the same nominal compound at 250°C by extrapolation. In spite of extensive research on the origin of the proton conduction in these compounds, it is still lacking conclusive information to determine mechanism and the true value of conductivity.

2.3 Construction materials

The main components of a fuel cell are the membrane electrode assembly (MEA), flow plates, and gaskets. Hardware such as end-plates, pipes and fittings are not considered here. A MEA consists of a membrane and two electrodes, where an electrode is comprised of a dispersed catalyst layer and a gas diffusion layer (GDL). GDLs are porous sheets, in PEM cells GDLs are usually carbon paper or carbon cloth. The degree of porosity is of importance for efficiency; high porosity facilitates fast gas transport, but high porosity also increases ohmic resistance. The GDLs have several functions as they provide mechanical support, ensures uniform distribution of the gases, facilitates water and establishes electrical contact within the cell. Bipolar plates constitutes most of the cell mass and volume. They

function as cell separators and carry current away from the cell. Specific requirements exist for the bipolar plates, the most important ones probably resistance to spalling and high electronic conductivity. In PEM systems, bipolar plates are usually non-porous graphite plates, or coated metallic or composite plates.

The two most investigated intermediate temperature fuel cell types have been fabricated in different ways.

As mentioned in Section 2.1 Uda *et al.* [21] demonstrated a high performance thin membrane CsH_2PO_4 fuel cell where a high power output of 415 mW cm^{-2} at 240°C. A mixture of CsH_2PO_4, naphthalene, Pt black and Pt/C was used as electrocatalytic layer with a total loading of Pt of 7.7 mg cm^{-2} was dispersed onto the porous stainless steel GDLs. This assembly served as one electrode onto which the electrolyte was deposited from a slurry of CsH_2PO_4 and toluene. Lastly the second electrode was attached. After deposition of each layer, the structure was pressed to promote contact between the layers. Naphtalene was removed before fuel cell measurements. The whole cell was sealed and supplied with humidified oxygen and hydrogen. [49] Gases were humidified by passing them through water held at 72°C.

Heo *et al.* [27] fabricated MEAs from $Sn_{0.9}In_{0.1}P_2O_7$ electrolyte and two electrodes made from catalyst (10 wt% Pt/C, E-TEK) and carbon paper (Toray TGPH-090) with a Pt loading of about 0.6 mg cm^{-2}. On the cathode an intermediate layer was applied by doctor blading, consisting of $Sn_{0.9}In_{0.1}P_2O_7$ with Pt/C powders with a 10% poly(vinylidene flouride) binder in 1-methyl-2-pyrrolidinone solvent (total Pt loading unknown). Prepared powders were pressed into pellets of 0.35 and 1 mm thicknesses under a pressure of 2 x 10^3 kg cm^{-2}. For fuel cell performance tests the cell was placed between two alumina tubes functioning as gas chambers. The chambers were sealed with inorganic adhesive and supplied with hydrogen and air. As pointed out earlier, a power density of 264 mW cm^{-2} was achieved using such cell with an electrolyte thickness of 0.35 mm.

2.4 Non-noble metal based electrodes

As mentioned in Section 2.3, in PEMFCs the catalyst phase consists of Pt supported on carbon, which is contacted with a porous carbon gas diffusion layer. The oxygen reduction reaction (ORR) takes place at the cathode in the fuel cell, and currently Pt and Pt alloys are used in electrodes for ORR and no commercially alternative to those are available. For improvement of Pt based cathodes two major research trends have been followed; either it has been attempted to reduce the fast aging of Pt in running fuel cells or to lower the amount of Pt. To reduce cost, a variety of non-noble-metal-based catalysts have been investigated. These involve organometallic complexes, nitrogen-doped carbon supported metal ions, transition metal oxides and chalcogenides. Also new bio-inspired catalyst designs are emerging. [50] While significant amount of research has concerned the replacement of Pt in

electrodes for ORR, less materials are suggested for the replacement of Pt for the hydrogen oxidation electrode. One group of catalysts that has been studied at lower temperature is transition metal carbides, especially tungsten carbide. This has been studied extensively due to CO tolerance, corrosion resistance, electrical conductivity and Pt-like behavior for chemisorption of hydrogen. [51]

Although promising demonstrations with non-noble-metal-catalyst-based electrodes, a few have been investigated at intermediate temperatures. Examples are shortly presented below. Muroyama *et al.* [52] demonstrated the use of WC as anode catalyst on a CsH_2PO_4/SiP_2O_7 electrolyte at 200°C and achieved a peak power density of 4.1 mW cm^{-2} compared to 56 mW cm^{-2} for the Pt/C catalyst. Heo *et al.* [53] investigated anodic overpotentials for Ni_x/C, Co_x/C, WC/C, Mo_2C in a fuel cell using an $Sn_{0.9}In_{0.1}P_2O_7$ electrolyte. Of the investigated catalysts Mo_2C showed the lowest overpotential at 250°C. Addition of ZrO_2 to the catalyst improved the catalyst performance to approach that of Pt/C. Using this as anode in a fuel cell resulted in a peak power density of 67 mW cm^{-2} compared to 84 mW cm^{-2} obtained for same cell using Pt/C. Later, using the same system Heo *et al.* [54] demonstrated a full Pt free fuel cell between 150 and 300°C. Cathodic overpotentials for oxides of Zr, W, Ni, Ce were compared at 250°C, and ZrO_2 was found to have the lowest cathodic overpotential. Prior to electrode fabrication the oxide was heat treated to improve catalytic activity. As anode catalyst Mo_2C-ZrO_2/C was also used in this cell as it performed better than Mo_2C. Full cell demonstrations were made with Pt/C|$Sn_{0.9}In_{0.1}P_2O_7$|Pt/C, Mo_2C-ZrO_2/C|$Sn_{0.9}In_{0.1}P_2O_7$|Pt/C, Pt/C|$Sn_{0.9}In_{0.1}P_2O_7$|ZrO_2/C and Mo_2C-ZrO_2|$Sn_{0.9}In_{0.1}P_2O_7$|ZrO_2/C assemblies, where the performance of the Mo_2C-ZrO_2/C|$Sn_{0.9}In_{0.1}P_2O_7$e|Pt/C approached that of Pt/C|$Sn_{0.9}In_{0.1}P_2O_7$|Pt/C. Performance of the Pt-free fuel cell using Mo_2C-ZrO_2/C as anode and ZrO_2/C as cathode was strongly dependent on temperature, giving a peak power density of 29 mW cm^{-2} at the highest temperature measured *i.e.* 300°C, compared to a power density of 6 mW cm^{-2} which was reached at 150°C. These results are shown in Figure 2.6.

Apart from fuel cells it should also be mentioned that Papandrew *et al.* [55] demonstrated the use of nickel for the hydrogen evolution reaction (HER) on a CsH_2PO_4 electrolyte. Unsupported nickel (3.5 mg cm^{-2}) was used as electrocatalyst in an electrochemical hydrogen pump, and Ni-based electrodes displayed promising properties as a stable reduction current of 207 mA cm^{-2} was measured at 250°C at -0.2 V, compared to 558 mA cm^{-2} measured when using Pt/C under identical conditions. Moreover the Ni-based MEA showed good stability at -0.2 V and 250°C for 100 hours.

In PEM fuel cell technology, apart from the noble catalyst research, focus is moving toward a change in the use of state-of-the-art carbon support materials. The high surface area carbons suffer from corrosion caused by the electrochemical oxidation in the fuel cell, mainly in the cathode. Effort has been put to slow down the corrosion rates, by using more

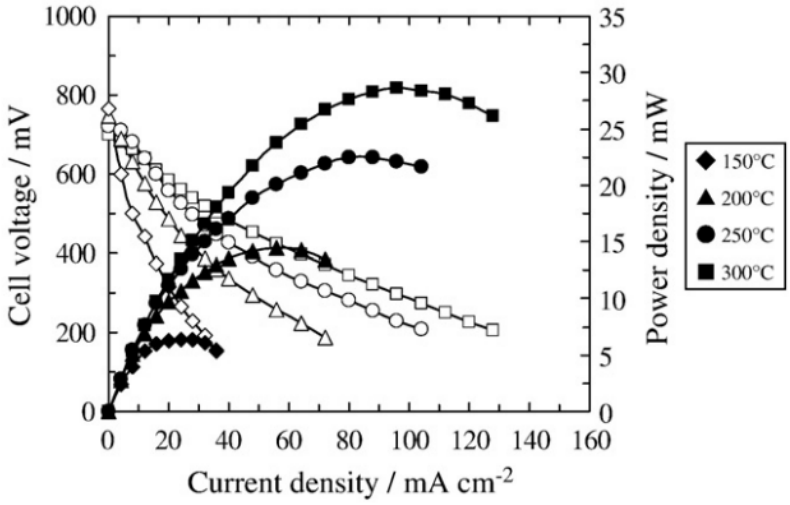

Figure 2.6: *Voltage and power density as function of current density of a Pt-free fuel cell at various temperatures. Mo_2C-ZrO_2/C and ZrO_2 are used as anode and cathode catalysts and $Sn_{0.9}In_{0.1}P_2O_7$ as electrolyte. [54]*

graphitic structure, such as carbon nanotubes or carbon nanofibers. Oxidation can not be prevented, however choosing such more stable carbon structures decreases the rate of which the carbon support corrode away. Therefore research has been directed toward non-carbon support materials, where conducting oxides and carbides are candidates. Among others, Ti- and Sn-based oxides, WO_3, $RuO_2 \cdot H_2O$, S-ZrO_2, SiO_2 and WC have been investigated. [56]

2.5 Fuels

Significant attention has been devoted to enable the use of hydrogen gas as a fuel as it can be produced from renewable sources. It is perceived as a clean fuel and can be integrated in a clean and sustainable energy cycle. An advantage of hydrogen is that it can be produced from several hydrogen containing compounds, however challenges with hydrogen as a fuel including storage, distribution and refueling systems hinder a hydrogen-based energy economy and major barriers remain to be overcome. Alcohols have energy densities much higher than compressed hydrogen. Alcohols are furthermore attractive as they can be produced from renewable resources. Some alcohols and other hydrogen containing compounds are shown in Figure 2.7. Their hydrogen release temperatures as well as the temperature matching with different types of fuel cells are plotted. A number of high capacity hydrogen carrying fuels are available in the gab between phosphoric acid fuel cells and molten carbonate fuel cells.

At lower temperatures, methanol is considered the most favorable alternative fuel to hydrogen. There is two major technical challenges in using methanol, fuel crossover and

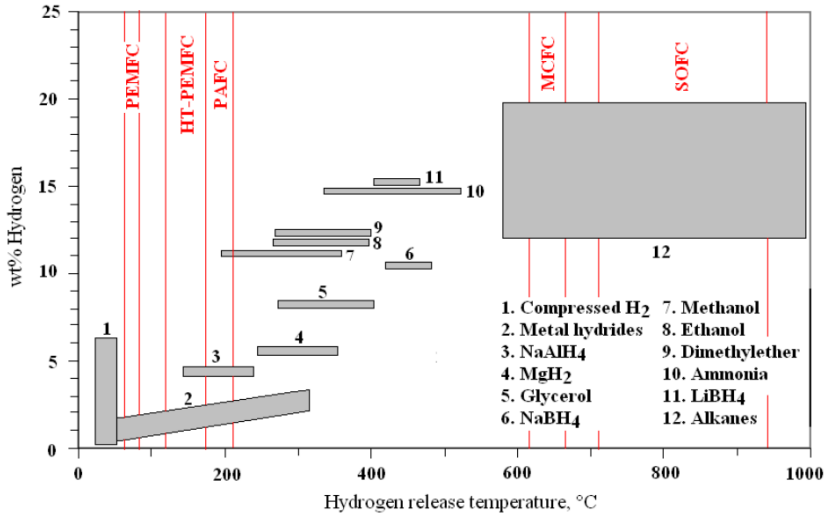

Figure 2.7: *Rough estimate of hydrogen contents obtained from different hydrogen storage concepts of different fuels against the release temperature of hydrogen and operation temperatures of fuel cells. [57]*

insufficient activity of the anode catalyst which leads to high overpotentials. [58, 59]

Direct alcohol fuel cells have also been demonstrated at intermediate temperatures. For instance, Boysen *et al.* [17] demonstrated a CsH_2PO_4-based fuel cell vaporfed with methanol. An electrolyte thickness of 260 μm was used and the cell was running for 35 hours at 243°C showing remarkable stability. Open circuit voltage of 0.897 V and power density of 37.2 mW cm^{-2} were obtained with catalyst loadings of 13 (PtRu) and 15 (Pt) mg cm^{-2} on anode and cathode, respectively. T. Uda *et el.* [49] demonstrated high-power CsH_2PO_4-based alcohol fuel cells with Pt based cathode (7.7 mg cm^{-2}) and PtRu anode (5.6 mg cm^{-2} Pt and 2.9 mg cm^{-2} Ru). Using electrolytes with thicknesses between 26 and 77 μm peak power densities reached 226 and 100 mW cm^{-2} using methanol and ethanol at 250°C, respectively, and thus approaching those measured in PEM systems. Furthermore a high power output for a reformat fuel cell containing 1% of CO demonstrated CO tolerance at these temperatures. In the alcohol fueled intermediate temperature fuel cells the OCVs were found to be higher than those commonly reported for alcohol fueled PEM fuel cells.

2.6 Summary

The proton conductivity of solid electrolytes has been investigated for decades. Norby [15] introduced a 'gab' *i.e.* a lack of sufficiently proton conducting materials at intermediate temperatures, including a discussion about the strategic importance of this temperature range. Following this an interest for materials working in this range has grown and vast amount of research has been performed concerning intermediate temperatures proton conductors. The research has mainly been focused on the finding and development of elec-

trolytes and many candidates have been suggested, mainly compounds based on phosphates. These were divided into two main groups, those of solid acids and those of pyrophosphates. Though a lot of research was performed on the properties of electrolytes, limited effort was reported concerning full cell demonstrations.

Main breakthroughs were achieved by the groups of Haile [21] in 2005 and Hibino [27] in 2006, as only they have demonstrated high performance fuel cells operating in this temperature range. Both fuel cell demonstrations were performed using the phosphates alone. The highest performance has been obtained in the research group of S. Haile [21], who concluded that the stability in fuel cell performance was hindered by mechanical problems of the electrolyte and probably degradation in the electrodes, for due to the use of carbon. No stability measurement could be obtained with a high performance fuel cell, probably owing to formation of holes in the electrolyte as result of the water solubility. Limitation in peak power performance was not caused by the electrolyte, but rather the cathode performance. These obstacles have lead to vast amount of research on the fabrication of composite electrolytes in order to improve several properties including mechanical enhancement, water retention and extended temperature range of conductivity.

The electrode components used in literature reported so far are similar to materials commonly used in PEM fuel cells. Platinum supported on carbon constitutes the main part of the catalytic layer on a carbon based or stainless steel gas diffusion layer. One of the main arguments for the temperature increase compared to PEM operation temperature is the ability to use non noble metal catalysts. So far tungsten carbide seems the most promising non-noble anode catalyst alternative to Pt. Other materials have been considered, and a fuel cell without noble metals was demonstrated with promising results.

A large advantage of the temperature range has been proven as the fuel cells are CO tolerant when compared to other technologies and the solid electrolytes ensures impermeability of methanol. Moreover the use of methanol seems viable as an alternative to hydrogen fuel as the peak power densities in the first demonstrations are approaching those reported for direct methanol PEM fuel cells.

Chapter 3

Characterization Techniques

This chapter presents characterization techniques where commercial equipment is used. It is divided into two sections, one describing the equipment and procedures for physical characterizations and one describing electrochemical characterizations.

3.1 Physical characterizations

Material characterizations were performed by use of conventional equipment. These characterizations include TGA/DTA, XRD, N_2 adsorption/desorption and microscopy (light, SEM and TEM) and will be introduced in this chapter.

3.1.1 Thermal analysis

Thermogravimetric Analyses (TGA) and Differential Thermal Analysis (DTA) were performed on a Netzsch STA 409 PC in argon or air atmosphere from room temperature to 800°C with platinum crucibles as sample and reference containers. The argon or air atmosphere was dry, *i.e.* without humidification. A constant heating rate of 10°C min^{-1} was used.

Thermal analysis is widely used in material science for the study of changes in the materials with temperature. In TGA the mass of the sample is registered throughout the experiment where the temperature is continuously increased. In DTA the sample temperature relative to a reference is measured during the heating. From process enthalpies it can be determined whether processes are endo- or exothermal.

3.1.2 X-ray Diffraction (XRD)

The phase purities were revealed by room temperature XRD performed on a Huber D670 diffractometer with CuKα radiation line (CuKα radiation, λ=1.54056 Å) in the range of 3° to 100° in steps of 0.02° in 2θ.
Average crystallite sizes were calculated, using Scherrer Equation (Equation 3.1).

$$d_c = \frac{K\lambda}{B cos\theta} \tag{3.1}$$

d_c is the thickness of the electrolytes, K is the Scherrer constant, B is the full width at half maximum, λ is the wave length of the X-rays and θ is the Bragg angle. [60]

3.1.3 N_2 adsorption and BET area

To estimate specific surface areas, the Brunauer-Emmett-Teller (BET) method was used by nitrogen adsorption/desorption. The BET equation can be expressed as in Equation 3.2 [61].

$$\frac{1}{V[P_0/P-1]} = \frac{C-1}{V_m \cdot C}\left(\frac{P}{P_0}\right) + \frac{1}{V_m \cdot C} \tag{3.2}$$

The BET surface areas were measured by nitrogen absorption at 77 K on a Micrometrics ASAP 2020 apparatus. The samples were degassed *in vacuo*.

3.1.4 Light microscopy

Light microscopy images were made using a Leica MZ12 (10472649) microscope.

3.1.5 Electron microscopy

Two electron microscopy techniques were used: Scanning Electron Microscopy (SEM) and Transmission Electron Microscopy (TEM). SEM images were made using a Zeiss EVO MA 10 electron microscope and TEM analyses were performed on a Tecnai T20 G2 S-TEM microscope. For SEM and TEM powder analysis the samples were first dispersed in ethanol and, in case of TEM, dropped onto a Cu grid coated with carbon.

In electron microscopy, a beam of beam of primary electrons is generated. When it hits the specimen, several events can occur as illustrated in Figure 3.1. When the beam hits the sample, electrons can: A) pass through without suffering energy loss (if the sample is thin), and a two dimensional projection of the sample can be formed as the attenuation of the beam depends on density and thickness; B) be diffracted by particles, and thereby enable crystallographic information; C) collide with atoms in the sample and be scattered back; D) excite characteristic transitions in the sample which can be studied as the energy loss from primary electrons; E) lose energy by inelastic collisions, whereby secondary electrons are emitted by the sample; or, Auger electrons and x-rays can be formed in the relaxation of core-ionized atoms, or electron-hole pairs in the sample can cause emission of a range of photons from UV to infrared *i.e.* cathodoluminescence. [62]

I this work, transmitted electrons are used for image formation in TEM and secondary electrons in SEM, respectively.

3.2 Electrochemical characterizations

Electrochemical characterizations were performed in air, in hydrogen concentration cells, and in hydrogen/air cells using a Princeton Potentiostat Versastat 4 equipped with Versastudio software.

For conductivity measurements, both sides of electrolyte pellets were uniformly painted

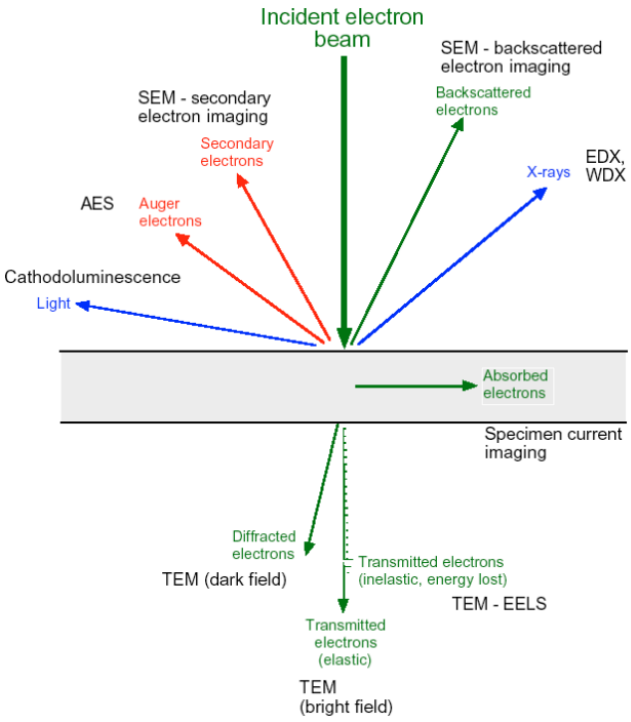

Figure 3.1: *Electron beam-specimen interaction. [62]*

with a thin layer of silver paste (Loctite® 3863, Henkel Co.). For fuel cell characterizations, MEAs were assembled as two electrodes attached on the sides of an electrolyte, The fabrication of electrolytes, electrodes and MEAs will be covered in the following chapter (Chapter 5).

3.2.1 Ionic conductivity by AC impedance spectroscopy

The ionic conductivity of electrolytes was measured by the two electrode AC technique in the frequency range from 1 Hz to 500 kHz. Impedance spectroscopy has become one of the most important tools in the characterization of electrochemical systems. The electrical element resistance, R, is described through Ohm's Law which expresses the fundamental relationship between the current and potential (Equation 3.3).

$$V = IR \tag{3.3}$$

where V is the voltage and I the current.

Like a resistor, the impedance, Z, is a measure of the ability of a circuit to resist the flow of electrons, however, the impedance, apart from the impedance of an ideal resistor, is dependent on frequency. Ohm's law is the limiting case of impedance, *i.e.* the impedance of an ideal resister would be equal to the resistance, R, while otherwise, the impedance is split into two components *i.e.* a simple resistive component and frequency dependent

resistance.

Usually the impedance is measured by applying an AC signal to the electrochemical cell and measuring the current response through the cell. If a pseudo-linear part of the cell response is used for measurements, Ohm's law and Eulers relationship (these steps are not described here) allows us to calculate the impedance of a system as in Equation 3.4.

$$Z(\omega) = \frac{E}{I} = Z_0 exp(j\phi) = Z_0(cos\phi + jsin\phi) \tag{3.4}$$

where ω is the angular frequency ($2\pi f$), ϕ the phase angle and j=$\sqrt{-1}$.

The impedance data are usually presented in a Nyquist plot, where the real part is plotted on the x-axis and the imaginary part is plotted on the Y axis. Each point on the Nyquist plot represents the impedance at one frequency.

In this work the impedance is used to measure the ionic conductivity, σ, of the prepared electrolytes. The resistance is read from the Nyquist plot, and the conductivity is calculated from the resistance and dimensions as in Equation 3.5.

$$\sigma = \frac{L}{SR} \tag{3.5}$$

where L is electrolyte thickness, S is the electrolyte geometric area and R is the measured electrolyte resistance.

3.2.2 Fuel cell principles

A fuel cell is a device which converts chemical energy directly into electricity and heat. In this chapter commonly used terms are introduced and the theoretical voltage of a hydrogen fuel cell and the reasons for operational voltage deviation are presented.

Theoretical voltages

The principle of a fuel cell with hydrogen as fuel relies on the basic simple combustion Equation 3.6.

$$H_2 + \frac{1}{2}O_2 \leftrightarrow H_2O \tag{3.6}$$

Assuming that the equation is reversible and all Gibbs free energy, ΔG is converted into electrical energy, we can use the Gibbs free energy equation (Equation 3.7) to calculate the open circuit voltage of the cell at standard pressure. [13]

$$E = \frac{-\Delta G}{2F} \tag{3.7}$$

where E is the reversible open circuit voltage (OCV) for the hydrogen fuel cell and F is the Faraday constant.

Operational voltage losses

The theoretical open circuit voltage (OCV) is changing with temperature. *E.g.* at room temperature the theoretical voltage is 1.23 V, while at 800°C it is approximately 1 V. While operating the fuel cell, the theoretical voltage is never truly realized due to losses occurring. Four types of losses are listed as: A) activation loss; B) fuel crossover/internal current loss; C) ohmic loss; and D); mass transport/concentration loss.

The activation loss occurs at low temperatures and low current densities due to limitations in kinetics of reactions taking place at the electrodes. Part of the voltage loss comes from driving the reaction. The activation loss can be evaluated by the Tafel equation (Equation 3.8). This equation was derived as the overvoltage at the surface of an electrode follows a general pattern.

$$\Delta V_{act} = Aln\left(\frac{i}{i_0}\right) \tag{3.8}$$

A is a constant and is higher if the electrochemical reaction is slow. i and i_0 are current density and the constant exchange current density *i.e.* the current density at which the the overvoltage starts to move from 0. [13]

Crossover and internal current losses are associated with the losses through the electrolyte, by fuel leakage or electrons passing. By adding the current density that occurs due to crossover, i_n into equation 3.8, this is rewritten into equation 3.9.

$$\Delta V_{act} = Aln\left(\frac{i+i_n}{i_0}\right) \tag{3.9}$$

The ohmic loss is proportional to the current (Equation 3.10). It mainly comes from the resistance to flow of ions in the electrolyte, electrical resistance of the electrodes and the flow of electrons in the interconnects.

$$\Delta V = IR \tag{3.10}$$

For consistency this should be expressed as current density, and thus the resistance should correspond to an area of 1 cm^2 of the cell. Equation 3.10 is then rewritten into equation 3.11.

$$\Delta V_{ohm} = ir \tag{3.11}$$

i is the current density and r is the area specific resistance (ASR).

Mass transport/concentration losses occur both at high and low temperatures, but is prevalent at high current densities. Transport or concentration losses mainly occur due to the cell using the fuel or oxygen faster than it is supplied. An empirical formula is favorable for fitting experimental data of transport loss (Equation 3.12).

$$\Delta V_{trans} = mexp(ni) \tag{3.12}$$

where m and n are constants. [13]

Simple model of a polarization curve

Combining the expressions for the voltage losses an equation can be derived for an operating fuel cell at a current density i (Equation 3.13).

$$V = E - \Delta V_{ohm} - \Delta V_{act} - \Delta V_{trans}$$

or

$$V = E - ir - Aln\left(\frac{i+i_n}{i_0}\right) - mexp(ni) \tag{3.13}$$

Using values for a PEM fuel cell running at 70°C a polarization curve as in Figure 3.2 can calculated. [13]

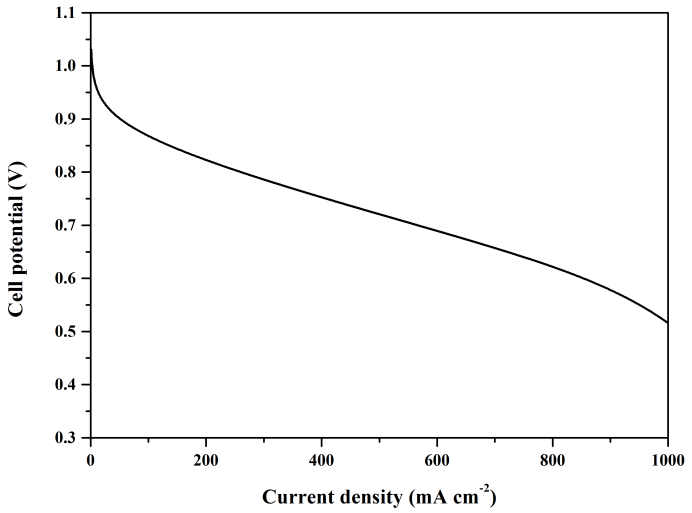

Figure 3.2: *Polarization curve using calculated from equation 3.13 values achieved from Ballard Mark V PEM fuel cell running at 70°C. [13]*

3.2.3 Hydrogen concentration cells

If the partial pressures of hydrogen, p, changes say, from p_1 to p_2, the corresponding voltage change ΔV is determined from Equation 3.14. [13]

$$\Delta V = \frac{RT}{nF} ln \frac{p_2}{p_1} \tag{3.14}$$

For EMF measurements, the cell was fed with pure hydrogen to one side and a mixture of hydrogen and nitrogen to the other side as shown below.

$$H_2 \text{ (1 atm), Pt|Electrolyte|Pt, } H_2 \text{ (0.05 or 0.1 atm)}$$

The EMF was then measured at a number of temperatures, by holding the temperature constant for minimum ten minutes while monitoring the potential. The measured potentials were compared to the theoretical values calculated from Equation 3.14. The proton transference number was calculated as the ratio between calculated and measured values.

3.2.4 Hydrogen/air fuel cell characterizations

Polarizations were performed by linear sweep voltammetry (LSV) by a continuous change in the potential while monitoring the current response. Stability measurements were performed by chronoamperometry.

Linear sweep voltammetry is a potential sweep technique, which in this work involves a sweep in the potential from the initial potential E_1, the open circuit potential to E_2 with a constant scan rate υ. [63]

Chronoamperometry is a potential step technique where the potential is instantaneously changed from the initial value E_1 to a new value E_2 where it is kept throughout a time t, while the current is measured. In this work, the open circuit potential is the initial potential E_1. [63]

Chapter 4

Cell Construction

A set-up was built for demonstrations of intermediate temperature fuel cells. In general, a single cell fuel cell is comprised of two endplates, two flowplates, gaskets and an MEA consisting of two electrodes and an electrolyte. This chapter is divided into four sections introduced by a description of the hardware, followed by evaluation of protective tantalum surface coatings. Third and forth sections describe the sealing/electrical insulation and method of humidification used throughout the work. The fabrication and characterization of the MEA is considered in a separate chapter (Chapter 5).

4.1 Hardware

The cell hardware in this work was made from two endplates, two flowplates, two heating rods, a thermocouple, gas sealing and electrical insulation. Apart from the cell hardware the set-up consisted of gas pipes, humidification of gases, mass flowmeters, and as mentioned a Potentiostat.

Figure 4.1 shows a flowplate (left) and assembled flowplates and endplates (right). The endplates were fabricated from a copper-aluminum alloy (a data sheet is attached in Appendix A). The flowplates were constructed in-house from stainless steel (316L), and coated with tantalum by chemical vapor deposition (CVD) by Tantaline®. For alignment of layers (sealing and MEA) while assembling the cell, stainless steel rods were used, but removed before measurements. The two heating rods and thermocouple were inserted in the endplates for controlling the temperature.

Gas pipes were made from 316L stainless steel and fittings were 316L Swagelok® fittings. The system could be operated with different gases, in this work H_2, H_2/N_2 mixtures and air.

4.2 Interfacial contact resistance of tantalum

Formerly used components for intermediate temperature fuel cells are based on those commonly used in PEM fuel cells. This include stainless steel and carbon materials (see Section 2.3). However, traditional construction materials are known to suffer from corrosion when using acidic electrolytes which may lead to potential loss and poisoning of the catalysts. Therefore the gas diffusion layers and flowplates were made from stainless steel coated

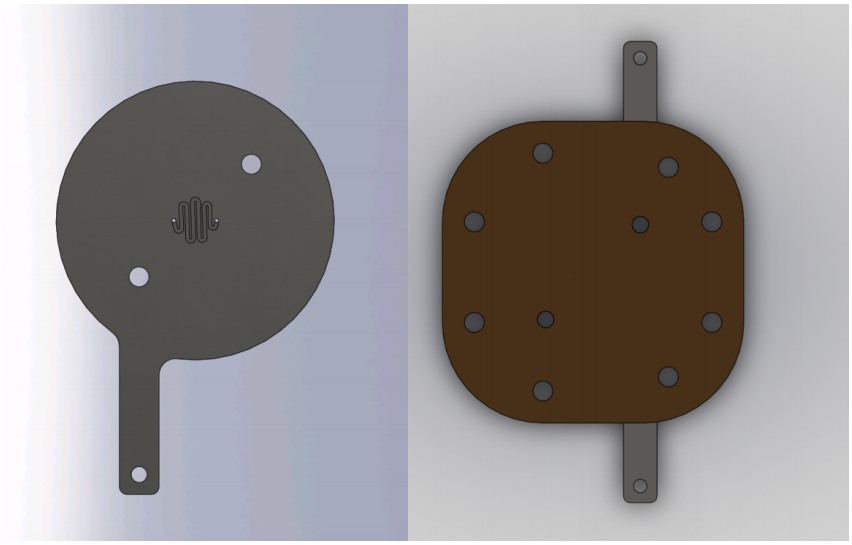

Figure 4.1: *Left: Illustration of flow plate. Right: Assembling of the cell with flowplates and endplates.*

with a tantalum layer were evaluated. Tantalum was chosen as it is known as the material with highest corrosion resistance towards hot phosphoric acid. Low corrosion rates have been reported for tantalum in phosphoric acid (<0.01 mm year^{-1} up to 150°C). [64] The superior corrosion stability of tantalum is generally ascribed to formation of a passive oxide layer.

On all, even apparently smooth surfaces there are asperities on the microscopic level. When two surfaces are clamped together, they have contact at the tips of the higher asperities resulting in an actual contact area lower than the apparent contact area. With an applied load the number of contact points are known to increase, thereby increasing the actual contact area. [65]

The contact between two surfaces clamped together has been studied from a mechanical point of view. The coefficient of friction μ is given as F/W, where F is the frictional force and W is the load or force normal to the surfaces. It is found that μ is independent on the surface apparent area of contact. This is known as Amontons' law. [65] If no motion is applied, a certain load will result in an increase in surface area due to the plastic microdisplacements of one surface relative to the other. The effect hereof will depend on the number of asperities, the size and separation of these and the total surface area. In the limiting case of no relative motion of the two surfaces F/W is denoted ϕ since this is not related to μ. The displacements will occur until a yield pressure $\mathbf{P}_m$ of the softer material is reached, and the actual area is given as $A = W/\boldsymbol{P}_m$. [65] The relation between actual contact area and applied load have been debated. From above it is suggested that the real surface area is proportional to the applied load [65]. However, later Hertz suggested that surface area increases with $W^{2/3}$ when the load courses elastic deformation. This was also found by A. Berman *et al.* [66]

Since current flows only through the contacting asperities, the limited number of these causes a voltage drop across the interface. Theory predicts an exponential decrease of contact resistance with increasing the load.

Interfacial contact resistance of tantalum coatings were measured to evaluate the effect of protective tantalum coatings on GDL/bipolar plates. Limiting corrosion conditions are simulated experimentally by anodization, and their influence on the ICR value of tantalum/tantalum surface contacts is evaluated and compared to ICR values obtained for titanium.

Tantalum plates (Goodfellow, 99.9%) 0.2 mm thick were used in sizes of 10 mm x 30 mm. Stainless steel foils (316L) were cut to the same size as the tantalum foils, and coated with tantalum by Chemical Vapor Deposition (CVD) (Tantaline®, 850°C, min. 99% purity) in thicknesses around 40 microns. All foils were treated first with an alkaline solution (commercial degreaser, Bonder V387M from Chemetall) at 90°C for 15 minutes, then washed with distilled water and subsequently treated in a commercial acidic solution ("Dry Acid", from Engtech Scandinavia) at room temperature for 5 minutes. Finally the foils were rinsed with distilled water. Preliminary measurements (not shown) without this cleaning procedure showed considerably higher values of ICR. Thus, the procedure was used for all foils. Anodizations of foils were performed using an in-house made potentiostat at 2 V and 130°C in 85% H_3PO_4 for time periods of 2, 4, 6 and 8 hours in a two electrode set-up. The foil under investigation was used as working electrode, and a platinum wire was used as counter electrode. Anodization of titanium was performed for 5 minutes.

The interfacial contact resistances were measured between two foils clamped together, as function of compaction force. The total resistance was measured in a four point arrangement using a multimeter (Keithley multimeter, 175 Autoranging multimeter) and a galvanostat. The voltage drop was measured at constant current (0.1 A), and the clamping pressure was periodically increased from 0 to 3 MPa. The total resistance was then calculated from the voltage drop using Ohm's law. The interfacial contact resistance, R_{ICR} was in turn calculated from Equation 4.1.

$$R_{ICR} = RxA \tag{4.1}$$

where R is the measured resistance and A is the apparent contact area. [67] All measurements were performed on apparent contact areas of 1 cm^2.

The interfacial contact resistances between two tantalum foils as function of compaction force are shown in Figure 4.2. These measurements, as well as all other measurements of ICR vs. force, show the characteristic shape of an initial decrease in ICR with increasing compaction force. This effect is attributed to a gradual increase of the actual contact area

with increasing compaction force due to the deformation of contacting asperities. In all measurements, the ICR decreased to a constant value, when a certain compact force was reached. The measured ICR of two tantalum plates in contact with each other is low, around 1.3 mΩ cm^2 and thus far below the US Department of Energy target value (10 mΩ cm^2). [68]

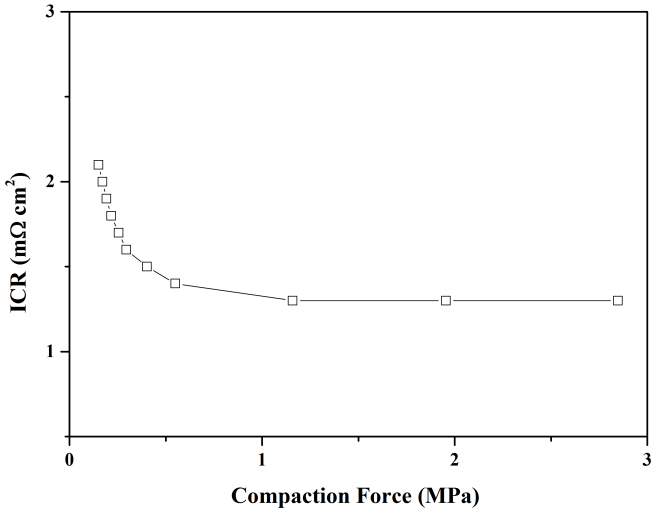

Figure 4.2: *Interfacial contact resistance between two tantalum plates as function of compaction force.*

Figure 4.3 illustrates the contact resistance values obtained for tantalum, tantalum coated stainless steel and titanium when clamped together with tantalum at a compaction force of 2.7 MPa. The figure compares ICR values obtained before and after anodization.

For the tantalum foils no increase in contact resistance was observed subsequent to anodization, therefore an eventual growth of a surface oxide layer does not seem to have a significant effect on the ICR at these conditions. ICR values were 1.3 and 3.18 mΩ cm^2 before and 1.3 and 2.92 mΩ cm^2 after anodization for tantalum and CVD coated tantalum, respectively.

The superior corrosion stability of tantalum is generally ascribed to formation of a passive oxide layer. Scanning electron microscopy images and x-ray diffraction patterns of tantalum layers before and after anodization (not shown) did not reveal such a layer. However, on the basis of the assumptions regarding the very low thickness of such a surface layer (see discussion below), these methods are not expected to be sufficiently sensitive to provide any useful results.

Contrary to tantalum, titanium corroded upon anodization: After only 5 minutes of anodization a relatively high ICR value of more than 12 mΩ cm^2 was measured. Longer anodization periods resulted in disintegration of the titanium foil. The tantalum oxide layer may be

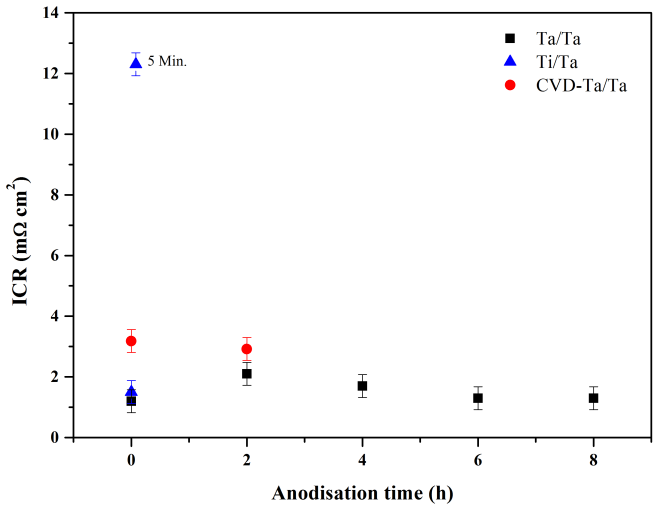

Figure 4.3: *Interfacial contact resistance obtained from plates of tantalum (Ta/Ta), tantalum coated stainless steel (CVD-Ta/Ta) and titanium (Ti/Ta) as a function of anodization time. Anodizations were performed at 130°C, 2 V in 85% H_3PO_4. In all measurements a compaction force of 2.7 MPa was used.*

very thin, causing the mechanism of electron transport to be somewhat complicated. The thickness of the naturally formed oxide layer on tantalum metal was investigated by X-ray photoelectron spectroscopy (XPS) by Lecuyer *et al.* [69] who found that the surface was covered by a 30 nm thick inhomogeneous layer consisting of Ta_2O_5 and large clusters of TaO at the interface between the oxide layer and the metal. Shimizu *et al.* [70] examined the structure of films formed by anodization of a tantalum surface in diluted phosphoric acid, however at very high voltages, up to 60 V. They found by secondary ion mass spectrometry (SIMS) analysis that these films had a duplex structure, consisting of an outer layer containing Ta, O and P, and below that, adjacent to the metal phase, a layer of pure tantalum oxide. The total thicknesses were in the range of 50-70 nm. Thus, the thickness of the oxide layer on the tantalum surface can in our case be assumed to be in the range between 30 and 50 nm, *i.e.* approximately 40 nm. A simple calculation of the resistance of the oxide layer based on the thickness, *e.g.* 40 nm, and the resistivity of Ta_2O_5, 10^{13} Ω cm, [71] would give an area specific resistance of 40 x 10^{10} Ω cm^2. This is clearly a very unrealistic result, when compared to the contact resistance values obtained in this work. One reason for this could be that the surface layer as just described for the anodically formed layer[70], has a more complicated structure and composition than a simple, uniform Ta_2O_5 layer, causing a much higher conductivity. Another, probably more important reason, related to the topography of the surfaces, could be that contact asperities of the ductile tantalum metal are very easily deformed, thereby generating fresh metallic surfaces of the two contact members as soon as a contact is established, providing direct metallic contact. This phenomenon is expected

to be further assisted by the very small oxide layer thickness. Theoretical considerations on the importance of the size of the asperities compared to the mean free path of electrons of the materials involved can be found in the literature. [72] From such considerations the Sharvin resistance and the Holm resistance have been derived. [72] However, these do not take into account the presence of an oxide layer on the surface having a considerably higher resistivity than the bulk metal phase, and are therefore not directly applicable in our case. In case that the oxide layer is very thin, it could occur that the bare tantalum metal is responsible for the electron transport across the contact due to the asperities deformation as outlined. Thus, there might be several phenomena counteracting each other. In any case, it seems very reasonable to conclude that the very good surface contact properties of tantalum are related to the low thickness of its oxide layer.

Extremely low ICR values combined with superior corrosion resistance enable tantalum as a coating materials for these conditions.

4.3 Humidification of gases

Following the literature survey (Chapter 2) it is evident that humidification of the electrolyte has a significant effect on the performance of electrochemical components. Humidifiers were applied to the set-up, enabling humidification of all gases let to the system. The gases were humidified by bubbling them through water before inlet as also reported in [17] and [18].

4.4 Gas sealing and electrical insulation

Different sealing/insulation materials were considered. For example, Viton® (a fluoroelastomer, Dupont^{TM}) has been used by a former member of the group [73]. In that work the plasticity of the material enabled use of the material as an insulating adhesive. In this work, Viton® was used for preliminary measurements (not shown) at lower temperatures (up to 200°C). At higher temperatures, the stability of the material was insufficient for use. Another material had to be used, and due to thermal stability and gas tightness, Kapton® HN (Polyimide film, DuPont^{TM}) was chosen.

Kapton® HN is known for its excellent properties over a wide range of temperatures. The film can be laminated, formed or adhesive coated. (See technical data sheet in Appendix A) It is stable, gas tight and readily available.
For electrical insulation the Kapton HN® sealing was positioned between the endplates and the flowplates, and as gas sealing it was placed between flowplates and electrode/electrolyte.

To investigate the thermal stability, TGA was performed according to Subsection 3.1.1. Figure 4.4 shows such TGA profile from room temperature to 400°C, which suggests thermal stability of the material in the entire temperature range of interest for this work.

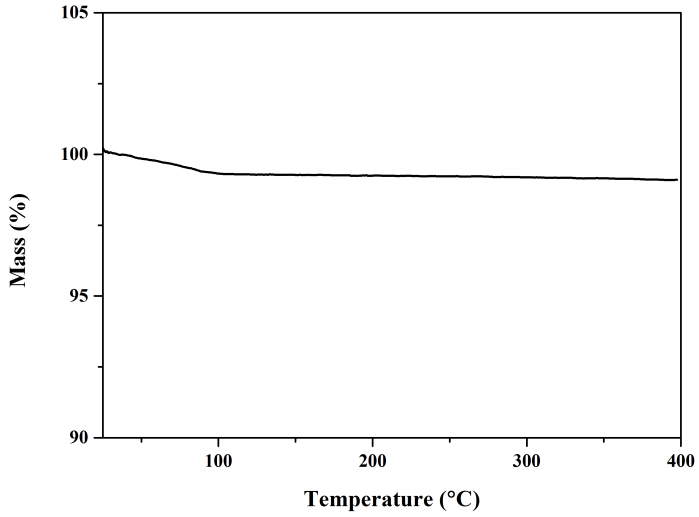

Figure 4.4: *TGA profile of Kapton® HN from 20 to 400°C. The measurement was conducted in air with a heating rate of 10°C min^{-1}.*

Chapter 5

CsH_2PO_4-Based Membrane Electrode Assemblies

As introduced, the most widely used solid acid electrolyte cesium dihydrogen phosphate (CsH_2PO_4) undergoes phase transition at 230°C. With a rise in conductivity from 8.5 x 10^{-6} S cm^{-1} at 223°C to 1.8 x 10^{-2} S cm^{-1} at 233°C this is called a superprotonic phase transition. The superprotonic phase of the phosphate is stable from the phase transition temperature and up to around 250°C under a water partial pressure above 0.2 atm. The high conductivity makes CsH_2PO_4 a potential electrolyte for intermediate temperature fuel cell applications.

In this chapter CsH_2PO_4 is synthesized and characterized. The chapter is divided into three sections, the first section describes the preparation of CsH_2PO_4 electrolyte, electrodes and assembling of MEAs. In the last two sections, these are physically and electrochemically characterized, and compared to already existing literature concerning CsH_2PO_4. One part of the fuel cell demonstrations involves the fabrication of a thin CsH_2PO_4 electrolyte film.

5.1 Membrane electrode assembling

5.1.1 Preparation of electrolyte

CsH_2PO_4 was prepared from an aqueous solution of Cs_2CO_3 (Aldrich, 99%) and H_3PO_4 (Aldrich, 85%). Polycrystalline powder of CsH_2PO_4 was precipitated in methanol. The prepared powder was dried at *ca.* 100°C for several days before use.

The prepared CsH_2PO_4 were characterized by both physical and electrochemical characterizations. Physical characterizations include XRD, SEM and Thermogravimetric analysis performed according to Subsections 3.1.2, 3.1.5 and 3.1.1, respectively. To remove any absorbed water prior to thermal analysis, the samples were preheated at temperatures up to 200°C. For electrochemical characterizations the prepared electrolyte powder was pressed into disk shaped pellets of 13 mm diameter of varying thicknesses. This was done in by uniaxial pressing at 2 x 10^3 kg cm^{-2} at room temperature.

5.1.2 Preparation of electrodes

Four different electrodes were prepared using different GDLs and catalytic compositions as listed below. They are referred to based on the used GDL *i.e.* Toray (Toray paper), Ta (Tantalum coated stainless steel), SS (Stainless Steel) or Carbon (Freudenberg carbon cloth).

1. The 'Carbon' electrodes were made from Carbon cloth (Freudenberg, H2315-C2) GDL wet-proofed with PTFE, with catalytic ink consisting from carbon supported platinum (60 mass% Pt, Johnsson Matthey) and polybenzimidazole (PBI) in formic acid sprayed on top. The catalytic mixture was suspended and treated in an ultrasonic bath for 1 h prior to spraying.

2. The 'Toray' electrodes were made from PTFE treated Torey paper (H120) precoated with a thin layer of carbon (Vulcan® XC72R carbon black) with PTFE binder. The catalytic layer was manually sprayed from a mixture of CsH_2PO_4, Pt black (Aldrich, 99.99%, 27 m^2 g^{-1}) and platinum supported on carbon (60 mass% Pt, Johnsson Matthey) in ethanol. The ratio of the respective components was 1:6:6 by mass with a total loading of 7 mg cm^{-2}. The catalytic mixture was suspended and treated in an ultrasonic bath for 1 h prior to spraying.

3. For the 'SS' electrodes stainless steel felts (316L) (Swiit Metallic Fiber Co. Ltd) were used as GDLs. The catalytic layer was prepared and applied in the same way as for the Toray electrodes.

4. The 'Ta' electrode were prepared from tantalum coated stainless steel felts, the catalytic layer was prepared as for the Toray and SS electrodes.

The prepared electrodes are summarized in Table 5.1.

Table 5.1: *Four gas diffusion layers (GDLs) and two catalytic mixtures used to prepare electrodes.*

Name	**GDL**	**Catalytic layer**	**Pt loading mg cm^{-2}**
Carbon	Carbon cloth (Freudenberg)	Pt/C + PBI	0.7
Toray	Carbon paper (Toray)	Pt/C + Pt black + CsH_2PO_4	7.0
SS	Stainless steel (316L)	Pt/C + Pt black + CsH_2PO_4	7.0
Ta	Tantalum coated stainless steel (316L)	Pt/C + Pt black + CsH_2PO_4	7.0

5.1.3 Assembling of MEAs

Three types of MEAs were prepared. In the first type, **A**, two similar electrodes were used on the sides of an electrolyte as shown in Figure 5.1. For the second type, **B**, two different types of electrodes were used. For MEA **A** and **B**, different ways to assemble the MEAs

were investigated. In order to promote contact between the electrodes and electrolyte, it was attempted to press the assemblies both by cold and hot pressing, however poor mechanical behaviour of the pressed powder complicated this procedure. Instead the layers were placed in fixed positions in the cell and after heating to minimum 100°C the cell was tightened. Preliminary investigations were made in order to establish how much the cell could be tightened to promote contact between layers. For example, when using CsH_2PO_4 a torque force of 0.35 Nm was used. A lower force resulted in lower current densities of the fuel cell measurements due to the lack of contact, and a higher torque force resulted in deformation of the electrolyte and thereby lowering the validity of the electrolyte thickness estimation. Furthermore, a very high torque force resulted in deformation of the electrode.

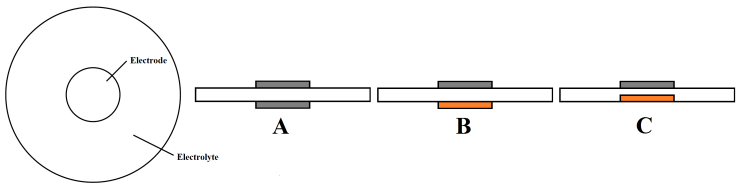

Figure 5.1: *Schematic illustration of the three MEAs used for characterizations of electrolyte materials as well as electrodes and full cell performance. Left: top view of the MEAs; A:Symmetrical cell; B: two electrode cell with two different electrodes; and C; slurry cast electrolyte MEA with two different electrodes. Anode (gray) and cathode (orange).*

In the third type, **C**, it was attempted to prepare thin film electrolytes by slurry casting. Slurry's can be prepared by mechanically mixing the powder with a solvent. In this work three different suspension media were used: water, ethanol and toluene. Slurries were made with CsH_2PO_4 powder and ethanol or toluene suspension medium, which were poured onto the electrode (cathode) forming evenly dispersed layers. With water as suspension medium, no useful results were achieved and this is therefore not considered any further. By using toluene and ethanol as suspension media, thin layers could be prepared.

5.2 Physical characterizations

5.2.1 X-ray diffraction of CsH_2PO_4

The phase purity of prepared CsH_2PO_4 was revealed by room temperature X-ray diffraction (XRD) (Figure 5.2). The experimentally measured diffraction pattern for CsH_2PO_4 was compared to a simulated pattern from JCPDS (not shown). The two patterns were found to be in excellent agreement, thus confirming the crystalline structure of the synthesized powder to be that of CsH_2PO_4.

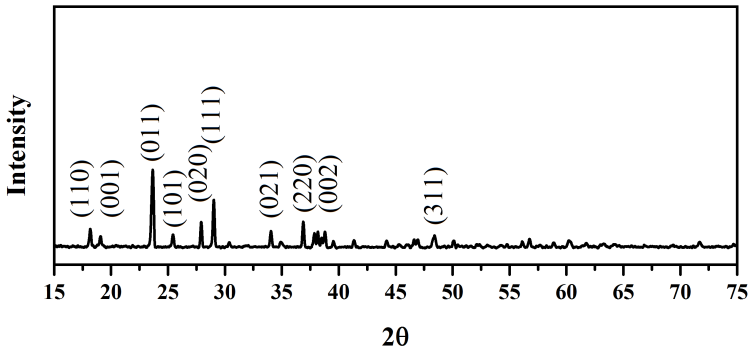

Figure 5.2: *XRD profile of synthesized CsH_2PO_4. Monoclinic CsH_2PO_4 is indexed according to JCPDS Card No. 00-35-0746. [74].*

5.2.2 Thermal analysis of CsH_2PO_4

The results, both in terms of the weight loss (thermogravimetric, TG) and differential thermal analysis (DTA) curves are shown in Figure 5.3. Expected weight loss values corresponding to the formation of $CsH_2P_2O_7$ and $CsPO_3$, 3.92 and 7.84 wt%, respectively, are illustrated in the figure for comparison. The DTA signal reveals thermal events with peaks at 234°C and 273°C which are accompanied with a weight loss, the total being in excellent agreement with the theoretical weight loss to form $CsPO_3$. At temperatures above 230°C, dehydration of CsH_2PO_4 started with the formation of pyrophosphate ($Cs_2H_2P_2O_7$) leading to a weight loss of 3.9 %. During subsequent heating further dehydration takes place, leading to higher polymerization of the phosphate.

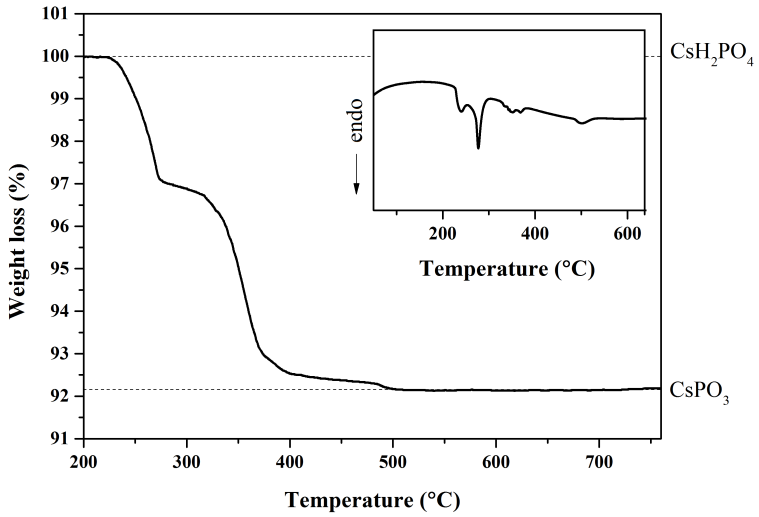

Figure 5.3: *Thermal analysis of CsH_2PO_4 measured with a heating rate of $10°C\,min^{-1}$ under argon atmosphere: weight change (TG curve); inset: differential thermal analysis (DTA).*

Accordingly, the DTA signal for CsH_2PO_4 showed three thermal events at 234, 274 and 345°C. The first two due to dehydration to form dimer and higher polymers of phosphates, were accompanied with weight losses, the total of which was reached at temperatures above 500°C for the formation of $CsPO_3$. Two steps can be described by the reaction pathway as in reaction 5.1.

$$CsH_2PO_4 \rightarrow Cs_2H_2P_2O_7 \rightarrow CsPO_3 \tag{5.1}$$

Obtained results are in agreement with results obtained from Yu-ki Taninouchi *et al.* [75] who performed a thorough investigation of the dehydration behavior of CsH_2PO_4.

5.2.3 Microscope images of CsH_2PO_4 powder and electrolyte, electrodes and MEA

Figure 5.4 shows an image of the prepared CsH_2PO_4 powder, and two cross sections of a CsH_2PO_4 pellet electrolyte. It appears that the synthesized powder is comprised of particles of around 4 μm which are agglomerated in clusters. From pressing the powders it was possible to obtain coherent pellets, which appeared dense (bottom image). Taking a closer look (middle image), the pressed CsH_2PO_4 appears porous with crystalline networks.

Figure 5.5 shows light microscope images of stainless steel electrodes and tantalum coated stainless steel electrodes sprayed with catalytic layers. When spraying on stainless steel the adhesion of the catalyst layer was very poor, whereas when sprayed onto tantalum coated stainless steel the adhesion of catalyst seems good. Images were also made using Toray paper and carbon cloth (not shown), which appeared similar to those using tantalum coated stainless steel indicating sufficient adhesion.

SEM images of Ta and Toray electrodes are shown in Figure 5.6. On both electrodes, the high loading seem to ensure complete coverage of the fibers.

5.3 Electrochemical characterizations

5.3.1 Conductivity of CsH_2PO_4

Figure 5.7 shows the measured AC impedance spectra of CsH_2PO_4 below and above the phase transition temperature and a water partial pressure of 0.3 atm. The shapes of the spectra are in good agreement with reported spectra from Otomo *et al.* [76] who measured the conductivity of CsH_2PO_4 in dry and humid atmospheres (gaseous 30% H_2O/Ar mixture) on pellet samples. In the low temperature range, a semicircle is observed, which becomes smaller with increasing temperature (not shown). From the semicircle the electrolyte resistance is determined as the intercept with the Z_{real} axis at low frequencies. Above the transition temperature no semicircles are observed due to fast ionic conduction. The resistance was determined as the intercept on the Z_{real} axis at high frequencies and the conductivity,

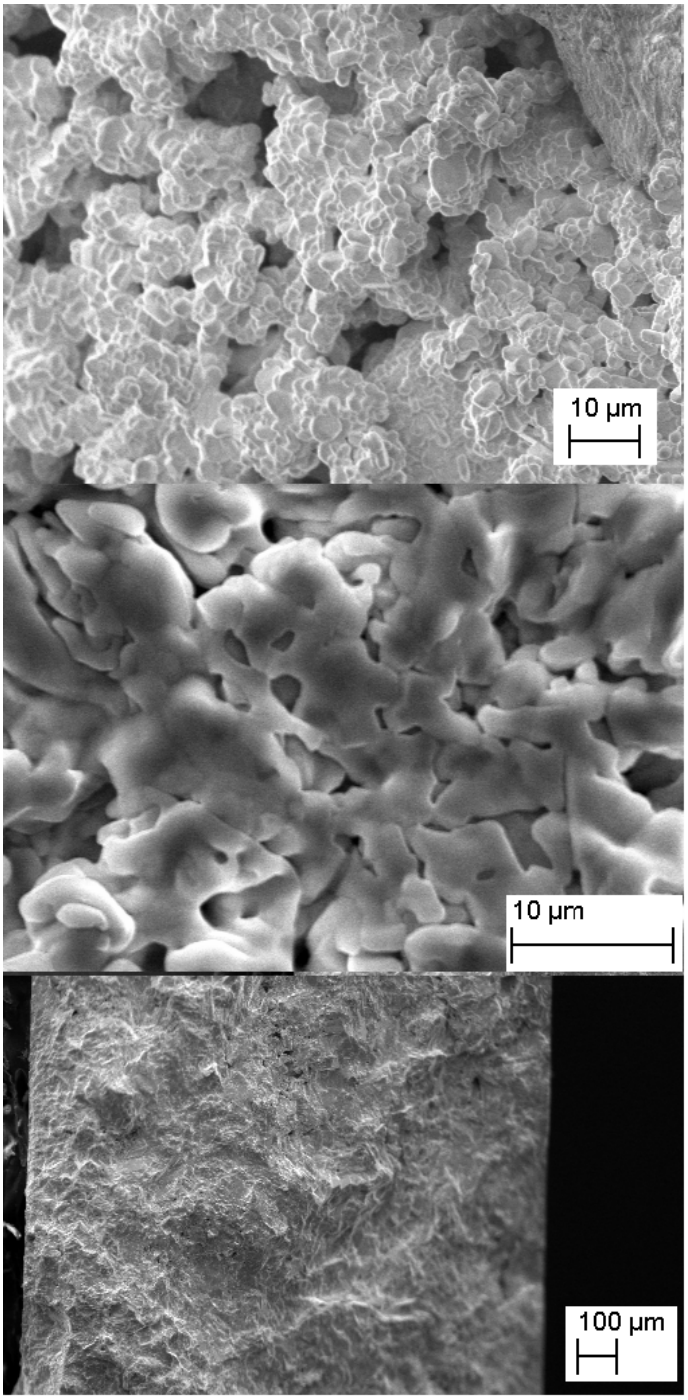

Figure 5.4: *SEM images of top: CsH_2PO_4 powder; middle: cross section of a pressed CsH_2PO_4 pellet, and bottom: higher magnification of cross-section of CsH_2PO_4 pellet electrolyte.*

σ, was calculated from the measured resistance as described in Section 3.2 (Equation 3.5).

Figure 5.8 shows the measured conductivity *vs.* temperature of the prepared CsH_2PO_4 at pH_2O=0.3 atm during two heating and cooling cycles. The results appear to be in agreement with former reported literature *e.g.* from Haile *et al.* [77]. A sharp increase in the con-

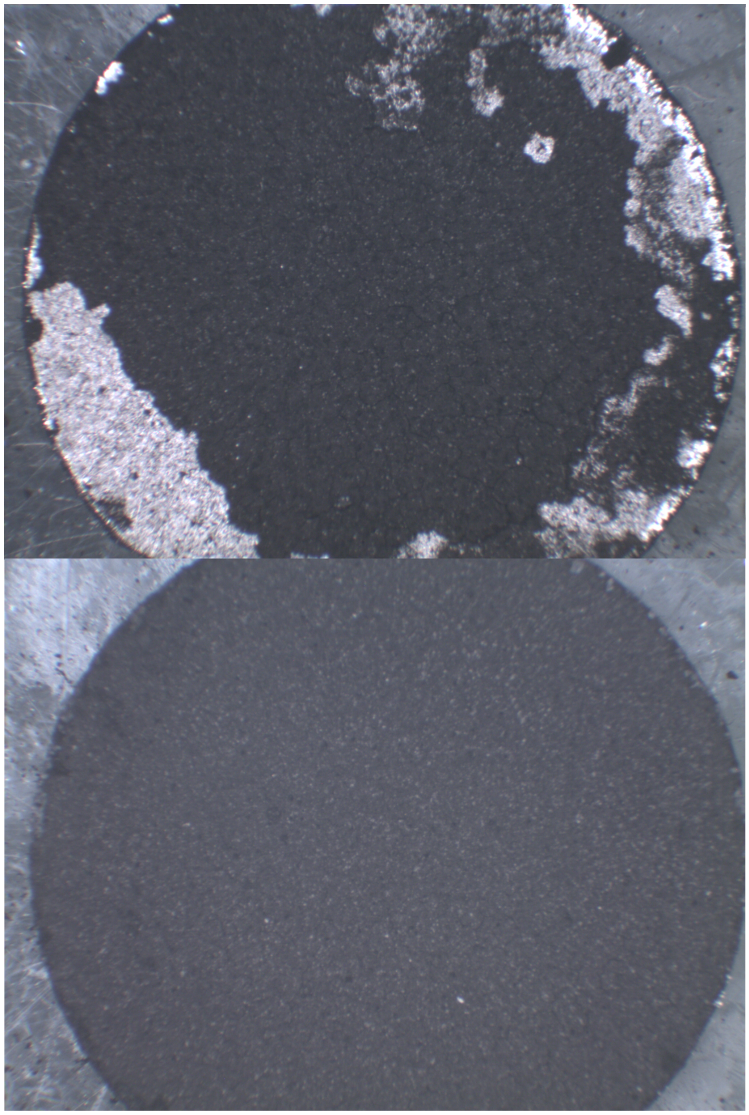

Figure 5.5: *Light microscope images of Pt/C, Pt black and CsH_2PO_4 sprayed on top: a stainless steel GDL; and bottom: a tantalum coated stainless steel GDL.*

ductivity is observed associated with the phase transition of CsH_2PO_4 as discussed earlier (Chapter 4).

It has been debated whether the sharp increase in conductivity of CsH_2PO_4 is a result of a true phase transition or decomposition/dehydration. Haile *et al.* [77] compared 26 publications from 1977 to 2005, supporting or opposing the conclusion of a superprotonic transition. Some authors reported that CsH_2PO_4 undergoes polymorphic phase transition at 228°C $\pm$ 2°C under atmospheric pressure with an enthalpy of 49.0 J g^{-1} $\pm$ 2.5 J g^{-1}, and that this is accompanied by an increase in conductivity, the extent of which depending on the sample. Other authors were dismissing the theory of a phase transition, proposing that the increase was merely due to water leaving the structure. Haile *et al.* concluded that there was evidence supporting the conclusion that CsH_2PO_4 undergoes a true, polymorphic tran-

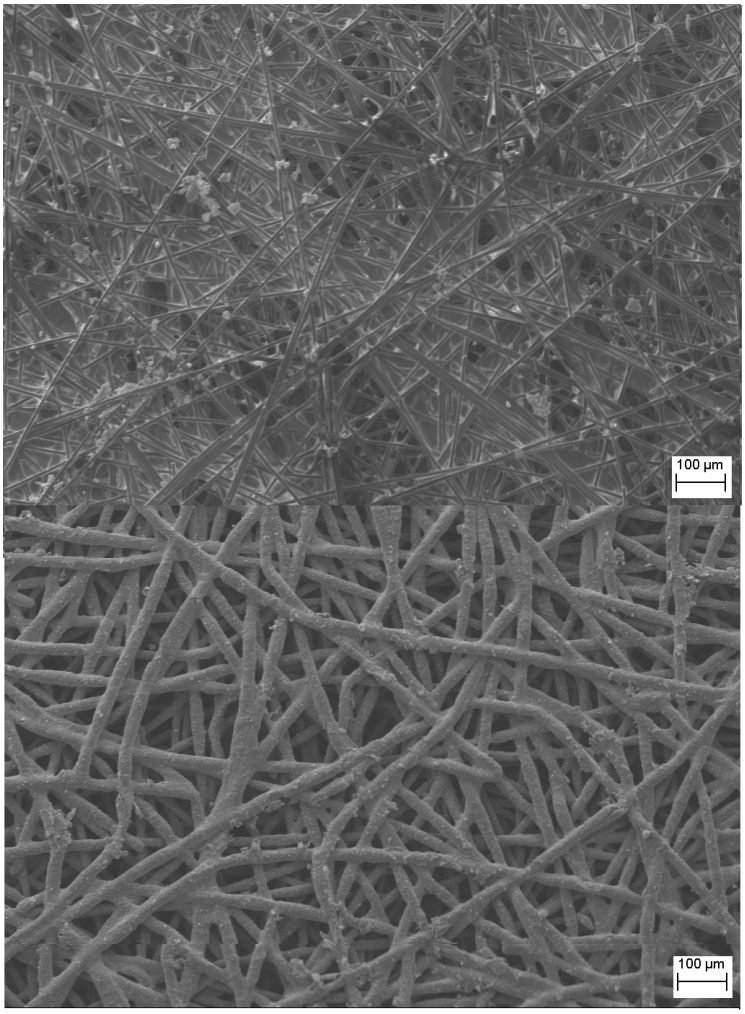

Figure 5.6: *SEM images of top: a Toray electrode and bottom: a Ta electrode.*

sition and that with sufficient humidification, high and stable values of conductivity can be achieved above 230°C. Otomo *et al.* [20] investigated the conductivity of CsH_2PO_4 under various humidity conditions. At 250°C a minimum water partial pressure of 20% was found sufficient to suppress the phosphate dehydration and to maintain the superprotonic conductivity level of around 1 x 10^{-2} S cm^{-1}. The level of conductivity was furthermore found not to increase with increasing humidity (pH_2O between 0.2 and 0.9 atm). With a water partial pressure of 0.3 atm the conductivity was found to increase monotonically with temperature from 230°C to 280°C, above which temperature the conductivity started to fluctuate due to melting and dehydration. A sudden drop in conductivity occurred at 300°C. With 90% H_2O the high conductivity was extended to 300-310°C before a sudden drop. For comparison, Haile *et al.* [77] reported a conductivity of 2.2 x 10^{-2} S cm^{-1} at 240°C and 40% H_2O.

5.3.2 Hydrogen cells

Figure 5.9 shows polarization curves for CsH_2PO_4 with thicknesses of 200, 400 and 600 μm performed in humidified hydrogen at 250°C. The linear response suggests ohmic control

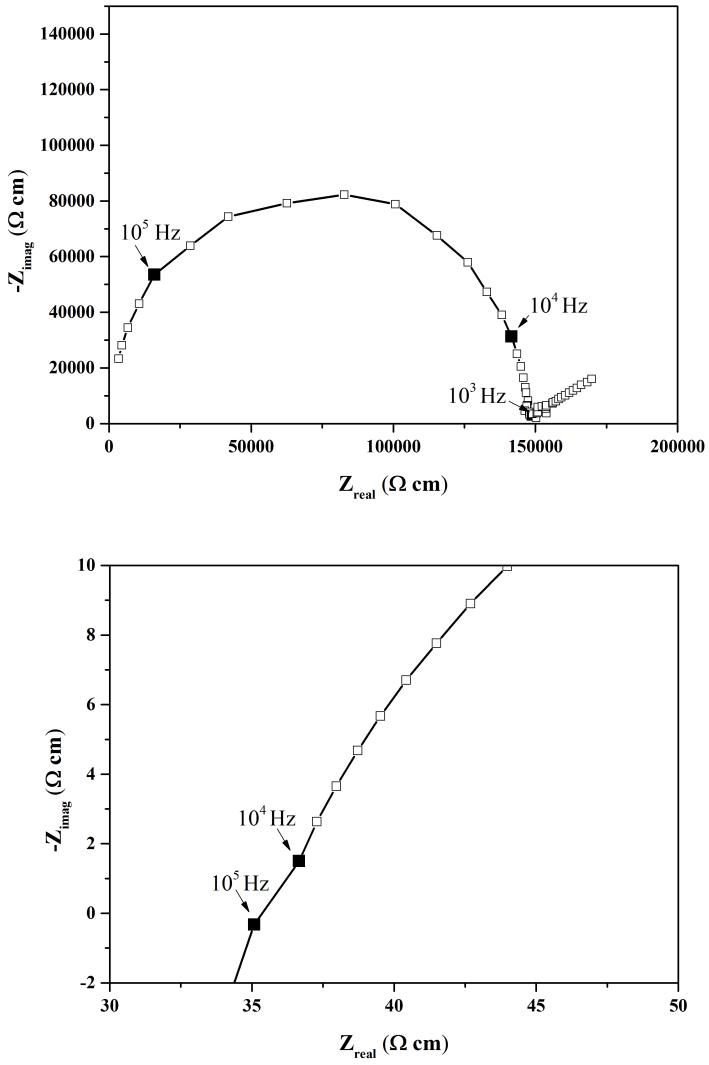

Figure 5.7: *Measured impedance spectra resulting from Ag|CsH_2PO_4|Ag under humidified air (pH_2O=0.3 atm) systems, top: at low temperature; and bottom: at high temperatures.*

and therefore the apparent conductivity can be calculated. Dotted lines shows calculated polarization curves with area specific resistances (ASR) of 1, 2, and 3 Ω cm^2. A thickness of 400 μm divided by 2 Ω cm^2 suggests a conductivity of 2.0 x 10^{-2} S cm^{-1} which is also the case for the two other measurements. Such polarization curves were performed at temperatures up to 270°C (not shown) all indicating ohmic control and with a small increase in conductivity as was also seen in Figure 5.8.

Figure 5.10 shows an iR corrected impedance spectrum obtained from Pt|CsH_2PO_4|Pt under humidified hydrogen (p_{H_2O}=0.3 atm) at 250°C. The impedance measurements indicate that the area specific anode polarization is around 0.175 Ω cm^2 (under zero bias).

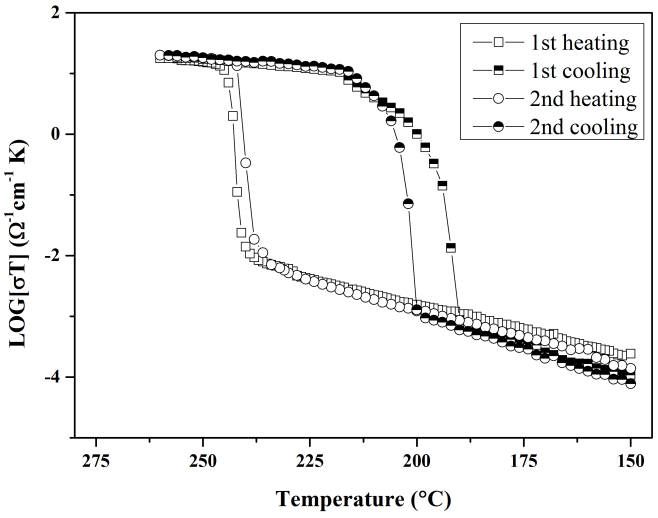

Figure 5.8: *Conductivity of Ag|CsH_2PO_4|Ag under humidified air (pH_2O=0.3 atm) for two heating and cooling cycles.*

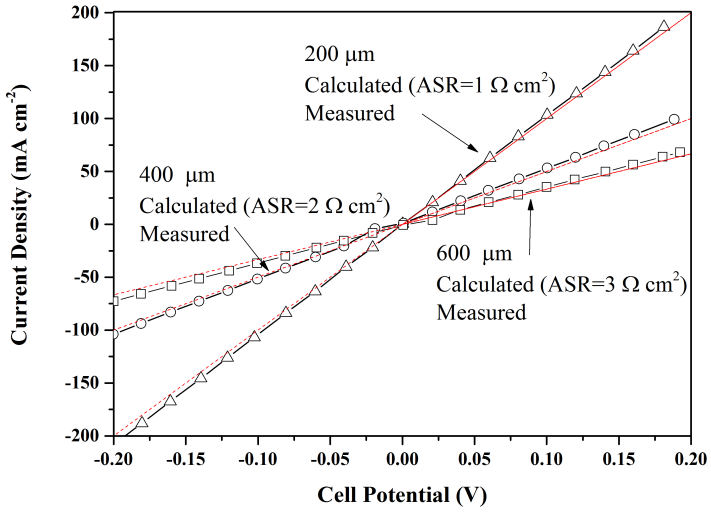

Figure 5.9: *Hydrogen evolution polarization curves of Toray|CsH_2PO_4|Toray MEAs (uncorrected for iR_Ω) at different thicknesses. Red dotted lines indicate calculated values. pH_2O=0.3 atm; Pt loading=7 mg cm^{-2}.*

Figure 5.11 shows and example of a stability measurement performed with CsH_2PO_4 electrolyte exposed to humidified hydrogen at 250°C and -0.2 V. Such cell remained stable over a time period of around 100 h, though with some variation. This indicates some stability of the electrodes and electrolyte at these conditions.

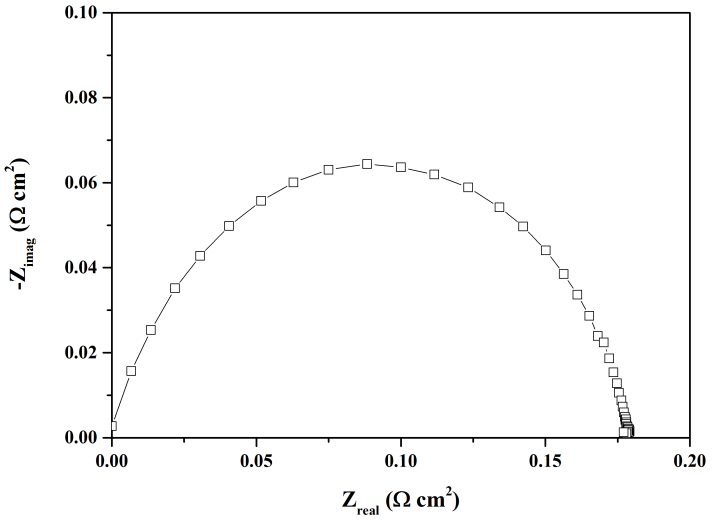

Figure 5.10: *iR corrected impedance spectrum obtained from a Toray|CsH_2PO_4|Toray under humidified hydrogen (p_{H2O}=0.3 atm) at 250°C. Pt loading=7 mg cm^{-2}.*

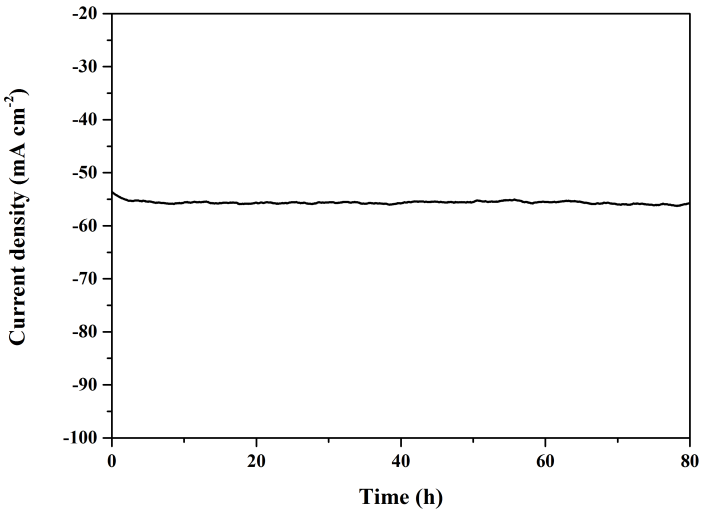

Figure 5.11: *Stability of a Toray|CsH_2PO_4|Toray MEA at 250°C in H_2/H_2 at 70°C dew point and -0.2 V working electrode potential. Pt loading=7 mg cm^{-2}; Electrolyte thickness=600 µm.*

5.3.3 Impedance measurement in air

An example of a Nyquist plot obtained at OCV for cells exposed to humidified air to one side and humidified hydrogen to the other side at 250°C is shown in Figure 5.12. When measured in air the area specific cathode polarization resistance under zero bias is around 20 Ω cm^2 and thus it is in agreement with Haile *et al.* [77] who also reported significantly larger area specific cathode polarization resistance than area specific anode polarization

resistance.

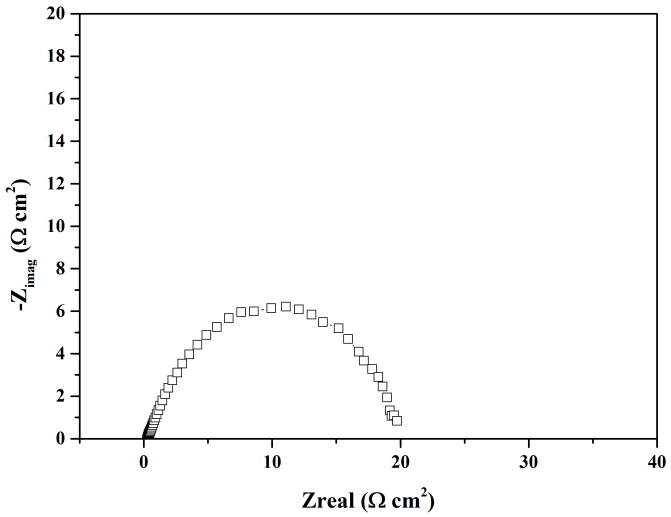

Figure 5.12: *iR corrected Nyquist plot obtained from a Toray|CsH_2PO_4|Toray MEA under humidified air (p_{H_2O}=0.3 atm) at 250°C. Pt loading=7 mg cm^{-2}.*

5.3.4 H_2/air cells

For CsH_2PO_4 based fuel cell measurements, four different gas diffusion layers were tested according to Table 5.1. To compare the prepared electrodes, OCV measurements, impedance measurements, hydrogen concentration cell measurements and fuel cell measurements were performed.

OCV measurements

For OCV measurements electrolyte thicknesses of *ca.* 600 μm were used. MEAs were assembled with the prepared gas diffusion electrodes on each side of the phosphate pellets (Figure 5.1). Table 5.2 sums the highest open circuit potentials measured for the different electrodes. When using Torey paper, stainless steel and tantalum coated stainless steel, the OCVs are high > 0.9 V at all temperatures. High OCVs were achieved when using stainless steel gas diffusion layer, however the catalytic layer was detached from the stainless steel GDL and subsequent to measurements corrosion was observed (Figure 5.5). When using the carbon cloth based electrodes poor OCVs were achieved (ca. 0.6 V).

Many factors influence the OCV of a fuel cell. In Section 3.2.2 it was stated that the theoretical voltage of a fuel cell is in the area of 1.23 V, but that this is never fully reached. The reasons for voltage loss during operation were introduced, however losses occur even at open circuit potentials. Zhang *et al.* [78] analyzed the deviations of the measured OCV from theoretical OCV in a PEM fuel cell. They concluded that the main reason for losses in their fuel cell are mainly due to the mixed potential of the Pt/PtO catalyst surface and

hydrogen crossover. It is likely that these factors are influencing the measurements in this work. For CsH_2PO_4 based cells Boysen *et al.* [17] reported high OCV (1 V) (Pt loading 18 mg cm^{-2}) for their fuel cell and Otomo *et al.* [20] reported an OCV of 0.945 V (Pt loading of 1.6 mg cm^{-2}), and suggested that the deviation from the theoretical potential was due to gas leakage. In this work, OCVs are intermediating these values as for example an OCV was measured as 0.965 at 250°C for a Toray|CsH_2PO_4|Toray MEA.

Table 5.2: *Measured OCVs for the four different electrodes at various temperatures.*

Electrode	**Temperature (°C)**	**OCV**
Carbon	250	0.6
Toray	235	0.976
	250	0.965
	275	0.926
SS	250	0.973
Ta	250	0.90
	260	0.90
	270	0.86

High OCVs are achieved with a high platinum loading (7 mg cm^{-2}), and it is naturally of interest to lower the amount of the expensive catalyst. Papandrew *et al.* [79] obtained slightly improved electrodes by depositing Pt nanoparticle network on CsH_2PO_4. In this way the loading could be decreased from 7.5 mg cm^{-2} as previously reported to 1.75 mg cm^{-2} without losing performance. Further reductions in catalyst loadings were made by Varga *et al.* [80] who prepared electrodes by electrospray deposition. In this way they decreased the Pt loading to 0.3 mg cm^{-2} for the fuel cell anode without performance loss. These results indicate that several routes for reduction of the platinum loading are available.

Polarization curves

In the section above it was found that the OCVs were varying with the choice of gas diffusion layer. It is believed that a lowered OCV when using tantalum coated stainless steel was caused by the stiffness of the electrode which may form gas leaks. However, problems with carbon based construction materials, particularly at the cathode side were addressed in Section 2.4. Therefore it was also attempted to make fuel cells with tantalum coated gas diffusion layers. Polarization curves of cells Toray|CsH_2PO_4|Ta and Toray|CsH_2PO_4|Toray are compared in Figure 5.13. The iR free polarisation curve is indicated on the figure as well. From the figure it can be seen that the two MEAs are performing equally.

Cells similar to the above except electrolyte thicknesses of 200 μm are compared in Figure 5.14. When using both Toray and Ta the OCV is lower when using Toray on both sides of the electrolyte, however, a higher current density is achieved when using Toray and Ta together. Maximum current and power densities were measured as 295 and 344 mA cm^{-2}, and 53.8 and 50.1 mW cm^{-2}, for the Toray|CsH_2PO_4|Toray and Toray|CsH_2PO_4|Ta MEAs.

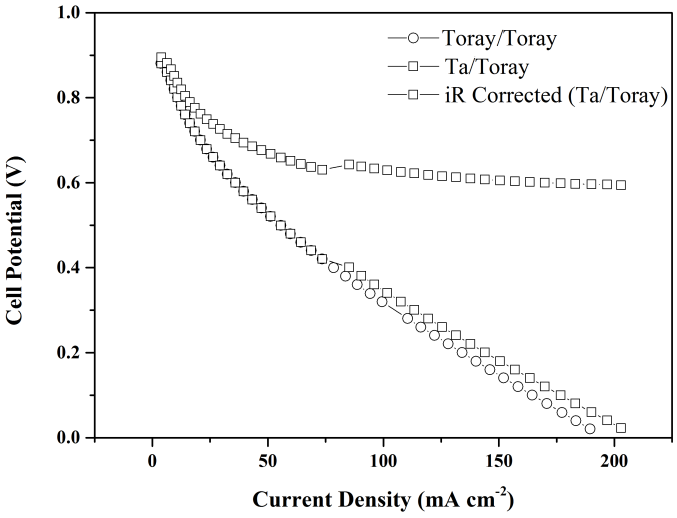

Figure 5.13: *Fuel cell polarization curves (and iR free polarization curve) from Toray|CsH_2PO_4|Toray and Toray|CsH_2PO_4|Ta MEAs. Temperature=250°C; pH_2O=0.3 atm; Pt loading=7 mg cm^{-2}; Electrolyte thickness=600 µm.*

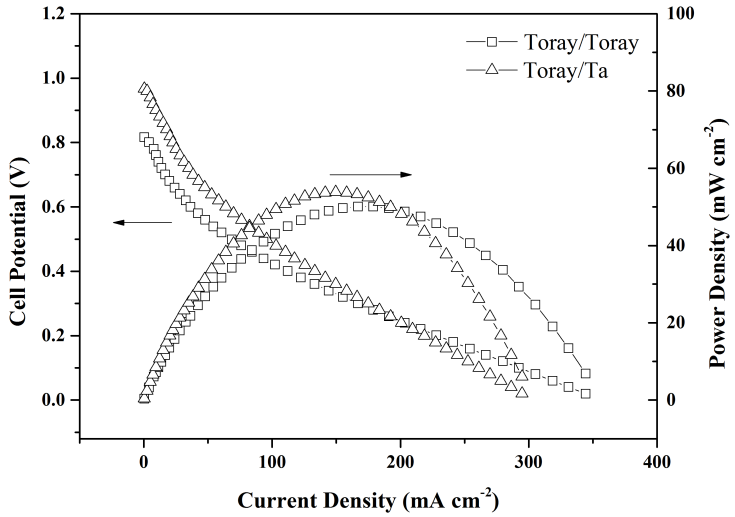

Figure 5.14: *Fuel cell polarization Toray|CsH_2PO_4|Toray and Toray|CsH_2PO_4|Ta MEAs. Temperature=250°C; pH_2O=0.3 atm; Pt loading=7 mg cm^{-2}; Electrolyte thickness=200 µm.*

Stability measurements

Figure 5.15 shows a stability measurement of a Toray|CsH_2PO_4|Ta fuel cell at 250°C and 70°C dew point. (0.2 V) Initially (first 5 hours) there seems to an increase in the current density where after the current density slightly decreases throughout the experiment. Moreover, small variation in the measurement appeared throughout the whole experiment.

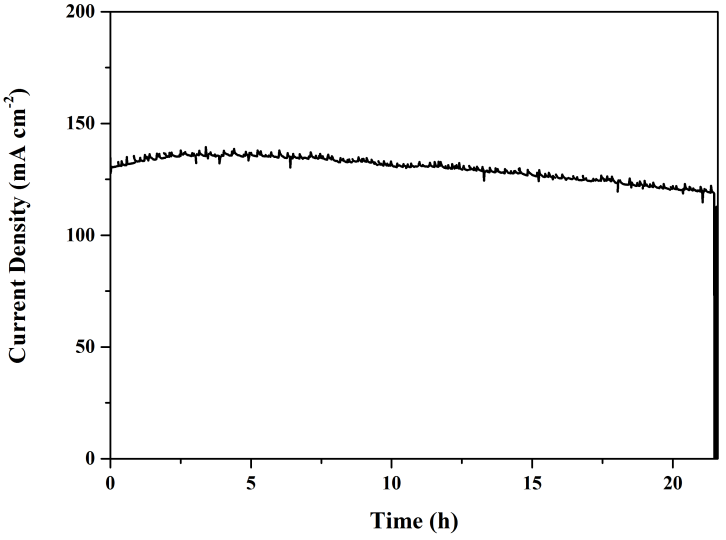

Figure 5.15: *Stability measurement of a Toray|CsH_2PO_4|Ta MEA at 0.2 V, 250°C and 70°C dew point. Pt loading=7 mg cm^{-2}; Electrolyte thickness=600 μm.*

Thin film fuel cells

One way to limit the ohmic resistance of a fuel cell is to use a thin electrolyte. The inorganic nature of CsH_2PO_4, however, makes it difficult to prepare a thin and robust membrane with high proton conductivity. [81] As the phosphate cannot be sintered at high temperatures, other preparation methods must be used. A few attempts to fabricate thin layer of CsH_2PO_4 have been reported in literature. *E. g.* A. G.-Urtiaga *et al.* [81] prepared CsH_2PO_4 by electrospinning and succeeded in the fabrication of a 50 μm fiber mat. The maximum proton conductivity achieved was 8 x 10^{-3} S cm^{-1} at 250°C. The value of conductivity is somewhat lower than reported from other authors, probably owing to the low density of the layer. From their results it was suggested that for the fabrication of a dense mat subsequent addition of a polymer is required. In Chapter 2 it was mentioned that the highest fuel cell performance seen at intermediate temperatures were achieved by T. Uda and S. M. Haile [21] who prepared thin CsH_2PO_4 membranes (25-36 μm). In their work the fuel cells were fabricated by slurry deposition with toluene as a suspension medium and a stainless steel GDL also served as mechanical support. Onto this an electrocatalytic layer, electrolyte layer and second electrocatalytic layer was deposited. The structure was pressed to provide contact between the layers.

In this work it was attempted to measure fuel cell performance using MEA **C**, *i.e.* thin film MEAs prepared by slurry deposition using ethanol or toluene as suspension medium. Various polarization curves were made, each time resulting in different performances. The erratic performance, which was also reported by Uda *et al.* [21]. Figure 5.16 shows the best

polarization curves obtained using such MEAs. In general, better results were achieved when using toluene compared to ethanol, as both the OCVs, current densities and power densities were significantly improved. This is also clear in the figure. Current and power densities of the cell with the electrolyte dispersed from toluene were measured as 276 mA cm^{-2} (at 250°C) and 313 mA cm^{-2} (at 270°C), and 61 mW cm^{-2} (at 250°C) and 75.6 (at 270°C) mW cm^{-2}, respectively.

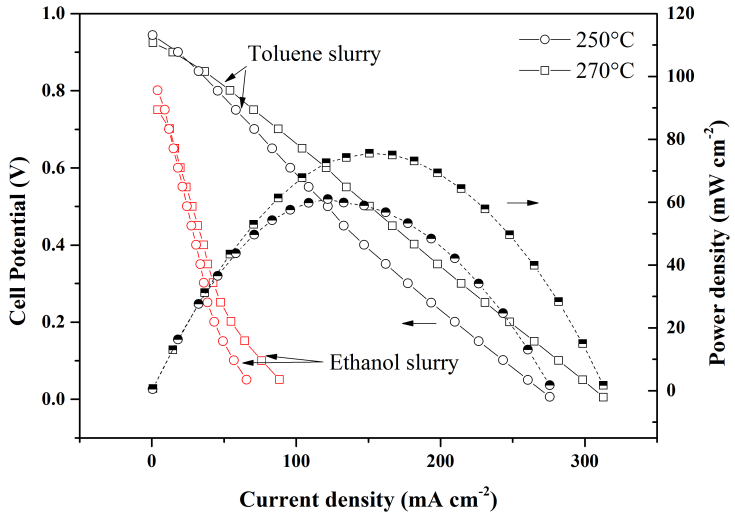

Figure 5.16: *Best fuel cell characteristics obtained using electrolytes fabricated by slurry deposition of the CsH_2PO_4 electrolyte with ethanol and toluene as suspension medium. Polarization curves were collected at 250 and 270° C. PH_2O=0.3 atm; Pt loading=7 mg cm^{-2}.*

5.4 Summary

CsH_2PO_4 was successfully prepared, XRD indicated that the prepared powder was phase pure and thermogravimetric analysis corresponded well with formerly reported results.

For conductivity, hydrogen pump and fuel cell experiments, pellets were pressed with 2 x 10^3 kg pr cm^2 into different thicknesses. Resulting pellets were coherent and had thicknesses from 0.2 to 1 mm. Conductivity measurements performed by impedance in air were in agreement with formerly reported literature and polarization curves performed with H_2/H_2 confirmed these measurements. Furthermore no significant overpotential for the hydrogen oxidation or evolution reaction was observed at these conditions. A H_2/H_2 cell was demonstrated for more than 100 h indicating stability of all components at these conditions.

In this work prepared electrodes were evaluated by means of microscopic images, OCV, impedance spectroscopy in hydrogen and air, and hydrogen/hydrogen and hydrogen/air polarization curves. From the literature review it was found that carbon paper suffers from

instability at the working conditions of fuel cells, particularly on the cathode side. The corrosion becomes even more severe at higher temperatures and therefore it was attempted to use other alternatives. Stainless steel was tested as an alternative, this however suffered from corrosion, and furthermore poor adherence of the electrocatalytic on the GDL layer was observed. As our research group has good experience with the use of tantalum as a surface coating for stainless steel, this was applied. Such coatings were concluded to posses extremely high corrosion resistance with the additional benefit of extremely low contact resistance. For use as GDL the tantalum coated stainless steel was furthermore found to have good adherence with the electrocatalytic layer.

In the H_2/air cells varying OCVs were measured. Also in literature different OCVs have been reported, even for similar systems, and reasons here fore were discussed. In this work, Toray paper on both anode and cathode resulted in high OCVs (around 1 V), though decreasing with temperature. Using tantalum coatings somewhat decreased the OCV, particularly when used both for anode and cathode at high temperatures. It is believed that the stiffness of the tantalum containing electrode has a negative effect on the OCV due to increased gas leakage, though no further evidence for this is provided. When using Toray paper as GDL on the anode side and tantalum coated stainless steel on the cathode side, the OCVs were decreased, however, current densities of such fuel cells were similar, even slightly increased.

Fuel cell polarization curves were demonstrated at various temperatures and electrolyte thicknesses, resulting in good performances comparable to [17]. An interesting and important topic is the choice of support material. Carbon is the most commonly used support for platinum, but is known to oxidize under fuel cell conditions. In this work a fuel cell was running for more than 20 hours and the performance was somewhat decreasing over time. It was not fully investigated what caused the decrease, nevertheless an alternative to carbon support is expected to improve the overall fuel cell characteristics.

It was attempted to fabricate thin films of CsH_2PO_4 by slurry casting with ethanol and toluene suspension mediums. By using toluene as suspension medium the fuel cell power density was somewhat improved compared to measurements with pressed electrolyte pellets. For example, 61 mW cm^{-2} was achieved for the thin film fuel cell compared to 53.8 mW cm^{-2} achieved when using a thin pellet electrolyte at 250°C. This improvement is believed to be due to improved contact between electrolyte and electrocatalytic layer rather than thinning of the electrolyte. For the cells using thin films, mechanical issues of CsH_2PO_4 became more severe, and such fuel cells were neither stable nor reproducible. This is in agreement with reported results [21] where varying outputs were observed and long term stability could not be achieved with the thin electrolyte.

Impedance measurements were performed on MEAs both in hydrogen and in air, indicating

that the cathode overpotential was significantly larger than the anode overpotential. This is in good agreement with the polarization curves as those measured in H_2/H_2 were found to be in agreement with the conductivity measurements, while those measured in H_2/air fuel cell polarization curves had a large additional voltage loss. Accordingly, improving the fuel cell cathode will improve the overall performance.

From the combination of experimental work and literature research, it is clear that there is a large potential for the development of CsH_2PO_4 based fuel cells and merely demonstrations have been given. Improvements of intermediate temperature CsH_2PO_4-based fuel cells include mechanical stabilization of the plastic CsH_2PO_4, better catalyst utilization or the finding of alternatives to Pt. Furthermore other support materials should be considered. So far, CsH_2PO_4 seems to be the most promising electrolyte for this temperature range, but with the shortcomings of this material, improvements or the finding of other materials is critical for the realization of a high performance stable intermediate temperature fuel cell.

Chapter 6

Development of CsH_2PO_4 Electrolytes

From the literature survey (Chapter 2) and experimental work performed with CsH_2PO_4 (Chapter 5) it was found that in order to fabricate a stable high performance fuel cell using CsH_2PO_4, improvements of the electrolyte properties were required. Thus for the use of CsH_2PO_4 as electrolyte, it must fabricated in a composite with at least one additional compound.

Improvements of the CsH_2PO_4 electrolyte can be achieved in terms of enhanced low temperature conductivity, extended transition temperature range, water retention and strengthened mechanical behaviors. As will be discussed throughout this chapter, the properties of CsH_2PO_4 can be improved by several mechanisms. Solid acid-based composites have formerly been presented in literature, generally in composites with:

- **Inert oxides:** Oxides including SiO_2, Al_2O_3, TiO_2 or perovskite-like zirconate ($SrZrO_3$) have been reported to physically stabilize the conductive phase towards lower and higher temperatures, or to promote disordering at the interface and thereby extending the high conductivity phase. Moreover composite formation with oxides is expected to improve water retention.

- **Phosphates:** Doping with other phosphates, *e.g.* SiP_2O_7 has resulted in the formation of a new low temperature (>150°C) conducting phase, $CsH_5(PO_4)_2$, and thereby extending the temperature range of high proton conduction towards lower temperatures.

- **Organic basic compounds:** Formation of inorganic-organic composites (*e.g.* with Guanine and tautomers) has been suggested to induce acid-base interactions *via* hydrogen bonding between the compounds, with a corresponding improvement in conductivity. Moreover, it is believed that the use of polymers facilitates the fabrication of thin and dense electrolyte layers.

Thus it is possible to improve the properties of CsH_2PO_4 electrolytes. Though research has been reported to improve the properties of electrolytes, very few have been demonstrated in

fuel cell assemblies.

In this chapter compounds will be evaluated in composites with CsH_2PO_4. First section uses oxides, SiO_2, TiO_2 and ZrO_2, in second section CsH_2PO_4 is prepared in composites with a phosphate, $NdPO_4$, and in the third section, CsH_2PO_4 is prepared in inorganic-organic composites, as it is mixed with melamine cyanurate.

6.1 CsH_2PO_4/Oxide composite electrolytes

6.1.1 Background and introduction

Composite forming has been widely used to improve the properties of solid state ionic conductors. By forming composites from solid acids and oxides, the properties of the solid acids have shown to improve in terms of adsorption and water retention up to high temperatures. Further improvements have been achieved in terms of thermal and mechanical stability. One possibility is to use the mechanically strong nature of the oxide to prepare a strong matrix into which the proton conducting phase can be incorporated. For inert oxides a relatively low concentration is sufficient for optimal conductivity, above a critical concentration, a continuous contact between the oxide particles is formed, and the conductivity will decrease due to a blocking effect of the oxides. [46, 82, 83, 84]

The most investigated solid acid based composites have been prepared by mixing CsH_2PO_4 with Al_2O_3, TiO_2 or SiO_2. By forming composites with SiO_2 the superprotonic temperature range of CsH_2PO_4 was extended towards lower temperatures. [38, 76, 85] For example, Ponomoreva *et al.* [38] achieved interesting results including CsH_2PO_4 in composites with SiO_2 in various ratios. They found that composites exhibited high proton conductivities, 10^{-3}-10^{-2} S cm^{-1} between 130 and 250°C. Moreover the CsH_2PO_4/SiO_2 composites had higher thermal stability at lower water partial pressures when compared to the pure CsH_2PO_4. Baranov *et al.* [86] discussed the effect of doping with oxides, and fabricated proton conducting composites from fibrous alumina skeletons impregnated with CsH_2PO_4 which exhibited conductive properties with enhanced thermal stability and mechanical stability. Bochetta *et al.* [87] succeeded in the fabrication of a thin (50 μm) membrane using anodic alumina membranes filled with CsH_2PO_4. Fuel cells using such membranes were demonstrated at room temperature and OCV, current and power densities of of 0.9 V, 160 mA cm^{-2} and 27 mW cm^{-2} were achieved, respectively. The fuel cells however, were not stable under operation and OCVs with temperature, for example at 105°C the OCV was less than 0.5 V. Strontium zirconate has been used stabilizing oxide matrices in composites with CsH_2PO_4. [88] No chemical interaction was found between the components, however an increase in conductivity was observed explained by salt disordering due to interphase surface interaction. Addition of the zirconate was found to result in a gradual increase in conductivity in the low-temperature region by 1-3 orders of magnitude, while the high tem-

perature conductivity is close to that of the pure salt. Song-yul Oh *et al.* [89] improved the conductivity in the low temperature region of CsH_2PO_4 by fabricating composites with dodecaphosphotungstic acid ($H_3PW_{12}O_{40}\cdot nH_2O$). In their work, as well as in the work of others, an increase in the low temperature conductivity was observed. Highest conductivities were achieved as 6.58 x 10^{-4} S cm^{-1} at 170°C under anhydrous conditions.

Encouraging results have been reported, however fuel cells using such composites remain to be demonstrated at intermediate temperatures.

6.1.2 Experimental

In this work, composites of CsH_2PO_4 with TiO_2, ZrO_2 and SiO_2 were investigated.
CsH_2PO_4 was prepared as described in Subsection 5.1.1. ZrO_2, TiO_2 and SiO_2 (Aldrich, 99%) were used as received. Composites were prepared by thoroughly mixing the initial components in a ceramic mortar and pressed into pellets. The sample with a CsH_2PO_4 to ZrO_2 weight ratio of 2/1, as an example, is referred to as 2Cs/1Zr.
Physical characterizations including XRD, BET area, thermal analysis and SEM are performed as in Chapter 3. Electrochemical characterizations include OCV, fuel cell polarization and stability measurements were performed as described in Chapter 5. For conductivity measurements a heating rate of 1°C min^{-1} was used for the cell temperature control. The electrodes for fuel cell characterizations were prepared by spraying the catalyst layer onto a Toray or Ta GDL as in Chapter 5 to a total loading of 7 mg cm^{-2}. For fuel cell measurements, two types of MEAs were prepared resembling those of MEA **A** and MEA **C** (Chapter 5) *i.e.* Toray|Electrolyte|Toray and Toray|Electrolyte|Ta. MEA **C** was in this work prepared by dispersing the electrolyte layer onto the Ta cathode followed by subsequent pressing. In order to allow pressing ammonium acetate was added to the catalytic layer in equal mass. Following the pressing, the assembly was heat treated at 150°C for 3 hours to evaporate the ammonium acetate and create pores in the catalyst layer.

6.1.3 Results

OCV measurements using CsH_2PO_4/oxide composite electrolytes

In Table 6.1 the OCVs obtained using CsH_2PO_4/oxide composite electrolytes at 250°C are shown. Good OCVs (>0.9 V) were achieved for composites of CsH_2PO_4 with TiO_2 and ZrO_2, while very poor OCVs, below 0.3 V and unstable, were obtained with CsH_2PO_4/SiO_2 composites.

Table 6.1: *Maximum measured OCVs for composites at 250°C.*

Composite	OCV
2Cs/1Zr	0.99
2Cs/1Ti	0.95
Cs/Si	N/A

The properties of CsH_2PO_4 in composites with SiO_2 have been extensively studied. [38, 76, 85, 90] In this work, and in for example the work of Otomo *et al.* [90] the silica particles were used as received. The mechanical properties of the fabricated pellets were very poor (no quantitative proof for this was done), and in order to fabricate good fuel cells, this problem must be addressed.

As mechanical properties and OCVs of the CsH_2PO_4/ZrO_2 and CsH_2PO_4/TiO_2 were promising, these were further investigated.

CsH_2PO_4/ZrO_2 composites

Composites of CsH_2PO_4/ZrO_2 were made in compositions of 2/1, 6/1 and 20/1.

Figure 6.1 shows the XRD patterns of the CsH_2PO_4, ZrO_2 and $2CsH_2PO_4/1ZrO_2$ composite after heat treatment at 200°C for 16 h. Monoclinic ZrO_2 is indexed in the figure. All peaks in the composite correspond to those observed for CsH_2PO_4 and ZrO_2. Thus no other crystalline phases were detected. Based on the diffraction peaks of ZrO_2(-111) and ZrO_2(111) the average crystalline size of the oxide was calculated using the Scherrer equation and found to be around 110 nm.

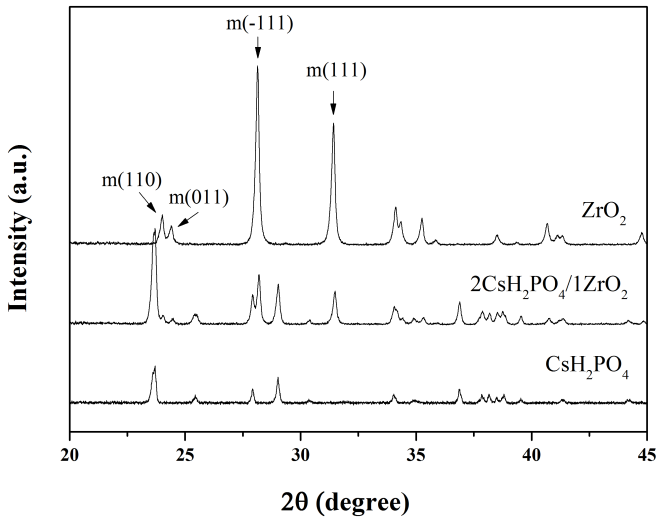

Figure 6.1: *XRD profiles of CsH_2PO_4, ZrO_2 and $2CsH_2PO_4/1ZrO_2$. Monoclinic ZrO_2 is indexed according to JCPDS card No. 371484.*

The results of thermogravimetric analysis (TGA) and differential thermal analysis (DTA) are shown in Figure 6.2. It should be mentioned that the measurements were made under dry argon atmosphere. To remove any adsorbed water the samples were preheated at temperatures up to 200°C. For the composites, the residual weight corresponded well with the formation of $CsPO_3$ from the CsH_2PO_4 phase assuming that the zirconia content remained unchanged. At temperatures above 230°C, dehydration of CsH_2PO_4 started with formation of pyrophosphate ($Cs_2H_2P_2O_7$) and further into $CsPO_3$, leading to a weight loss of 7.84%

which was reached at around 500°C. In the figure dotted lines are marking the weight losses which can be expected assuming that the zirconia content remains stable in the temperature range. These are in good agreement with the measured values, which were reached at higher temperatures, for example at around 600°C for the 2/1 sample. These results indicate the improvement of the thermal stability in terms of water retention for the composites.

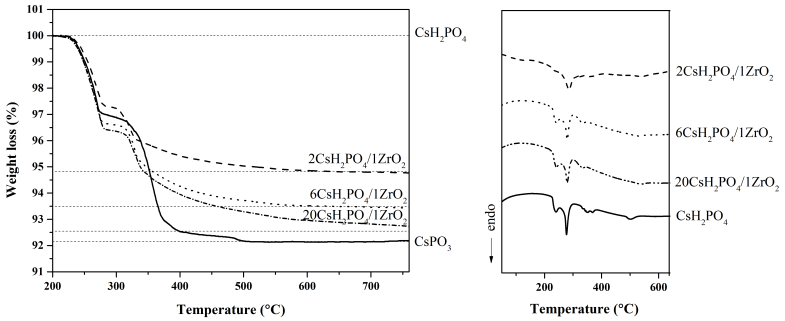

Figure 6.2: *DTA (left) and TGA (right) curves of CsH_2PO_4, $20CsH_2PO_4/1ZrO_2$, $6CsH_2PO_4/1ZrO_2$ and $2CsH_2PO_4/1ZrO_2$ composites recorded at 10°C min^{-1}.*

DTA curves of composites revealed similar events as for CsH_2PO_4, with decreasing intensity in the endothermic signal as the ZrO_2 content was increased. The endothermic effect at 234°C due to the superprotonic phase transition of CsH_2PO_4 was nearly invisible for the $2CsH_2PO_4/1ZrO_2$ sample. At around 274°C the intensity of the endothermic effect was also decreasing, however, to a less extent than that at 234°C. For the $2CsH_2PO_4/1ZrO_2$ sample, it was still evident. At the same time, a small shift was observed to slightly higher temperatures when additional amounts of ZrO_2 were present in the samples. For all samples, the endothermic peak at 345°C, corresponding to the melting point of CsH_2PO_4, was visible though somehow indistinct. As the content of ZrO_2 was increased, this peak became weaker and for the $2CsH_2PO_4/1ZrO_2$ composite it disappeared. In brief, the TGA and DTA study showed indications of the improved thermal stability of the composite materials.

Figure 6.3 shows the SEM images of ZrO_2 particles and a cross section of a $2CsH_2PO_4/1ZrO_2$ pellet composite. The oxide particles were in a range of 200-300 nm, thus somewhat higher than calculated from XRD. The BET area was measured as 5 m^2 g^{-1}, which is in good agreement with the specific surface area estimated from the SEM particle size. The pure CsH_2PO_4 phase (Chapter 5, Figure 5.4) appeared like a porous crystalline network, while the composite was characterized as flake-like crystalline clusters glued together. From this one may expect a coherent layer of the phosphate electrolytes from the oxide doped salt.

From the TGA and formerly reported literature, it can be expected that the water retention of the oxide composites are improved compared to the pure CsH_2PO_4. To investigate this the conductivity measurements were measured in humidified air with saturated water vapor

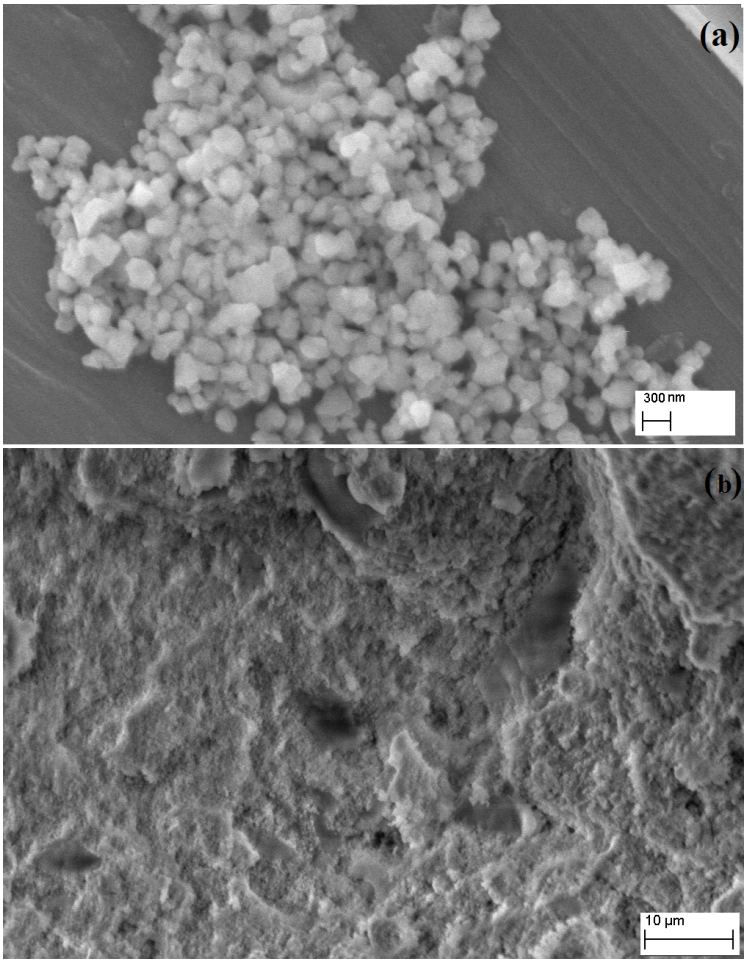

Figure 6.3: *SEM images of (a) ZrO_2; and (b) $2CsH_2PO_4/1ZrO_2$ composite.*

of 50°C, corresponding to a water partial pressure of only 0.12 atm compared to 0.3 atm which was used in Chapter 5. Figure 6.4 shows the measured conductivities of the prepared electrolytes. The conductivity of CsH_2PO_4 reached a maximum of 1.0 x 10^{-2} S cm^{-1} at 250°C. Above this temperature it dehydrated with a corresponding decrease in conductivity.

For the composite samples under the same hydration, the conductivity was found to be stable and steadily increasing with temperature to a higher range. For the $6CsH_2PO_4/1ZrO_2$ sample, a broad conductivity peak was observed at about 250°C, in a similar manner as that for the pure CsH_2PO_4. Above this temperature the conductivity was extended in increasing with temperature in the studied range of up to 285°C. For the $2CsH_2PO_4/1ZrO_2$ sample, the conductivity was found to monotonically increase with temperature in the studied temperature range. It is clear that the introduction of ZrO_2 in the phosphate effectively prevented the dehydration or/and the physical collapse of the phosphate electrolyte.

Similar results were reported for other types of composite materials. Baranov *et al.* [86] reported improved thermal stability of the phosphate composite with Al_2O_3, which extended the superprotonic conductivity to a higher temperature range than that of pure CsH_2PO_4.

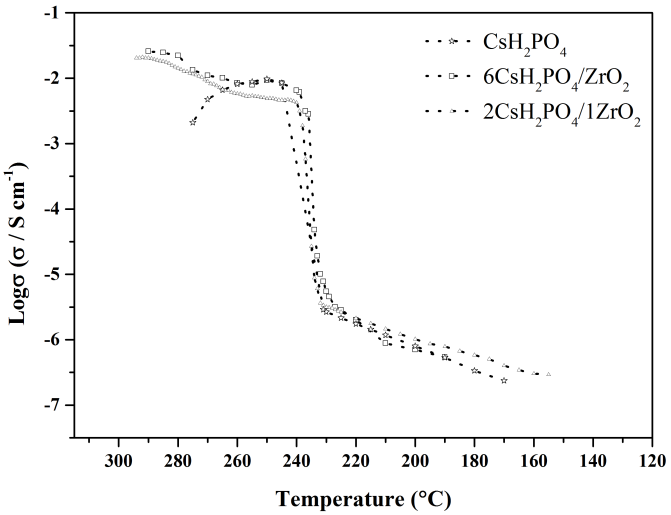

Figure 6.4: *Temperature dependence of conductivity of CsH_2PO_4, $6CsH_2PO_4/1ZrO_2$ and $2CsH_2PO_4/1ZrO_2$ samples. Air was saturated with water at 50°C.*

As discussed on the TGA and DTA measurements, the composites with ZrO_2 exhibited improved thermal stability in the high temperature range. This is in good agreement with the conductivity measurements. As shown in Figure 6.4, the superprotonic conductivity was preserved at temperatures as high as 285°C when ZrO_2 was present in the phosphate phase.

Fuel cells were evaluated under a small polarization. At a cell voltage of 0.8 V, the current densities as a function of time were recorded. By expressing the relative current density as a ratio of the measured current density to the initial maximum value, the result is shown in Figure 6.5a. A dramatic decrease in the current was observed for the pure solid acid electrolyte within the first 1000 seconds. For the electrolyte of the $6CsH_2PO_4/1ZrO_2$ composite, the stability was improved but a steady decrease was still observed after 2000 seconds. By using $2CsH_2PO_4/1ZrO_2$, a stable performance was observed, though the time scale of an hour was still very short. Bochetta *et al.* [87] showed the possibility of making thin composite electrolytes from CsH_2PO_4 with alumina as a mechanical support. Good short term performance was seen, however, the observed fuel cell performance decreased by more than 70% within the first hour.

Figure 6.5b shows the current density as function of time for the $2CsH_2PO_4/1ZrO_2$ electrolyte while keeping a fixed potential of 0.2 V. The fuel cell was running for 60 hours. It can be seen that there was an initial increase in performance followed by a nearly constant performance lasting for more than 60 hours, though with a certain variation.

Encouraged by the improved thermal stability of the composite electrolyte, an effort was

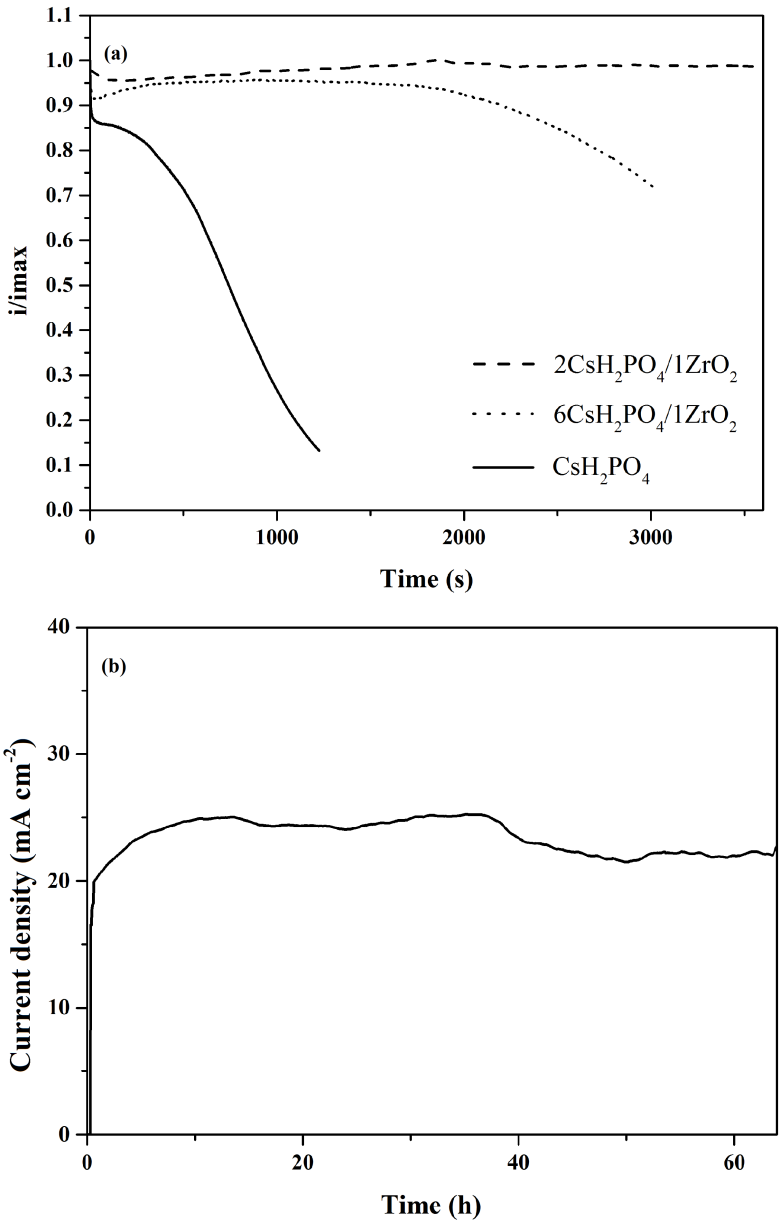

Figure 6.5: *Stability of the Toray|Electrolyte|Toray MEAs at 250°C with hydrogen and air saturated with water at 50°C. (a): The three cells and their operation expressed as ratio of the current density at 0.8 V to the maximum value. (b) Current density at voltage of 0.2 V for the $2CsH_2PO_4/1ZrO_2$ cell. Electrolyte thickness ca. 0.6 mm; Pt loading ca. 7 mg cm^{-2} for each electrode.*

made to fabricate a thin electrolyte layer (ca. 300 microns) by dispersing pure CsH_2PO_4 and composite powders onto the electrode surface *i.e.* MEA **C** (Toray|Electrolyte|Ta). As shown in Figure 6.6, the two composite cells showed OCVs above 0.9 V whereas the pure CsH_2PO_4 cell had an OCV lower than 0.8 V. The pure CsH_2PO_4 cell exhibited a maximum current density of 200 mA cm^{-2}, but the composite electrolyte cells showed lower currents. By elevating the cell temperature to 275°C, neither pure CsH_2PO_4 nor the

$6CsH_2PO4/1ZrO_2$ composite cell performed anymore, while the $2CsH_2PO_4/1ZrO_2$ composite cell gave an OCV above 0.9 V and a maximum current density above 200 mA cm^{-2} and power density higher than 40 mW cm^{-2}, as shown in the figure.

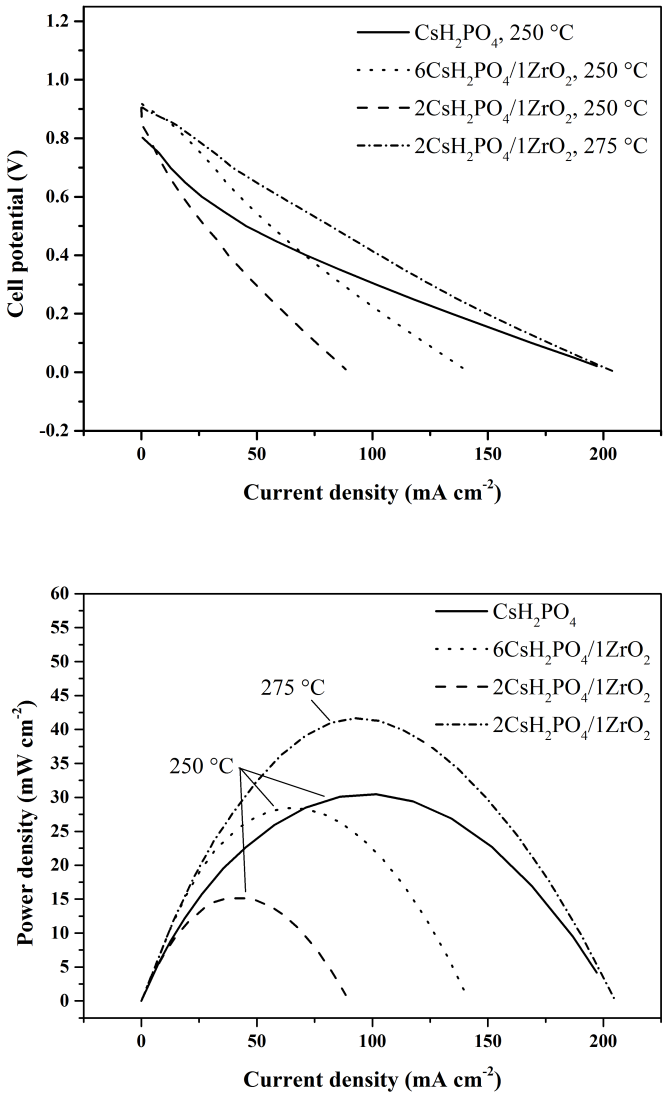

Figure 6.6: *Fuel cell polarization curves using Toray|Electrolyte|Ta with CsH_2PO_4, $6CsH_2PO_4/1ZrO_2$ and $2CsH_2PO_4/1ZrO_2$ electrolytes of about 300 micron thicknesses at 250 and 275°C. Hydrogen and air were saturated with water at 50°C. Electrolyte thickness ca. 0.3 mm; Pt loading ca. 7 mg cm^{-2} for each electrode.*

CsH_2PO_4/TiO_2 composites

Similar characterizations as for CsH_2PO_4/ZrO_2 were performed with TiO_2 as the additive (not shown). Fuel cell measurements performed with a Toray|$2CsH_2PO_4/1TiO_2$|Toray MEA are shown in Figure 6.7. High OCVs and good fuel cells performances were observed for

this type of electrolyte.

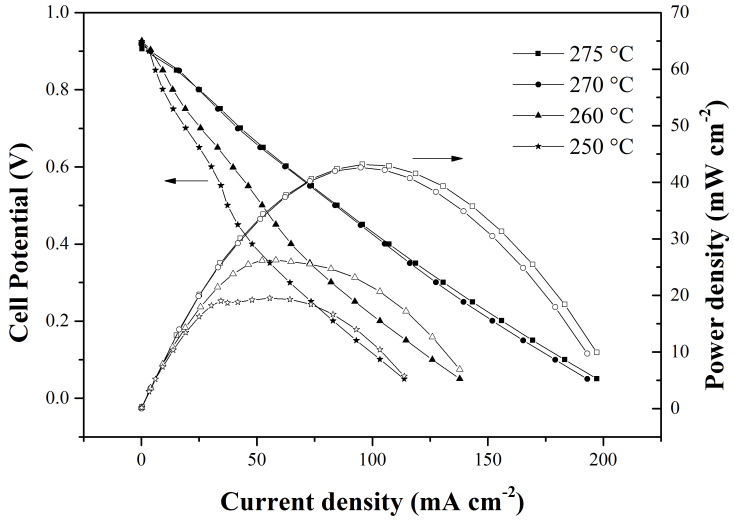

Figure 6.7: *Fuel cell polarization curve using and Toray|2CsH_2PO_4/1TiO_2|Toray MEA with electrolyte thickness of about 600 microns at 250 and 275°C. Hydrogen and air were saturated with water at 50°C. Pt loading ca. 7 mg* cm^{-2}

6.2 CsH_2PO_4/$NdPO_4$ composite electrolytes

In this section CsH_2PO_4 in composites with neodymium phosphate is investigated. The section is introduced by a short summery of the preparation and characterization of rare-earth-phosphates followed by the characterization of the prepared rare-earth-phosphates in composites with CsH_2PO_4.

6.2.1 Background and introduction

Rare earth phosphates are considered to be potential materials for applications in electrochemical cells for intermediate temperatures. Vast amount of research have been performed on the proton conducting rare-earth metal phosphates due to proton conductivity combined with thermal stability, however, no breakthroughs have been achieved in real fuel cell applications. The rare-earth phosphates are usually improved by substitution of divalent ions or used in composites where they are believed to improve the mechanical properties. [42, 43, 44, 45, 92]

First [91], three hydrated phosphates, $LaPO_4 \cdot 0.6H_2O$, $NdPO_4 \cdot 0.5H_2O$ and $GdPO_4 \cdot 0.5H_2O$, were synthesized and characterized. Water was found to be present in the systems in two ways *i.e* as surface adsorbed water and as hydrate water which was stable up to 650°C. Thermal stability of surface adsorbed and hydrate water was found to be of importance for the proton conductivity of the prepared phosphates. $NdPO_4 \cdot 0.5H_20$ was found to have

the highest conductivity from around above 200°C to 250°C, where the conductivity was measured as *ca.* 3 x 10^{-6} S cm^{-1}. The $NdPO_4 \cdot 0.5H_2O$ was chosen for further investigations in composite with CsH_2PO_4.

For the investigation of $CsH_2PO_4/NdPO_4 \cdot 0.5H_2O$ composites neodymium phosphate hydrate was prepared from Nd_2O_3 by wet precipitation using phosphoric acid at 150°C under constant stirring for 3 hours, and resultant powder was cooled down to room temperature and filtered. CsH_2PO_4 was prepared as described in Subsection 5.1.1. For synthesis of composites the initial powders were thoroughly mixed in a ceramic mortar, and composites of varying molar ratios (see Table 6.2) were investigated.

Table 6.2: *Molar compositions of prepared samples.*

Composition mol%
$100NdPO_4 \cdot 0.5H_2O$
$29NdPO_4 \cdot 0.5H_2O/71CsH_2PO_4$
$49NdPO_4 \cdot 0.5H_2O/51CsH_2PO_4$
$69NdPO_4 \cdot 0.5H_2O/31CsH_2PO_4$
$100Cs_2PO_4$

X-ray diffraction patterns were performed on the five samples, where the patterns of the composites comprised peaks of both initial compounds. No other peaks were detected. It is of interest to investigate whether a surface reaction takes place at the grain boundaries of the composites and therefore diffraction patterns were made of the sample of $29NdPO_4/71CsH_2PO_4$ before and after heat treatment for 24 hours at 250°C in humidified air (p_{H_2O}=0.15 atm). The $29NdPO_4/71CsH_2PO_4$ showed clear peaks of both initial components both before and after the heat treatment, and additionally after the heat treatment small signals appeared probably owing to the formation of $CsH_5(PO_4)_2$. The conductivities of all five samples were measured as function of temperature. The conductivities of composites below the transition temperature were at all times orders of magnitudes higher than the those of the pure phosphates. For example at 150°C the conductivity was found to be 0.4 x 10^{-2} S cm^{-1} for the $29NdPO_4 \cdot 0.5H_2O/71CsH_2PO_4$ composite while it was found to be around 10^{-6} and 10^{-4} S cm^{-1} for CsH_2PO_4 and $NdPO_4$, respectively.
These results encouraged demonstration of such composites in electrochemical cells, and in the following such results are presented.

6.2.2 Experimental

Electrochemical investigations of prepared $29NdPO_4 \cdot 0.5H_2O/71CsH_2PO_4$ composites included OCV measurements, measurements in a hydrogen concentration cell and fuel cell measurements. MEAs were made from pressed pellets of the electrolytes two similar electrodes *i.e.* MEA **A** (Chapter 5), with electrodes made from a mixture of Pt/C, Pt black and CsH_2PO_4 sprayed on Toray GDLs to a platinum loading of 7 mg cm^{-2} was used.

Measurements were performed in a hydrogen concentration cell at various temperatures using a Toray|29NdPO$_4$/71CsH$_2$PO$_4$|Toray MEA and by leading hydrogen to one electrode and a mixture of hydrogen and nitrogen to another as in Equation 6.1.

$$H_2(1atm), Pt|29NdP/71CsH_2PO_4|Pt, H_2(0.1atm) \tag{6.1}$$

For OCV measurements Toray|29NdPO$_4$/71CsH$_2$PO$_4$|Toray MEAs were used in humidified hydrogen and air at various temperatures.

6.2.3 Results and discussion

Figure 6.8 shows the measured EMF compared to values calculated from Nernst equation for a Toray|29NdPO$_4$/71CsH$_2$PO$_4$|Toray MEA. EMF measurements were performed in a cell with different hydrogen partial pressures on each side as shown in Equation 6.1 at temperatures from 150 to 235°C, and the measured EMF values were found to be in good agreement with calculated values. This suggests that the conductivity is primarily protonic under these conditions.

Figure 6.9 shows an example of a long term OCV measurement measured at 235°C. The OCVs measured with such MEAs were high and stable, in this case the measured open circuit voltage was 0.93 V at start and increased steadily to 0.97 V after 12 hours. The deviation from theoretical open circuit potentials (1.13 at 235°C) was discussed in Chapter 5, and is in this case expected to be mainly due to the irreversibility of the oxygen electrode. Agreement between calculated and measured EMF values, as well as the high OCVs measured indicate dense structures of the fabricated pellets. It was indeed observed that the fabricated pellets were mechanically strong, though no quantitative evidence for this is given.

Fuel cell performances using Toray|29NdPO$_4$/71CsH$_2$PO$_4$|Toray MEAs were measured at various temperatures for are shown in Figure 6.10. As could be expected, the current and power densities increase with increasing temperatures. All polarization curves shows ohmic characteristics, due to the thickness of the electrolyte (700 μm), and therefore the performance is expected to increase considerably if a thinner electrolyte is used. Maximum power and current densities were measured at 285°C as 27.7 mW cm^{-2} and 117 mA cm^{-2}, respectively.

Based on the ohmic characteristics of the fuel cell, the conductivities of the electrolyte were calculated from the slope. The results are listed in Table 6.3 and appears to be in good agreement with conductivity values measured by impedance, thus confirming the ohmic resistance dominating the fuel cell performance.

This demonstration confirms the proton conducting nature of the composite. It can be speculated what causes the increase in conductivity by several orders of magnitude. As was introduced, an increase in conductivity in composites can have several origins. As mentioned, from XRD it was found that a new phase, $CsH_5(PO_4)_2$, was detected. This phase

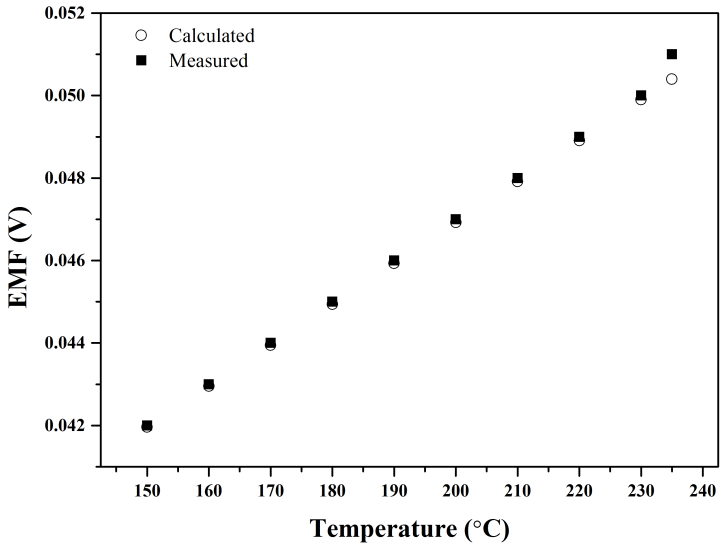

Figure 6.8: *EMF values as function of temperature of a hydrogen concentration cell, H_2(1 atm)|29$NdPO_4$/71CsH_2PO_4|H_2(0.1 atm). Electrolyte thickness=0.7 mm; Pt loading=7 mg cm^{-2}.*

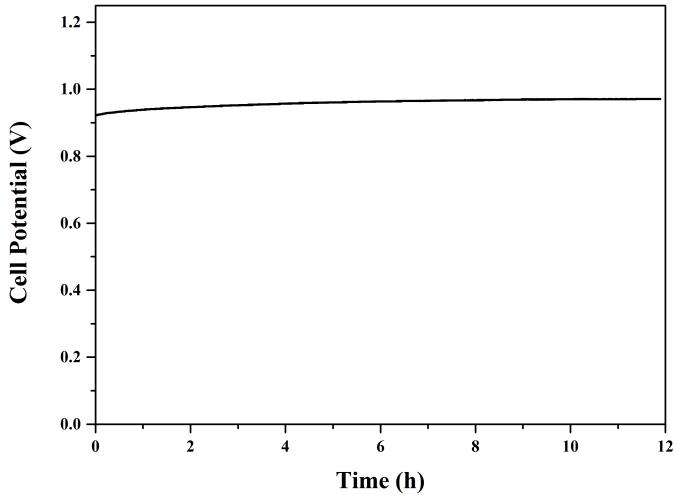

Figure 6.9: *Open circuit voltage for Toray|29$NdPO_4$/71CsH_2PO_4|Toray in humidified hydrogen and air at 235°C. pH_2O=0.3 atm. Electrolyte thickness ca. 0.7 mm; Pt loading=7 mg cm^{-2}.*

has a lower melting point (150°C) than $NdPO_4$ and CsH_2PO_4, and leads to a high surface conductivity in a liquid layer at the grain boundaries as was also seen in [34]. Another explanation for the conductivity increase can be surface adsorbed water. As introduced, water is contained in rare earth phosphates in two ways, as surface adsorbed or as crystal hydrate water which is stable at temperatures up to 650°C and thus the temperature is of

Table 6.3: *Conductivities calculated based on fuel cell slopes.*

Temperature (°C)	**Conductivity (S cm^{-1})**
233	0.36 x 10^{-2}
250	0.48 x 10^{-2}
270	0.72 x 10^{-2}
285	0.92 x 10^{-2}

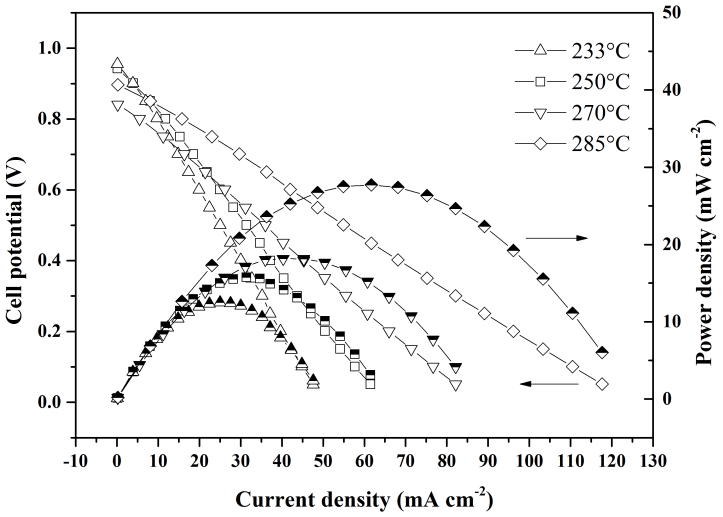

Figure 6.10: *I-V and I-P characteristics of a Toray|29$NdPO_4$/71CsH_2PO_4|Toray in humidified hydrogen and air at various temperatures. Hydrogen and air were saturated with water at 70°C. Electrolyte thickness= 0.7 mm; Pt loading=7 mg cm^{-2}.*

significance for the conductivity. Additionally, the acidity is believed to have an influence on the conductivity. If two components of different acidities are combined, a hydrogen bond network may be established between the two components. Oh *et al.* [89] formed composites of CsH_2PO_4 and phosphotungstic acid ($H_3PW_{12}O_{40}\cdot nH_2O$) and suggested that the increase in conductivity was not only due to the wetting of CsH_2PO_4 by hydrate water, but also due to newly formed hydrogen bonds between the two components. It is likely that such interactions also takes place in the $CsH_2PO_4/NdPO_4\cdot nH_2O$ composites though no evidence for this was observed.

6.3 CsH_2PO_4/Melamine cyanurate composite electrolytes

6.3.1 Background and introduction

Addition of organic compounds to solid acids for formation of inorganic-organic electrolyte complexes have two purposes. First, the conductivity may be improved by acid-base interaction in the membranes, a mechanism also known from PEM fuel cells, where polymers

bearing basic sites react with strong acids such as phosphoric acid. The basicity of the polymers enables an establishment of hydrogen bonds with the acid. [93] Second, polymers in composites may enable the formation of thin and flexible films. [94]

Few attempts have recently, in 2012, been made in order to establish acid-base interactions in inorganic-organic composites. Matsuda *et al.* [95, 96] prepared composites of solid acids with Guanine and its tautomers as well as azoles (Imidazole, 1,2,4-triazole and Benzimidazole). The composites showed significantly higher proton conductivities than the components alone. For example $CsHSO_4$ was mechanochemically mixed with Imidazole, 1,2,4-triazole and benzimidazole in composites of $80CsHSO_4$/20Azole (mol%). [96] They observed an increase in conductivity, particularly in the low temperature region below the superprotonic phase transition of $CsHSO_4$. *E.g.* proton conductivities of $80CsHSO_4$/20Imidazole ranged from 6.8 x 10^{-4} to 1.7 x 10^{-3} S cm^{-1} over a temperature range from 60-160°C. Same authors [95] mechanochemically mixed CsH_2PO_4 with guanine in molar ratios from 50 to 90 mol% CsH_2PO_4. Proton conductivities of all the composites were found to increase by more than two orders of magnitude than the pure CsH_2PO_4. Though good conducting properties were observed for both systems, no fuel cell demonstrations were performed.
Very recently, 2014, Kikuchi *et al.* [94] used a polymer, polyvinylidene fluoride (PVDF), in a composite with CsH_2PO_4 in order to prepare thin electrolyte films for fuel cells. The thin film electrolyte was prepared by slurry casting from a ball milled suspension containing CsH_2PO_4, PVDF and dimethylformamide. In this way, they fabricated membranes with thicknesses of 101 and 67 μm. Using this membrane they demonstrated a fuel cell with an OCV of 0.92 V and a peak power density of 86 mW cm^{-2} at 259°C in humidified hydrogen and oxygen (pH_2O=0.3 atm).

In this work melamine cyanurate is used in inorganic-organic complexes with CsH_2PO_4. The chemical structure of melamine cynanurate complex is shown in Figure 6.11.

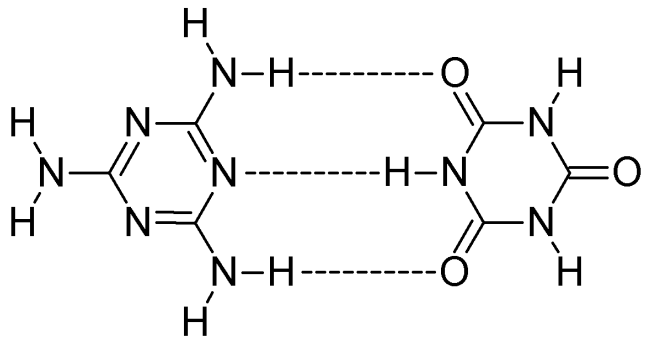

Figure 6.11: *Melamine-cyanurate complex*

6.3.2 Experimental

Composites of CsH_2PO_4 and melamine cyanurate (Aldrich, >99%) were synthesized by solid state ball milling. CsH_2PO_4 was prepared as described in Subsection 5.1.1. The mechanochemical treatment was carried out using a ball mill with an agate pot (Fritsch, 45 mL) and 10 agate balls (10 mm i diameter). The rotation speed was maintained at 700 rpm for 1 hour.

Resultant powders were characterized by SEM, TGA and conductivity measurements as described in Chapter 5 Conductivity measurements were performed at various temperatures, before each measurement the temperature was stabilized for 30 minutes.

A preliminary screening was performed with several organic components (not shown). From these experiments it appeared that the highest conductivities were achieved from the composite of CsH_2PO_4 and melamine cyanurate, and thus further experiments were performed with these initial components. Samples were made with various compositions according to Table 6.4.

Table 6.4: *Molar compositions of prepared samples.*

Composition mol%
100Melamine cyanurate
95CsH_2PO_4/5Melamine cyanurate
90CsH_2PO_4/10Melamine cyanurate
80CsH_2PO_4/20Melamine cyanurate
100Cs_2PO_4

6.3.3 Results and discussion

Physical characterizations

Thermal properties of CsH_2PO_4, melamine cyanurate and the composites were evaluated using powder samples in air (Figure 6.12a). The TGA of $CsH_2PO_4$was evaluated in an earlier Chapter (Chapter 5). In short CsH_2PO_4 dehydrates at around 230°C under anhydrous conditions. Pure melamine cynanurate showed one considerable weight loss around 320°C which is attributed to the thermal decomposition. In comparison, CsH_2PO_4/Melamine cyanurate complexes showed lower thermal decomposition temperatures than the pure starting compounds.

Figure 6.13 shows SEM images of melamine cyanurate (MeCy) and 90CsH_2PO_4/10MeCy ball milled powders. The pure melamine cyanurate powders appears more dispersed than the agglomerated composites.

Electrochemical characterizations

Figure 6.14 shows the conductivities of the prepared electrolytes at various temperatures measured after 30 min temperature stabilization before each measurement. The conductivities for the composites are higher than the pure CsH_2PO_4 at all temperatures. Below the

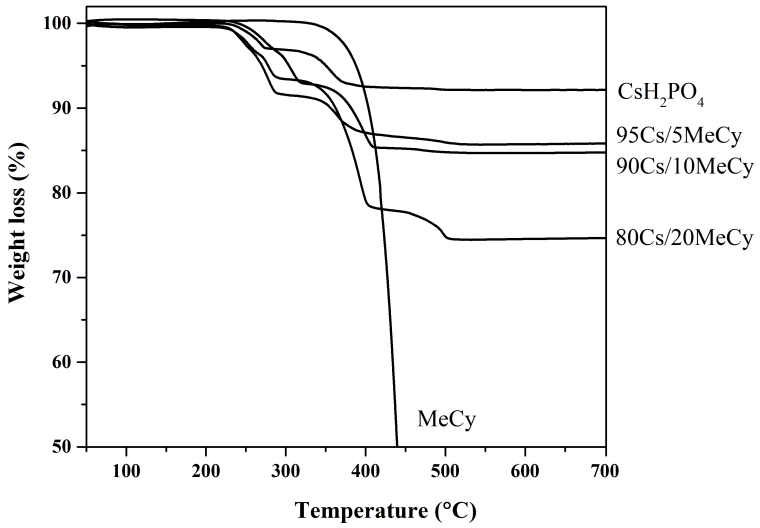

Figure 6.12: *TGA profile of CsH_2PO_4 (Cs), melamine cyanurate complex (MeCy) and composites produced by mechanochemical treatment.*

phase transition temperature all composites showed conductivities of more than one order of magnitude higher than the pure CsH_2PO_4. Figure 6.14 (right) shows the conductivities as function of the CsH_2PO_4 content at 120, 140 and 250°C. Moreover, the conductivity appeared to increase with increasing melamine cyanurate content (up to 10%). For this composition the conductivity at 250°C was as high as 0.18 S cm^{-1}. Unfortunately it was not possible to fabricate a coherent pellet with higher amount of melamine cyanurate. It was also attempted to measure the conductivity of the pure melamine cyanurate, however this could not be measured.

6.4 Summary

This chapter presented the development of CsH_2PO_4 elctrolyte by composite formation with oxides *i.e.* SiO_2, TiO_2 and ZrO_2, a rare-earth phosphate *i.e.* $NdPO_4{\cdot}0.5H_2O$ and an organic compound *i.e.* melamine cyanurate.

Composite electrolytes based on CsH_2PO_4 and ZrO_2 were prepared and their properties were investigated within the intermediate temperature range. Thermogravimetric analysis showed significant improvement in the thermal stability of the composites. Under low hydration (pH_2O=0.12 atm), the conductivity of pure CsH_2PO_4 dropped at above 250°C while that of the composites increased monotonically with temperature up to 280°C. In addition, better densification was observed for the pellet electrolytes of the composites, which was confirmed by the enhanced open circuit voltage of fuel cells in the entire studied temperature range from 120 to 275°C. Fuel cells were operated at temperatures up to 275°C thus

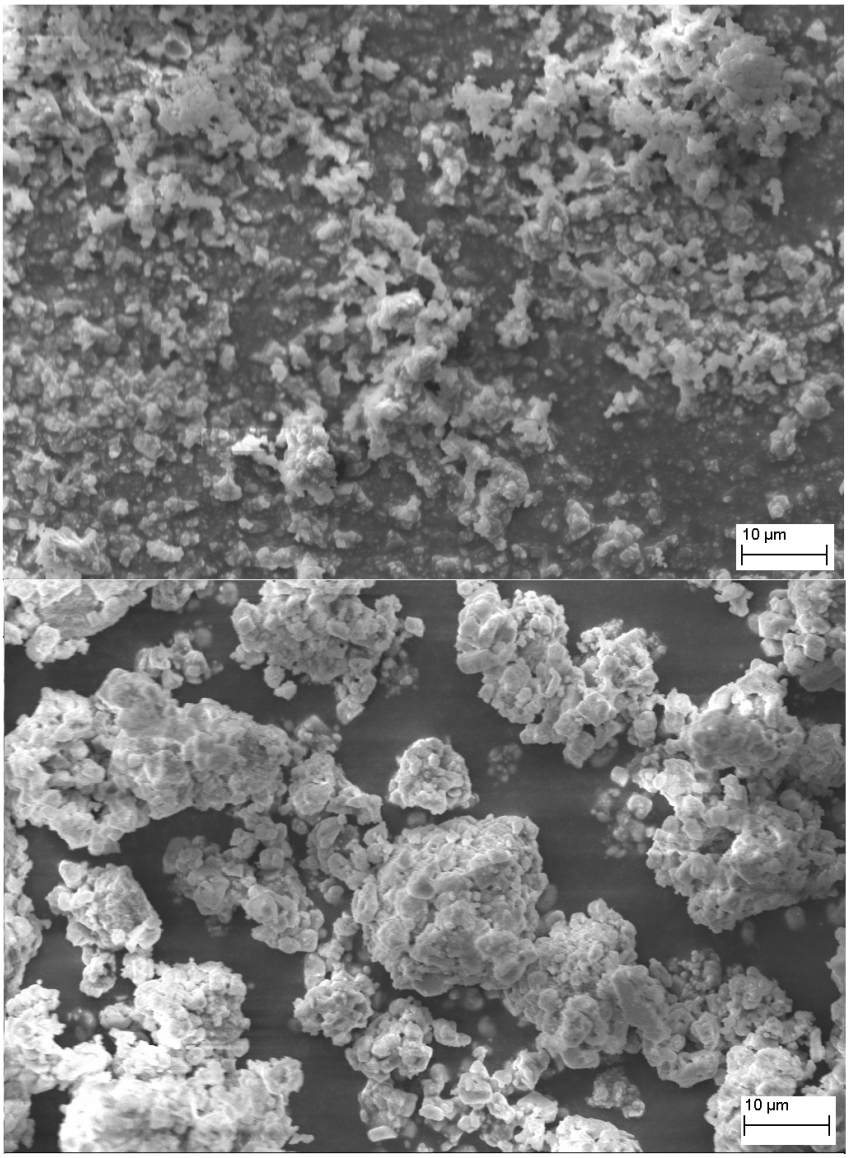

Figure 6.13: *SEM images of top: Melamine Cyanurate, and bottom: Ball milled 90CsH_2PO_4/10MeCy.*

demonstrating the improved mechanical and thermal stability, when using the composite electrolyte with a CsH_2PO_4 to ZrO_2 molar ratio of 2. The best fuel cell performance was achieved at 275°C and exhibited an OCV above 0.9 V and a maximum current density above 200 mA cm^{-2} and a power density of more than 40 mW cm^{-2}.

Composites of CsH_2PO_4 an $NdPO_4 \cdot 0.5H_2O$ were prepared in various concentrations. XRD of such composites after heat treatment at 250°C showed the two initial compounds as well as a formation of a new phase, $CsH_5(PO_4)_2$. Conductivity measurements were performed showing an increase by several orders of magnitudes, in the low temperature regime. It is likely that more than one mechanism contributed to the drastic increase in conductivity and the main reason for this increase was not fully clarified. $CsH_5(PO_4)_2$, a new phase formed

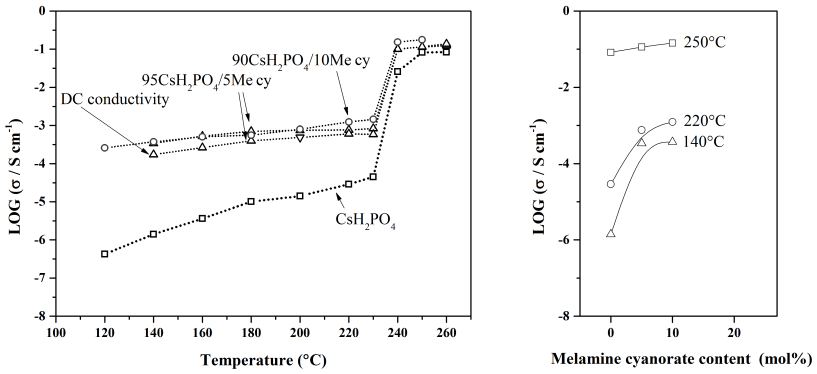

Figure 6.14: *Left: Temperature dependence of conductivity CsH_2PO_4, $95CsH_2PO_4$/5Melamine cynanurate and $90CsH_2PO_4$/10Melamine cynanurate samples. Thermal stabilization of 30 min. before each measurement. pH_2O=0.3 atm. Right: Conductivity of CsH_2PO_4/Melamine cyanurate complexes of different compositions at 120, 140 and 250°C.*

as a liquid layer at the interphases, might be responsible for an increase. Another probable mechanism is from the establishment of a hydrogen bond network occurring due to the difference in surface acidities between the two components. It is likely that both mechanisms are contributing, more considerations on this question were however not done.
Neodymium phosphate/cesium dihydrogen phosphate electrolytes were found to be mechanically strong, and experimental values from a hydrogen concentration cell were in very good agreement with calculated values. Moreover the measured OCVs were high and stable throughout the experiments *e.g.* 12 hours. Operating fuel cells at different temperatures were demonstrated suggesting ohmic resistance probably due to the thick electrolyte. Accordingly, fuel cells can be improved by using electrolytes of lower thickness.

Solid-state ball milling was used to synthesize inorganic-organic composite electrolytes from CsH_2PO_4 and melamine cyanurate. The composite formation resulted in conductivities higher than the pure CsH_2PO_4 over the entire temperature range probably owing to the establishment of a hydrogen bond network.

In summary, the literature study (Chapter 2) combined with the experimental chapter (Chapter 5) suggested that in order to achieve stable high performance CsH_2PO_4-based fuel cells, the CsH_2PO_4 must be used in a composite with at least one additional component.
In this chapter CsH_2PO_4 was prepared in composites with three different classes of additives; oxides, a rare-earth phosphate and organic compounds. The conductivity was improved by physical stabilization, formation of a new highly conducting amorphous surface layer or by chemical interaction *via* hydrogen bonds. System improvements were achieved as mechanical improvement of the electrolyte, extension of the superprotonic phase, increased stability, and hindrance of dehydration enabling operation at lower water partial

pressures.

Chapter 7

Niobium and Bismuth Phosphates as Novel Electrolytes

Part of the PROCON project, included a search for novel materials for electrolytes in fuel cells at intermediate temperatures. This chapter summarizes the key results from a joint research performed within the PROCON project, with results published in [57, 97] and [98], and elaborates on cell assembling.

7.1 Background and introduction

In this chapter new proton conductors based on niobium and bismuth phosphates were synthesized using pentoxides and phosphoric acid as precursors. The resulting phosphates were evaluated as potential electrolytes for intermediate temperature electrochemical cells.

Preliminary experiments included a screening of several new potential proton conducting electrolytes. A series of metal phosphates was synthesized by mixing corresponding oxides with aqueous H_3PO_4 solution in a temperature range from 150 to 300°C. [57] Among the investigated phosphates, niobium and bismuth phosphates (the niobium phosphate was found to be a mixture of orthorhombic $Nb_{1.91}P_{2.82}O_{12}$ and monoclinic $Nb_5P_7O_{30}$, and bismuth phosphate was found to be a mixture of monoclinic $Bi_2P_4O_{13}$ and $BiPO_4$) were found to be the most promising, as they exhibited highest conductivities at 250°C. [57] For the bismuth phosphate, conductivities were found to be strongly dependent on the water partial pressure, a conductivity of 2 x 10^{-7} S cm^{-1} was measured at 250°C under anhydrous conditions, and increased to a high level, 3 x 10^{-2} S cm^{-1} with a water content above 0.6 atm, at the same temperature. [57] It was particularly interesting that the conductivity of niobium phosphate reached a value as high as 2.8 x 10^{-2} S cm^{-1} at 250°C under unhumidified conditions. Stability tests were performed for the preliminary niobium and bismuth phosphates showing reasonably stable conductivity at 250°C within a period of more than 80 hours. [57]

Good conductivity values, especially for niobium phosphate encouraged further studies of such phosphates. Earlier literature studies [99, 100] demonstrated the possibility of stabilizing surface functionalities at high temperatures by phosphoric acid treatment. For example Okazaki *et al.* [100] stabilized functionalities up to nearly 600°C. This combined with ease

of water adsorption makes niobium phosphate a good candidate for intermediate temperatures. Very few investigations have been made on the preparation of niobium phosphates as a proton conductor. Cantero *et al.* [101] prepared acidic niobium phosphates, in the form of $NbOPO_4 \cdot nH_2O$ (n<3), and measured proton conductivities over a relatively low temperature range from 27 to 140°C. The conductivity was found to increase with temperature until 100°C, where a maximum conductivity of 5 x 10^{-6} S cm^{-1} was measured. Higher conductivities of niobium phosphates were measured by Chai *et al.* [102], about 1.7 x 10^{-2} S cm^{-1} at room temperature under a relative humidity of 100%.

As was discussed in Section 2.2 for SnP_2O_7-based electrolytes, surface functionalities *e.g.* from excess phosphoric acid are believed to be the main contributor to the high conductivity values although not fully clarified. Thus, naturally, synthesis history, such as molar ratio of P/Metal and heat-treatment has a large influence on the resulting properties. In our work [97], it was decided to prepare the niobium phosphates from Nb_2O_5 and H_3PO_4 with an initial molar ratio of P/Nb 2.5:1, at 200-300°C. Resulting pastes were heat-treated at four different temperatures (350, 500, 650 and 800°C) for 3 hours followed by materials characterization and conductivity measurements.
XRD profiles of the niobium phosphates sintered at the four different temperatures were presented together with crystal patterns of orthorhombic $Nb_{1.91}P_{2.82}O_{12}$, cubic $Nb_2P_4O_{15}$ and monoclinic $Nb_5P_7O_{30}$. It appears that niobium phosphates heat-treated at low temperatures (350 and 500°C) had mixed orthorhombic and monoclinic phases, while niobium phosphates heat-treated at higher temperatures (650 and 800°C) had mixed monoclinic and cubic phases.

Conductivities of the niobium phosphates were performed during heating and cooling between 70 and 250°C under anhydrous conditions. For the niobium phosphate treated at 350°C (NbP350) the conductivity increased with temperature up to 160°C where it was measured as 2.4 x 10^{-2} S cm^{-1}. Above 160°C the conductivity decreased drastically. The niobium phosphates heat-treated at 500, 650 and 800°C (*i.e.* NbP350, NbP500, NbP650 abd NbP800, respectively) were found to have increasing conductivities with increasing temperature in the entire temperature interval *i.e.* up to 250°C. From the three samples, the highest conductivity was measured for NbP500C as 1.6 x 10^{-2} S cm^{-1} at 250°C. Moreover conductivity stability measurements were performed for the NbP500 and NbP650 at 250°C showing reasonable stability for 50 h. [97]

As shortly mentioned in the literature study (Chapter 2) pyrophosphates have shown to improve conductivity by doping with trivalent metal ions such as Al^{3+}, In^{3+} or Sb^{3+}. Hibino *et al.* [103, 104] investigated a series of pyrophosphates with equimolar ratios of a trivalent (A^{III}) metal and a pentavalent (B^{V}) metal. They achieved an anhydrous proton conductivity as high as 0.18 S cm^{-1} for a $Fe_{0.4}Ta_{0.5}P_2O_7$ electrolyte at 250°C. When introducing a deficiency the proton conductivity was enhanced and the $Fe_{0.4}Ta_{0.5}P_2O_7$ electrolyte exhibited

a conductivity as high as 0.25 S cm^{-1}. In work performed in our group [98], indium doped niobium phosphates were prepared form precursors of trivalent indium oxide, pentavalent niobium oxide and phosphoric acid. The obtained materials were characterized by XRD, impedance spectroscopy, FT-IR spectroscopy and SEM. It was found that the indium doping promoted the formation of the high conducting $Nb_2P_4O_{15}$ instead of the $Nb_5P_7O_{30}$ in the pristine niobium phosphates and enhanced the preservation of OH functional groups in the phosphates. The preserved OH functionalities in the phosphates after the heat treatment at 650°C contributed to the anhydrous conductivity. The indium doped niobium phosphate exhibited a proton conductivity five times higher than that of the un-doped analog at 250°C. The conductivity was stabilized above 0.02 S cm^{-1} under dry atmosphere at 250°C during the stability evaluation for three days.

In the following, bismuth phosphates, niobium phosphates and indium doped niobium phosphates are evaluated for their potential use as electrolytes for intermediate temperature electrochemical cells.

7.2 Experimental

MEAs For electrochemical measurements electrolytes were made as MEA **A** in Chapter 5 two identical electrodes (Carbon, Pt loading=0.7 mg cm^{-2}) and electrolytes around 1.5 mm thicknesses. NbP500 (NbP in the following), indium doped niobium phosphate (NbInP) and bismuth phosphate (BiP) were used as electrolytes. The mechanical nature of the prepared phosphate electrolytes hindered the use of pure phosphates in the cell measurements and thus PBI was added for strengthening. Composite pellets were pressed into pellets under a pressure of 5 x 10^3 kg cm^{-2}. OCV and hydrogen concentration cell measurements were performed as described earlier (Section 3.2).

7.3 Results

Table 7.1 shows the highest measured OCVs for the phosphate/PBI composites. For NbP(5 wt% PBI) the OCVs dropped significantly with incresing temperature. At 200°C the best measured OCV was 0.75 V. To improve the mechanical integrity of the phosphate a high amount (20%) of PBI was added to the phosphate and the OCV thereby improved. As shown in table 7.1, an OCV as high as 1.045 V was measured at 70°C. At higher temperatures, 110 and 200°C, stable OCVs were measured as 0.895 and 0.863 V.

For the $Nb_{0.9}In_{0.1}P$(5% PBI) electrolyte, the mechanical properties were very poor. It was attempted to fabricate a coherent pellet, however with this electrolyte no stable OCVs could be achieved. Maximum OCVs of 0.9 V at 25°C and 0.7 V at 200°C were achieved. For BiP, the OCVs were stable; for BiP(5% PBI) 0.8 V was measured at 200°C and maintained at 230°C. The maximum OCVs are summerised in Table 7.1.

Table 7.1: *Maximum measured OCVs for niobium-, niobium-indium- and bismuth-phosphate-based electrolytes reinforced with PBI.*

Electrolyte	**Temperature** (°C)	**Maximum OCV (V)**
NbP(5% PBI)	110	0.92
	150	0.84
	200	0.75
NbP(20% PBI)	70	1.045
	110	0.895
	200	0.86
NbInP(5% PBI)	25	0.9
	200	0.7
BiP(5% PBI)	200	0.8
	230	0.8

Figure 7.1a shows long term OCV measurements for a NbP(20% PBI) electrolyte at 70, 110 and 200°C. At all three temperatures the OCVs were stable over the measuring time of around 10 hours. Long term OCV measurements were also performed for BiP(5% PBI) at 200 and 230°C (Figure 7.1b). The OCVs remained stable and even slightly increasing for a time period of around 80 hours at 230°C.

Measured and calculated potentials for NbP and BiP are shown in Figure 7.2 as function of temperature in hydrogen concentration cells according to Equation 7.1.

$$H_2(1atm), Pt|Electrolyte|Pt, H_2(0.05atm) \tag{7.1}$$

Measured potentials for NbP are in excellent agreement with the theoretical values calculated from the Nernst equation. This indicates the protonic nature of the ionic conductivity of NbP. For BiP there is a larger deviation from the theoretical values, and the deviation is furthermore irregular.

7.4 Discussion

A screening of metal phosphates lead to encouraging results in terms of conductivity values and stability. It was attempted to fabricate electrochemical cells using such electrolytes. It was not found possible to achieve high and stable OCVs for the phosphates alone, and therefore it was attempted to stabilize the phosphates with a polymer, PBI. As discussed in Chapter 5 that several factors influences the open circuit voltage. It is for example critical that the electrolytes are dense to avoid leakage of gases. As was shortly mentioned in the literature study (Chapter 2) polymers are a promising matrix materials to prepare flexible and thin composite electrolytes as they add strength and enables fabrication of thin electrolytes. In this work, good OCVs could not be achieved by use of the pure phosphates and therefore PBI was added though it was expected to decrease conductivity. [28] The OCV was found to increase with the addition of PBI, and finally a high amount, 20 wt% was used.

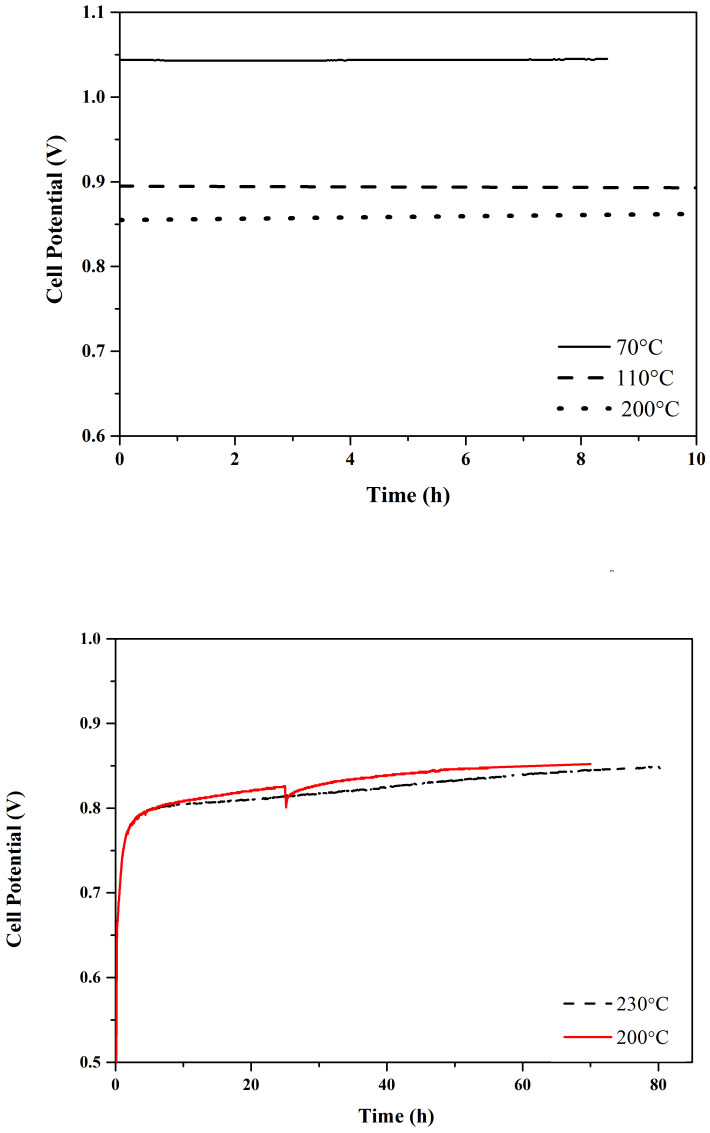

Figure 7.1: *OCV-measurements at various temperatures using H_2,Carbon\Electrolyte\Carbon,air (Pt loading=0.7 mg cm^{-2}, electrolyte thicknesses≈1.5 mm) MEAs vs time using with A: a NbP(20% PBI) electrolyte and B: BiP(5% PBI) electrolyte.*

Using the phosphate-PBI composites, stable OCVs could be achieved at low temperatures, however at higher temperatures the OCVs increased, for example at 200°C the OCV was measured as 0.86 V (with 20% PBI). As was also discussed for $Sn_{0.9}In_{0.1}P_2O_7$ electrolytes [105], it is possible that the lowered OCV can be attributed to a mixed proton and electron-hole conduction. In our case, as well as in their work, proton conduction were observed under reducing atmospheres. In [105], however the electrolyte showed mixed conduction

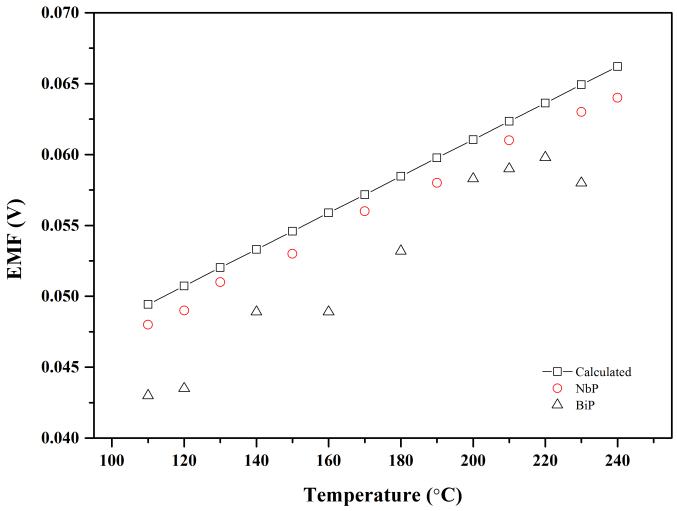

Figure 7.2: *EMF values for H_2 (1atm), Carbon\Electrolyte\Carbon, H_2 (0.05 atm) cells with niobium and bismuth phosphates as electrolytes. Pt loading=0.7 mg cm^{-2}.*

in oxidizing atmospheres. For good OCV measurements, the electrode composition should furthermore be addressed. The electrodes used had a low platinum loading and the contact with the electrolyte was not optimized.

For improvements of the electrochemical cells using niobium phosphate electrolytes, vast amount of research is yet to be done. First, the synthesis must be optimized, in this work only one parameter was varied. The effect of synthesis parameters must be thoroughly investigated. Second, fabrication of dense stable electrolytes is necessary for stable good fuel cell results. In this work a high amount of PBI ensured stability in the OCV measurements. It is possible that other compounds can have a beneficial effect on the electrolyte density. Polymers have shown to be promising materials for preparation of thin and flexible composite electrolytes. [28, 40, 41, 106, 107] Hibino and coworkers used polystyrene-b-poly(ethylene/butylene)-b-polystyrene and sulfonated polystyrene-b-poly(ethylene/butylene)-b-polystyrene as support for $Sn_{0.95}Al_{0.05}P_2O_7$ to prepare thin electrolytes. [40, 41] In this way, as mentioned in the literature review they achieved thin layers of less than 100 μm. Third, the electrodes used in this work consisted of an electrocatalytic layer of PBI and Pt/C on carbon cloth with a loading of 0.7 mg cm^{-2}. As addressed in earlier chapters, for effectively working cells, the fabrications of active and stable electrodes is critical as well as the contact between the electrodes and the electrolyte layer.

Chapter 8

Tungsten Carbide as Non-Noble Catalyst

8.1 Background and introduction

Owing to the high cost of precious metals commonly used as catalysts in electrochemical cells many studies have been conducted to develop new materials or to reduce the loading. [108] Several transition metal based materials, especially carbides, have been shown to have promising properties for applications in fuel cells and electrolyzers. Transition metal carbides are the most widely studied among the non-noble metal catalysts for hydrogen evolution and oxidation, and studies indicate the possibility of high catalytic activity for molybdenum, chromium, titanium and tungsten carbides. These are characterized by having superior properties such as high melting points, hardness, high oxidation resistance and electrical conductivity. Tungsten carbide is the hardest (16-22 GPa, 500 g load Vickers test) of the binary carbides, it is resistant to oxidation and corrosion and has a high melting point (2770°C). [109] Moreover, tungsten based materials are the only compounds which can be used as catalyst, co-catalyst, catalyst support and electrolyte. [51] Tungsten carbide has been widely investigated since Levy and Boudart [110] reported that the electronic structure of WC is similar to that of Pt. Low price and resistance toward catalyst poisons have further encouraged research on the development of tungsten carbide and it is therefore the most investigated of the carbides for catalytic reactions.

Electrochemical properties of catalysts strongly depend on surface condition and composition, which are closely related with synthesis route. Many preparation methods for tungsten carbides are reported in literature including direct reaction of solid carbon or carbonaceous gases with tungsten metal or oxide. Traditional methods as these, however, lead to low surface area carbides, and furthermore high temperatures are needed for sufficient diffusion rates within the solid. [111] Improvements in catalytic activity can be achieved by preparation of high surface area structures or reduction of the particle size. Therefore studies on the preparation of carbides are now focused on the ability to achieve nanoscale particle sizes, high surface areas and porous structure. [112, 113, 114, 115, 116] One method to prepare high surface area carbides is by use of mesoporous templates. Ordered mesoporous materials prepared using hard templating methods are attracting attention in the field of ma-

terial science. However, these methods are challenging for the preparation of carbides due to collapse of the mesostructural regularity when caburizing directly from WO_3. [109, 112] Volpe and Boudart [117] demonstrated that the high surface areas could be retained when introducing an additional synthesis step by first converting WO_3 into W_2N which was then converted into WC by the temperature programmed reaction (TPR) method. Also Hara *et al.* [114] reported higher surface area carbides with improved catalytic activity when preparing WC from W_2N which was prepared from WO_3, than with prepared WC obtained from direct carburization of WO_3 with CH_4. [60]

Prepared non-precious catalysts have so far almost exclusively been evaluated in three electrode cells with aqueous alkaline or acid electrolytes, however, if they are to be implemented in electrochemical cell stacks, it is *via* porous gas diffusion electrodes. Especially implementation in fuel cells have been encouraged, and lately research has shifted toward demonstrating the viability of tungsten carbide for example as anode catalyst material in PEM fuel cells. [118] The best fuel cell performance using a tungsten carbide anode catalyst as has been obtained by Yang and Wang in a H_2/air single cell at 80°C and 3 atm. They reported a current density of 0.9 A cm^{-2} with a catalyst loading of 0.5 mg cm^{-2}. [119]
WC was also demonstrated as a support material in fuel cell electrodes. M. Shao *et al.* [120] tested for the first time WC as support material for Pt. Pt catalyst supported on WC showed similar or slightly better activity than Pt supported on carbon. Importantly, it was reported that Pt/WC only lost 4% of the activity after 300 potentiometric cycles, while Pt/C lost more than 20% of its activity. [121]
Tungsten carbides have long been known to be active for the hydrogen evolution reaction (HER). They have been extensively studied, and are among the most promising alternatives to platinum for this reaction. [51, 122] First investigations were performed by Bianchi *et al.* [123] who pioneered extensive studies.

Only very few evaluations of tungsten carbide have been performed above 100°C, while the activity is expected to increase with temperature. [52, 124, 125] For instance, the performance of WC at temperatures up to 150°C was investigated by Nikiforov *et al.* [124], who demonstrated that the HER activity of WC increases significantly with temperature, and that this effect is more pronounced than for Pt. For fuel cells at intermediate temperatures, Muroyama *et al*. [52] demonstrated the viability of WC as anode catalyst (2.5 mg cm^{-2}). Using a CsH_2PO_4/SiP_2O_7 electrolyte (thickness ca. 1.3 mm) high OCVs were reported and fuel cell current densities up to 15 mA cm^{-2} were achieved at 200°C. They reached a power density of 4.1 mW cm^{-2} compared to 1.3 mW cm^{-2} which was obtained using a commercial WC.

In this work carbides were prepared from mesoporous precursors and commercial WO_3 by carburization with methane or ethane. The present work makes use of mesoporous WO_3 and W_2N *i.e.* mWO_3 and mW_2N as which were prepared by Simon Meyer (Technical University

of Munich). mWO_3 was made by nanocasting by impregnation of a mesoporous silica (KIT-6) with ammonium metatungstate followed by calcinations. mW_2N was obtained by ammonolysis of the resulting powder. TEM images of the precursors mWO_3 (top) and mW_2N (bottom) are presented in Appendix B, Figure B.2. The image of mWO_3 suggests an ordered structure with rods of around 9-10 nm in thickness. In the image obtained for W_2N, there is no clear sign of an ordered structure. However, the particle sizes appears somewhat smaller, in the area of 5 nm. The characterization of the carbides as catalysts for hydrogen oxidation reaction (HOR) and HER by use of a solid electrolyte, CsH_2PO_4, and a liquid electrolyte, H_3PO_4. For comparison a commercial carbide and carbide prepared within the PROCON project are also investigated.

8.2 Experimental

8.2.1 Preparation of carbides

Six different tungsten carbides were used are used in this chapter. Two kinds of tungsten carbide powders were obtained from the precursors mWO_3 and mW_2N by treatment with a mixture of 25% CH_4 in H_2. Prior to carburization the precursors were treated with HF to remove the silica. HF and water were added to the silicate containing compounds, and the solutions were centrifuged at 5000 rpm and afterwards the liquid was collected. This procedure was repeated three times. Infra red (IR) spectra (Figure B.1 in Appendix B) indicated that all silica had been removed. For comparison of methane and ethane carburizing agents, treatment was performed on commercial WO_3 (Aldrich 99%) with methane as above, and with 12.5% ethane in H_2 at 900°C for 3 h with a flow rate of 200 mL min^{-1}. WC (Aldrich 99%) was used as received and WC-05-VN was obtained from A. L. T. Garica prepared using a carbon black template as described in [126]. Table 8.1 summarizes the carbides used in this chapter.

Table 8.1: *The table summrizes the prepared tungsten carbides. m, for example in mWO_3, indicates 'mesoporous'. [z]Prepared by Antonio Luis Tomas Garcia, *prepared from carbon black template, **prepared from KIT-6 template.*

Sample name	Precurser	Carburizing agent
WC (Aldrich)	NA	Methane
WC-WO_3	WO_3 (Aldrich)	Methane
WC-05-VN^z	$W_2N^{z,*}$	Methane
WC-mWO_3	mWO_3**	Methane
WC-mW_2N	mW_2N**	Methane
WC-ethane	WO_3(Aldrich)	Ethane

8.2.2 Physical characterizations

X-ray diffraction patterns and TEM images were achieved as described in Chapter 3. For BET surface area determination a Micromeritics Autochem 2910 was used. The powders

were placed on a quartz wool bed in a U-shaped quartz tube. The surface areas were determined at -196°C using a 30% mixture of nitrogen in helium. Adsorption/desorption was repeated three times, desorption peaks were used to calculate the surface area.

8.2.3 Electrochemical characterizations

Electrochemical measurements in phosphoric acid were carried out in 100% H_3PO_4 in a polytetrafluoroethylene (PTFE) half-cell assembly (as described in [126]). The electrode was prepared by using Toray paper substrate onto which an ink containing the carbide and ethanol was dispersed to a loading of around 13 mg cm^{-2}. A platinum wire was used as counter electrode. This was fixed around the capillary tip of the reversible hydrogen reference electrode, which was situated on the top of the carbide layer and the cell was placed in an oven with controlled temperature. For electrochemical measurements the cell was heated to the working temperature under a hydrogen gas flow (100 mL min^{-1}) through the back electrode chamber. For measurements of specific activity, steady state polarizations were performed when the temperature and OCV had stabilized, with a scan rate of 0.05 V s^{-1} and electrochemical impedance spectra were recorded at OCV in a frequency range of 10^4 to 10^{-2} Hz.

CsH_2PO_4 was used as electrolyte for electrochemical measurements at 250°C. Electrochemical hydrogen evolution measurements using CsH_2PO_4 were carried out with MEAs prepared as MEA **B** (Section 5.1.3, Figure 5.1) using a platinum electrode (Toray), CsH_2PO_4 electrolyte (0.6 mm thickness) and a tungsten carbide-based electrode. The tungsten carbide based anodes were prepared by dispersing a mixture of the carbide and CsH_2PO_4 (10:1 wt%) in ethanol onto the GDL (Toray for HER measurements and Ta for HOR measurements) with a WC loading of 10 mg cm^{-2}. Hydrogen evolution polarization curves were performed by applying hydrogen humidified to a dew point of 75°C to both electrodes. Fuel cell polarization curves were performed by applying humidified hydrogen to one electrode and humidified air to the other.

8.3 Results and discussion

8.3.1 Physical characterizations of prepared tungsten carbides

XRD

Figure 8.1 shows the x-ray diffraction patterns of WC Aldrich, the prepared carbides, WC-mW_2N and WC-mWO_3, and mW_2N. Sharp peaks are observed for commercial tungsten carbide, while broader peaks are observed for WC-mWO_3, WC-mW_2N and WC-ethane indicating smaller crystallite sizes. A challenge in the catalyst preparation is to obtain phase pure tungsten carbide, the product may consist of WC mixed with WO_x, W_2C, WC_{1-x} and W metal. [127] From the x-ray diffraction patterns of the prepared carbides, it appears that the major phase is WC as indexed with main crystalline phases.

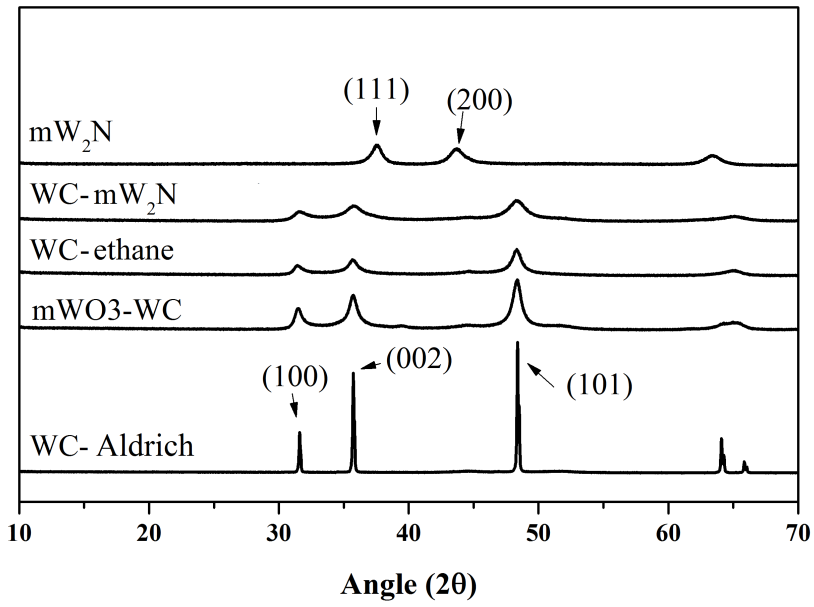

Figure 8.1: *XRD profiles of WC-Aldrich, WC-mW_2N, WC-mWO_3, WC-ethane and mW_2N. The main crystallite phases are indexed.*

TEM

Figure 8.2 shows the TEM images of WC-mW_2N, WC-mWO_3 and WC-ethane. It appears that the WC-mWO_3 consists of finely dispersed particles in sizes of around 20 nm, while WC-mW_2N appears rods-like with thicknesses of around 10 nm surrounded by amorphous carbon layer. WC-ethane consists of particles with sizes around 20 nm.

This tendency is in good agreement with formerly reported literature, for instance Claridge *et al.* [128] reported that the use of nitride precursor or ethane as carburizing agent increased the surface area of the carbides, compared to surface areas achieved when carburizing WO_3. Actually, the carbides synthesized with ethane were in their work found to give higher surface areas than carbides synthesized from nitrides, though the crystallinity of the carbides synthesized from nitrides was superior.

Specific activity and surface area

Table 8.2 summarizes the specific surface areas of the carbides and the precursors, as well as the measured specific activities obtained from the steady state measurements in phosphoric acid at 185°C (not shown).

It was not possible to measure neither the BET area of the commercial WC powder nor the commercial WO_3, probably because of the low surface areas. The BET areas of the mesoporous precursors, mW_2N and mWO_3 are relatively high, 49 and 43 $m^2\ g^{-1}$, respectively. Unfortunately no BET area was provided for the WC-O5-VN precursor. The BET areas for

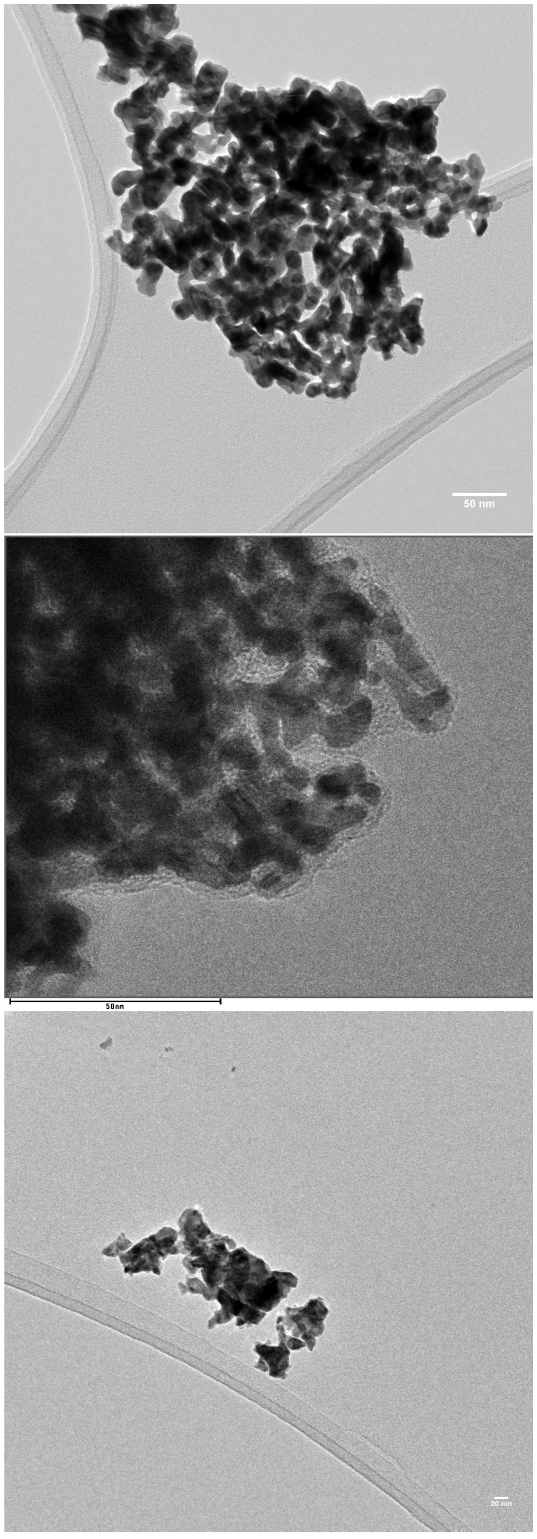

Figure 8.2: *TEM images of top: WC-mWO_3 (scalebar 50 nm); middle: WC-mW_2N (scalebar 50 nm); and below: WC-ethane (scalebar 20 nm).*

the carbides were measured as 31, 6, 18 and 12 $m^2\ g^{-1}$ for the WC-05-VN, WC-mWO_3, WC-mW_2N and WC-ethane, respectively. This suggests that the BET areas of the carbides

prepared from the two step oxide to nitride to carbide route (WC-05-VN and WC-mW_2N) yields higher surface areas, according to the discussion above.

Table 8.2: *BET areas of precursors and carbides, and specific activities measured in phosphoric acid at 185°C.*

Sample	**BET area of precursor (m^2 g^{-1})**	**BET area (m^2 g^{-1})**	**Specific activity at -100 mV (A g^{-1})**
WC-Aldrich	-	-	0.08
WC-comWO_3	-	-	0.36
WC-05-VN	-	31	18.73
WC-mWO_3	43	6	1.5
WC-mW_2N	49	18	2.08
WC-ethane	-	12	10.7

Apart from the WC-mW_2N sample, the specific activities measured for the carbides increases with increasing BET surface area. A very low activity was measured for WC-Aldrich, 0.08 A g^{-1} at -100 mV, whereas the activities increases in turn for WC-mWO_3, WC-mW_2N, WC-ethane and WC-05-VN. According to Table 8.2 these were measured as 1.5, 2.08, 10.7 and 18.73 A g^{-1}, respectively.

Figure 8.3 shows the activities vs. the BET areas for the five carbides. In principle, the activity should be proportional to the catalyst active area. As mentioned above, apart from the WC-mW_2N, the activity increases with surface area. Assuming that WC-Aldrich, WC-mWO_3, WC-ethane and WC-05-VN follows a linear increase, a higher activity could be expected from WC-mW_2N which is clearly deviating. From the TEM images, it appeared that the WC was surrounded by an amorphous phase which is expected to be carbon, which may lower the specific activity. Furthermore the BET measurements may be influenced by the amorphous carbon layer. In [126] and [129] the influence of excess carbon on the BET areas was discussed, and it was stated that even a small amount of carbon can result in a higher BET area than actual active area. The amount of excess carbon strongly depends on the synthetic history, but will not be discussed further here.

Hydrogen evolution and oxidation using H_3PO_4

Hydrogen evolution polarization curves for the WC-electrodes with WC loadings of 10 mg cm^{-2} in phosphoric acid at 185°C are shown in Figure 8.4 All measurements have been iR corrected by use of impedance. At 185°C no clear HER activity was found for WC-Aldrich at -100 mV. HER activity was induced by using tungsten carbide synthesized from mesoporous precursors. *E.g.* for WC-mW_2N for driving a cathodic current density of 1 A g^{-1}, an overpotential of 77 mV is required. These results imply that faster electron transfer may occur on WC-mW_2N than WC-Aldrich. As was discussed above based on the BET measurements, the activity of WC-mW_2N was expected to be higher, however a carbon surface layer may hinder the increase in activity. For WC-ethane and WX-05-VN the activities appear higher, for example for WC-ethane and overpotential of 49 mV is required to drive a

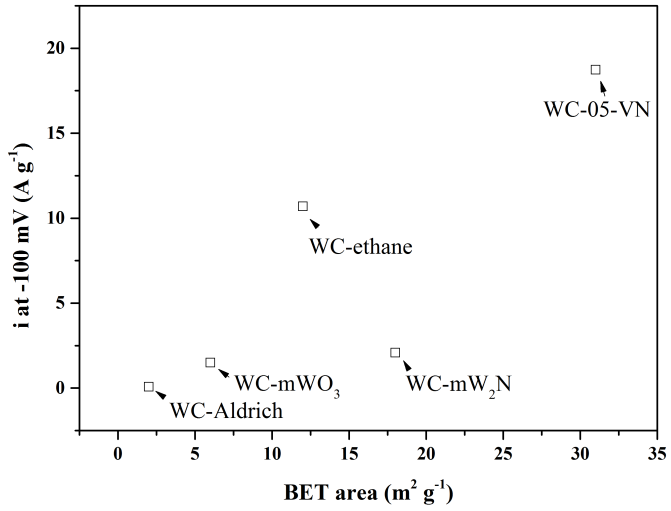

Figure 8.3: *Specific current density of HER at -100 mV vs. RHE as a function of sample BET area.*

cathodic current of 1 A g^{-1}.

Figure 8.4 also shows the hydrogen oxidation reaction (HOR) potentials. These activities are clearly lower than the HER activities. The most active appears to be WC-ethane, followed by WC-05-VN, while WC-mW_2N, WC-mWO_3 and WC-Aldrich shows no significant oxidation currents at these potentials.

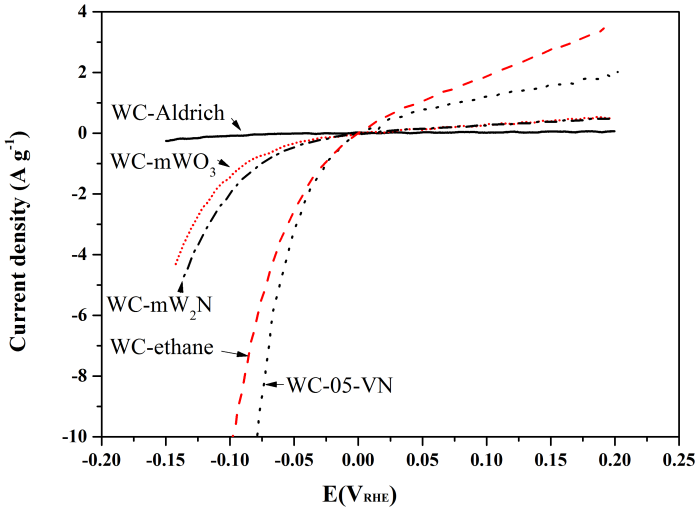

Figure 8.4: *Hydrogen evolution and oxidation polarization curves (corrected for iR) for the tungsten carbides, WC-Aldrich, WC-mW_2N, WC-mWO_3, WC-ethane and WC-05-VN recorded at 185°C in liquid H_3PO_4 electrolyte. WC loading=10 mg cm^{-2}.*

Hydrogen evolution and oxidation using CsH_2PO_4

Figure 8.5 shows the iR corrected hydrogen evolution polarization curves obtained at 250°C for the WC|CsH_2PO_4|Pt MEAs. Also in this system, all the prepared carbides shows higher cathodic currents than WC-Aldrich. WC-ethane appears has the highest activity, while WC-mW_2N, WC-mWO_3 and WC-05-VN are somewhat similar. The asymmetry in HOR/HER on the WCs both in phosphoric acid and in the solid acid system is not well-understood. The same behavior was reported by Papandrew *et al.* [55] for a nickel catalyst, and it was discussed whether the asymmetry could be ascribed to mass transport limitation or the blocking of binding sites for the dissociative adsorption of hydrogen on the catalyst surface. For clarification of this, more detailed mechanistic studies are required.

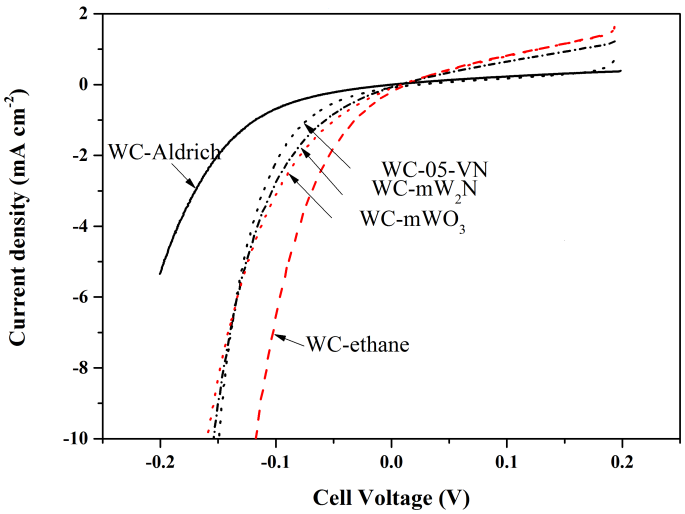

Figure 8.5: *Hydrogen evolution and oxidation polarization curves (corrected for iR) for experimental WC-Aldrich, WC-mW_2N, WC-mWO_3, WC ethane and WC-05-VN-based electrodes recorded at 250°C with solid CsH_2PO_4 electrolyte with H_2/H_2 at 75°C dew point. WC and Pt loadings of 10 and 7 mg cm^{-2} were used, respectively.*

Figure 8.6 shows the long term hydrogen evolution current of a WC-mW_2N|CsH_2PO_4|Pt MEA. The evolution current is stable for more than 90 hours at 250°C. There is a slight increase in the evolution current throughout the experiment. This may be due to hydration of the electrolyte. During the experiment some water may adsorb on the surface contributing to a somewhat increase in conductivity. Throughout the experiment there were small fluctuations in the steady state current. It is likely that these occurred due to water condensation and evaporation in the test hardware. Thus it seems that the carbide is stable under these conditions. Stability is of key importance for the catalyst materials. Tungsten carbide is considered stable, though some concern has been raised on the stability of WC in aqueous solutions. It has been reported to undergo continuous oxidation and covers with an insulating layer of WO_3. [130] Zellner *et al.* [118] investigated the electrochemical stability of

WC and W_2C in acidic solutions. They found that WC is stable, while W_2C is not. The MEA measured in this work remained stable throughout the experiment for almost 100 h.

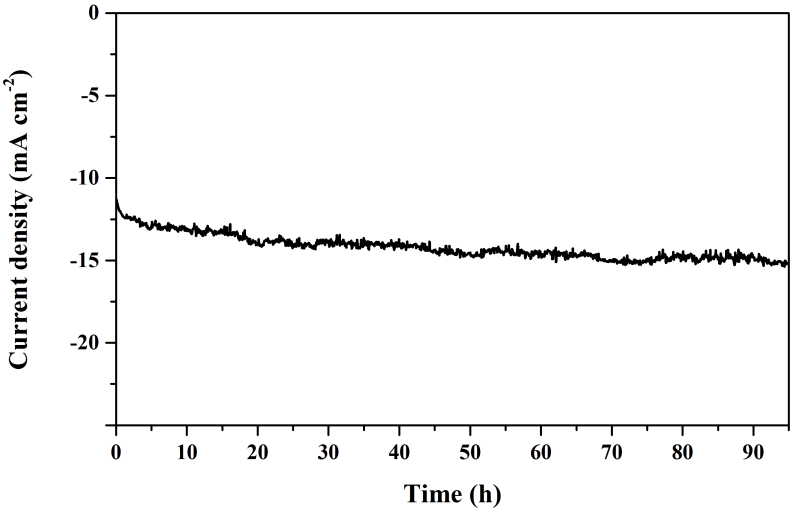

Figure 8.6: *Long term hydrogen evolution current of the experimental WC-mW$_2$N\|CsH$_2$PO$_4$\|Pt MEA at 250°C in H$_2$/H$_2$ at 75°C dew point and -0.2 V working electrode potential. WC and Pt loadings=10 and 7 mg cm^{-2}, respectively.*

Fuel cell polarization curves were performed with WC|CsH$_2$PO$_4$|Pt MEAs at different temperatures and with different catalyst loadings. In preliminary experiments (not shown) the fuel cell performance was found to increase in turn with WC loading. For the measurements presented in this chapter, a loading of 10 mg cm^{-2} was used. No optimization was performed, though a higher loading and optimization of the catalytic composition is expected to increase the fuel cell performance. Current densities at 0.6 V and 250, 260 and 270°C are presented in Table 8.3 along with maximum power densities. Examples of polarization curves are shown in Figure 8.7. The fuel cell performances were as expected increasing with temperature. The highest performances were achieved at 270°C, where WC-ethane and WC-05-VN perform significantly better than WC-mWO$_3$ and WC-mW$_2$N. The same trend as was seen in Figure 8.4. Power densities were calculated as 8.2, 7.4, 3.1 and 2.6 for WC-ethane, WC-05-VN, WC-mWO$_3$ and WC-mW$_2$N, respectively. Considering formerly reported literature on WC in intermediate temperature fuel cells, these results are encouraging. As was mentioned in the introduction of this chapter, Muroyama *et al.* [52] demonstrated at fuel cell using WC as anode material. They reached a current density of around 15 mA cm^{-2} and a maximum power density of 4.1 mW cm^{-2} at 200°C, though in a different system.

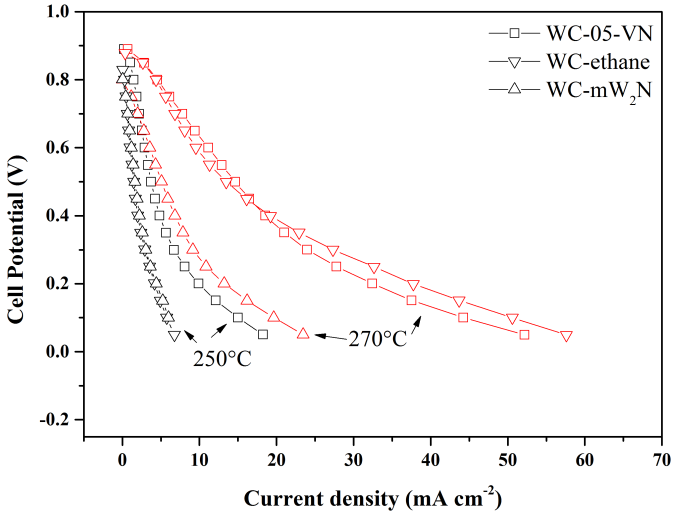

Figure 8.7: *Examples of polarization curves obtained using prepared WC(WC-05-VN, WC-mW$_2$N or WC-ethane)|CsH$_2$PO$_4$|Pt MEAs in H$_2$/air at 250°C. p_{H_2O}=0.3 atm. WC loading=10 mg cm^{-2}; Pt loading=7 mg cm^{-2}; Electrolyte thickness=0.6 mm.*

Table 8.3: *Current densities at 0.6 V at 250, 260 and 270°C in H$_2$/air cells. p(H$_2$O)=0.3 atm; WC loading=10 mg cm^{-2}; Pt loading=7 mg cm^{-2}; Electrolyte thickness=0.6 mm.*

Sample	**250°C mA cm^{-2}**	**260°C mA cm^{-2}**	**270°C mA cm^{-2}**	**Power density (270°C) mW cm^{-2}**
WC-05-VN	2.9	5.9	11.1	7.4
WC-mW$_2$N	1.6	2.4	4.2	2.7
WC-mWO$_3$	1.2	1.7	3.5	3.1
WC-ethane	1.0	2.6	9.5	8.2

Chapter 9

Overall Discussion

9.1 Overall Discussion

Fuel cells are widely known and the technology has been investigated and developed for several decades. Different types exist, *e.g.* polymer electrolyte membrane (PEM) fuel cells operating below 200°C and solid oxide fuel cells (SOFCs) above 500°C. Both technologies are promising as they are effective, well developed and the polymer and oxide electrolytes enable compact designs. Material issues such as use of expensive catalysts at low temperatures and material instability at high temperatures invite to the entering of a new technology. If a fuel cell is operated at temperatures intermediating those of PEM and SOFC, it may become possible to use novel catalysts, while still having a broad choice of construction materials.

For this work set-up was made for the electrochemical measurements. Kapton® HN, which was found stable in the temperature range of interest (<400°C), was used as gas sealing and electrical insulation. Tantalum coated flowplates and gas diffusion layers for the cathode side were used to avoid corrosion. The tantalum coatings had the additional advantage of extremely low interfacial corrosion resistance. For the electrodes, high platinum loadings facilitated contact between the electrodes and electrolyte, however further optimization of the catalyst composition in the electrolytes would significantly improve cell properties. The set-up was built so that the cell could be operated up to 400°C with non-stabilized electrolyte thicknesses down to 200 μm.

The finding of a sufficiently working electrolyte *i.e.* one that has high conductivity and at the same time mechanical strength, for intermediate temperatures has been the objective of research within the field for decades. Breakthroughs in the intermediate temperature technology were achieved by high performance fuel cell demonstrations reported by the groups of Haile [21] and Hibino [27] using CsH_2PO_4 and $Sn_{0.9}In_{0.1}P_2O_7$ electrolytes, respectively. For both systems the fuel cell performances were limited by the slow cathode kinetics, and stability was hindered by poor mechanical properties of the electrolytes. In this work, a cell was made confirming the results reported for CsH_2PO_4. CsH_2PO_4 undergoes a phase transition at 230°C where above a highly conducting phase is stable in a narrow temperature depending on the water partial pressure. The necessity of using composite electrolytes was highlighted, as for stability measurements pellet electrolytes of more than half a millimeter

were used as also reported by the group of Haile.

Following the demonstrations of high performance intermediate temperature fuel cells, vast amount of research has been reported on composite formation with solid acids. Improvements of properties can be achieved including mechanical stability, conductivity and water retention. In general, three types of solid acid based composites have been reported resulting in vast amount of research papers, however, only a few fuel cell demonstrations were reported.

In this work composites of CsH_2PO_4 with SiO_2, TiO_2 and ZrO_2 were investigated. Composite formation of CsH_2PO_4 with SiO_2 have previously been reported to increase the conductivity low temperatures (>150°C) with several orders of magnitude. In this work the possibility of using such composites in actual fuel cell applications was shortly addressed. The fuel cell measurements resulted in poor OCVs (below 0.3 V), probably due to the observed poor mechanical properties of the composites. Opposite, composites of CsH_2PO_4 with ZrO_2 and TiO_2 were found to have improved mechanical stabilities. Composites of CsH_2PO_4 and ZrO_2 were further investigated and found to improve densification of the electrolyte, indicated by SEM and improved OCV measurements. Furthermore, TGA measurements suggested improved water retention which was confirmed in the fuel cell experiments. It was possible to run a fuel cell at a lower water partial pressure, 0.12 atm compared to 0.3 atm which was used for CsH_2PO_4 alone. The cell was stable for more than 60 hours at 250°C. The physical stabilization of the superprotonic phase by composite formation with ZrO_2 enabled fuel cell measurements at 275°C reaching a current density of around 200 mA cm^{-2} and power density of around 40 mW cm^{-2}. Similar results were found for CsH_2PO_4/TiO_2 composites although this was not thoroughly studied.

CsH_2PO_4/$NdPO_4 \cdot 0.5H_2O$ composites were prepared, and the conductivity of the composites was found to increase by several orders of magnitude below the phase transition temperature of CsH_2PO_4. It was discussed whether this increase was due to a liquid layer of $CsH_5(PO_4)_2$ formed at the interphases as confirmed by XRD, or if newly established hydrogen bonds contributed. It is likely that both effects have an influence, however to present any conclusion on this topic, further investigations must be conducted. The prepared composite pellets were mechanically strong and dense, which facilitated high and stable OCVs, more than 0.9 V was measured for more than 12 hours at 235°C. Fuel cell polarization curves were performed at various temperatures, all characterized by being controlled by ohmic resistance. Accordingly, the fuel cell performance is expected to increase with decreasing ohmic resistance in the electrodes and electrolyte.

By forming composites with materials which are carrying basic sites, it may be possible to enable acid base interactions *via* hydrogen bonds. In this work, composites of CsH_2PO_4 with melamine cyanurate were investigated. The conductivity was found to increase in the entire temperature range of investigation thus indicating such interactions. Further inves-

tigations on this mechanism is of particular interest as the electrolytes were found to have both improved mechanical properties as well as high conductivities.

These investigations confirms that there are unexplored possibilities for CsH_2PO_4 as an intermediate temperature fuel cell electrolyte. The mechanical stability appears to be critical for the fuel cell performance, in composite with mechanically strong materials including ZrO_2, TiO_2 and $NdPO_4{\cdot}0.5H_2O$ good and stable fuel cell performances were achieved, while poor, or no performance was achieved for the CsH_2PO_4/SiO_2 composite.

Niobium based phosphates and bismuth phosphates were investigated as novel electrolytes. The niobium phosphates were found to have high conductivities, above 10^{-2} S cm^{-1}, and high OCVs and good EMF measurements indicated that the conductivity was protonic.
For cell measurements it was not possible to measure neither OCV nor EMF for the pure electrolytes. Instead these were strengthened by addition of PBI. For niobium phosphate a high amount of PBI, 20 wt% was used, which enabled stable measurements, however, even with such a high amount of PBI, the OCVs still dropped significantly with temperature. It was not fully investigated what caused the drop in OCV. It is possible that the mechanical stability of the electrolyte decreased with temperature, and additionally, electrodes of low Pt loadings, 0.7 mg cm^2 were used without optimization in the electrode/electrolyte contact. In general, it was found possible to form new proton conducting electrolytes for the intermediate temperature range, properties were enhanced by composite formation with a polymer, which are promising as they are known to enable the fabrication of dense and thin membranes. Naturally, considerations must be addressed to the electrodes for the demonstration of a full performing fuel cell. In this work, a low loading of only 0.7 mg cm^{-2} was used, which was in other experiments found to have an influence on the contact between electrodes and electrolyte.

Tungsten carbide is the most well investigated anode catalyst alternative to platinum in PEM fuel cells. In this work, tungsten carbides were prepared *via* different routes. The effect of using templates was investigated by preparing carbides by use of mesoporous silica and carbon black templates. The templates were impregnated with tungsten oxides and methane was used as carburizing agent. Additionally it was investigated whether there was an effect of using ethane as carburizing agent compared to methane, and therefore a commercial WO_3 was carburized by both. For comparison of the prepared carbides, a commercial tungsten carbide was investigated. The activities for the hydrogen evolution reaction (HER) were determined in phosphoric acid at 185°C. Apart from the WC-mW_2N they increased with the measured BET surface areas. The deviation of WC-mW_2N was expected to be due to an amorphous carbon layer as also indicated by TEM. BET areas were measured as 6, 12, 18 and 31 m^2 g^{-1}, and the activities were measured 1.5, 2.07, 10.7 and 18.73 A g^{-1} at -100 mV for WC-mWO_3, WC-ethane, WC-mW_2N and WC-05-VN, respectively. Thereby all the prepared carbides induced a higher performance than the commercial carbide, where

neither a surface area nor an activity could be measured. The HER activities were furthermore measured at 250°C using a CsH_2PO_4 electrolyte. Such cell was stable during the entire experiment which lasted more than 90 hours.
The carbides were furthermore investigated as anode catalysts in fuel cells at 250, 260 and 270°C. The measured current densities were as could be expected found to be strongly dependent on temperature. The highest power densities were found at 270°C as 8.2, 7.4, 3.1 and 2.7 mW cm^{-2} for WC-ethane, WC-05-VN, WC-mWO_3 and WC-mW_2N, respectively, in agreement with the order of activity for HOR which was measured in phosphoric acid.
These investigations of tungsten carbide catalysts thereby suggest that it may become possible to prepare high surface area carbides, which are active and stable for the hydrogen evolution and hydrogen oxidation reactions.

These investigations have considered most parts of a fuel cell, from hardware, electrolyte, platinum based electrodes and non-noble catalysts. They suggest that it is possible to fabricate high performance fuel cells with stable composite electrolytes, low platinum loading, or non-noble catalysts at intermediate temperatures using hydrogen or other fuels. Promising demonstrations have been performed, however, the full potential of an intermediate temperature fuel cells is yet to be seen.

Chapter 10

Conclusion and Outlook

10.1 Conclusions

A purpose build set-up was fabricated and operational in the temperature interval from room temperature and up to 400°C. The tantalum coated flowplates and GDLs were extremely corrosion resistant, and the interfacial contact resistance (ICR) of tantalum coated layers were found as 1.3 mΩ cm^2 *i.e.* far below the DOE target value. Anodizations in phosphoric acid at 2 V did not increase the ICR.

Measurements using CsH_2PO_4-based MEAs confirmed formerly reported literature of the material as a potential solid electrolyte for intermediate temperature fuel cells. High platinum loadings of 7 mg cm^{-2} were used to facilitate contact between electrolyte and electrodes. Major drawbacks of the pure CsH_2PO_4 electrolyte were found to be poor mechanical properties, narrow temperature range of operation and necessity of humidification.

Developments of the CsH_2PO_4 electrolyte were made by composite formations. Composite formation of CsH_2PO_4 with SiO_2 did not result in good OCVs, these were below 0.3 V and unstable. Improvements of the properties of CsH_2PO_4 were achieved by composite formation with oxides including ZrO_2 and TiO_2. The composite of $2CsH_2PO_4/1ZrO_2$ was stable at 250°C with low water partial pressures, down to 0.12 atm, and operational up to 275°C. At 275°C current and power densities of 200 mA cm^{-2} and more than 40 mW cm^{-2} were measured, respectively.
Composite formation of CsH_2PO_4 with $NdPO_4{\cdot}0.5H_2O$ resulted in mechanically improvement of the electrolyte leading to a high OCV>0.9 V which was stable for more than 12 hours. The proton conductivity of the composite was confirmed by EMF and fuel cell demonstrations. Fuel cells were measured up to 285°C, where the highest performance was achieved as 27.7 mA cm^{-2}.
CsH_2PO_4 composite formation with melamine cyanurate resulted in increased conductivities in the entire temperature range from 120 to 260°C. Importantly the conductivities above the phase transition temperature of CsH_2PO_4 were increased probably due to the establishment of hydrogen interactions. The highest conductivity was measured as 0.18 S cm^{-1} at 250°C.

Niobium and bismuth phosphates were investigated as novel electrolytes. They were found to have high and stable conductivities and it was therefore attempted to fabricate electro-

chemical cells. The pure phosphates suffered from poor mechanical properties and PBI was added in order to achieve stable OCVs. OCVs of 0.75 and 0.8 V were measured for niobium and bismuth phosphate with 5 and 20% PBI added, respectively. For the niobium phosphate measured EMF values were furthermore found to be in good agreement with theoretical values.

Mesoporous tungsten oxide was used as precursor for tungsten carbide formation, and resulted in a BET area of 6 m^2 g^{-1}. By introducing an additional synthesis step by first converting WO_3 into W_2N the BET area of the resulting carbide increased to 18 m^2 g^{-1}. Carburization of commercial WO_3 with methane and ethane were compared and resulted in a BET area 12 m^2 g^{-1} for that carburized by ethane, while no value could be measured for that carburized by methane. An additional carbide (WC-05-VN) with a BET area of 31 m^2 g^{-1} was investigated.

Activity measurements for the hydrogen evolution reaction performed in H_3PO_4 suggested improved activities in the order WC-Aldrich < WC-mWO_3 < WC-mW_2N < WC-ethane < WC-05-VN. The activities were measured as 0.08, 1.5, 2.08, 10.7 and 18.73 A g^{-1}, respectively. Based on the BET measurements, a higher activity could be expected for WC-mW_2N. An amorphous carbon surface layer visible in the TEM images may have hindered this. An asymmetry was observed in HER/HOR activities, as those of HER were significantly higher than those of HOR. The HOR activity was highest for the WC-ethane.

Demonstrations of tungsten carbides as hydrogen evolution and oxidation catalysts at higher temperatures were performed with CsH_2PO_4 as solid electrolyte. Promising results were achieved for the carbides, both as reduction and oxidation catalysts and a stable hydrogen evolution measurement was measured at 250°C for more than 100 h at 250°C, indicating stability of the carbide under these conditions.

Fuel cell polarization curves were performed at 250, 260 and 270°C. The fuel cell performance was found to increase with temperature. In agreement with measurements performed in phosphoric acid highest powder densities were achieved for WC-ethane. The maximum power densities were calculated at 270°C as 8.2, 7.4, 3.1 and 2.7 mW cm^{-2} for WC-ethane, WC-05-VN, WC-mWO_3 and WC-W_2N, respectively.

10.2 Outlook

Following the introduction from Norby of a 'gab' *i.e.* the lack of a sufficiently conducting electrolyte for intermediate temperatures (*ca.* 200-400°C), research of electrolytes for this temperature range expanded. Electrolytes found for this temperature area include phosphates which generally suffer from poor mechanical properties and one of the main obstacles which remains to be overcome is the fabrication of a highly conducting mechanically strong thin layer electrolyte with sufficient compatibility with the other materials used. A few fuel cell demonstrations have been performed in this temperature range and for the

realization of such cells, major emphasis must be put on the fabrication of a full cell.

Emphasis has in formerly reported literature and in this work been on the preparation of composites. Hard materials such as ZrO_2, TiO_2 and Al_2O_3 can be fabricated into mechanically strong layers for example as a 3D porous network wherein the proton conducting phase can be incorporated. The fabrication of a fuel cell using such electrolyte is still to be demonstrated. For CsH_2PO_4/$NdPO_4$ composites the mechanism responsible for the large increase in conductivity must be further clarified to be fully understood and further used. Composites with organic compounds should be further investigated since organic compounds have been proven to enable fabrication of thin layer electrolytes and this remains to be done.

Screenings have been performed by our and other research groups in order to suggest novel electrolytes. The electrolytes chosen from such screenings were found to fulfill the main criteria, high conductivity. However, for the practical use of novel materials, research remain to be done. For new electrolytes to be implemented in the fuel cell system, more careful synthesis must be performed.

For the commercialization of fuel cells and electrolyzers, the amount of the expensive platinum must be lowered. In this work tungsten carbide was investigated as catalyst for the hydrogen oxidation reaction and hydrogen evolution reaction. As the surface area of commercial tungsten carbide is very low, the carbides were prepared with the aim of achieving higher BET areas using different routes. Improvements of synthesis are still to be made, for example, the structural regularities seen for the precursors were lost in the carbides. The mechanism of carbide formation has been studied, but is however still not fully understood, and parameters not mentioned here, excess carbon, flow rates, synthesis temperature are expected to have an influence on the final catalyst activity.
Ethane was compared to methane as carburizing agent and the surface area was increased additionally. Ethane is interesting as a carburizing and it is expected that by use of this the synthesis temperature can be lowered.
For cell demonstrations, unsupported carbides were used as catalysts and an optimization in the catalytic layer and establishment of contact with the electrolyte is expected to further improve the cell performance.
It was chosen to study tungsten carbide, however, various of other interesting materials are to be investigated for potential use as catalysts.

Major reasons for the intermediate temperature regime are the potential use of non-noble catalysts in combination with the possibility of using other fuels than hydrogen, unfortunately in this project only hydrogen fuel was used. The performance of intermediate temperature methanol fuel cell have in formerly reported literature been shown to approach those reported for direct methanol PEM fuel cells, and it would be of interest to study this further.

References

[1] http://www.kebmin.dk/klima-energi-bygningspolitik/dansk-klima-energi-bygningspolitik, .

[2] M. S. Dresselhaus and I. L. Thomas. Alternative energy technologies. *Nature*, **414**: 332–337, (2001).

[3] J. D. Holladay, J. Hu, D. L. King, and Y. Wang. An overview of hydrogen production technologies. *Catalysis Today*, **139**:244–260, (2009).

[4] http://www.ballard.com/files/pdf/media/the_fuel_cell_today_industry_review_2011.pdf, .

[5] http://nssdc.gsfc.nasa.gov/nmc/spacecraftDisplay.do?id=1965-068A, .

[6] http://www.netinform.net/h2/h2mobility/Detail.aspx?ID=278, .

[7] http://www.toyota-global.com/innovation/environmental_technology/fuelcell_vehicle/, .

[8] T. Norby. The promise of protonics. *Nature*, **410**:877–878, (2001).

[9] G. K. H. Shimizu, J. M. Taylor, and S. Kim. Proton conduction with metal-organic frameworks. *Science*, **341**:354–355, (2013).

[10] J. M. Pringle, P. C. Howlett, D. R. MacFarlane, and M. Forsyth. Organic ionic plastic crystals: recent advances. *Journal of Materials Chemistry*, **20**:2056–2062, (2010).

[11] http://www.ballard.com/fuel-cell-applications/distributed-generation.aspx, .

[12] http://www.horizonfuelcell.com/#!minipak/c156u, .

[13] James Larminie and Andrew Dicks. *Fuel Cell Systems Explained*. Wiley, England, 2nd edition, 2003. ISBN 978-0-470-84857-9.

[14] J. S. Wainright, J.-T. Wang, D. Weng, R. F. Savinell, and M. Litt. Acid-doped polybenzimidazoles: A new polymer electrolyte. *Journal of The Electrochemical Society*, **142**:L121–L123, (1995).

[15] T. Norby. Solid-state protonic conductors: principles, properties, progress and prospects. *Solid State Ionics*, **125**:1–11, (1999).

[16] O. Paschos, J. Kunze, U. Stimming, and F. Maglia. A review on phosphate based, solid state, protonic conductors for intermediate temperature fuel cells. *Journal of Physics: Condensed Matter*, **23**:234110–, (2011).

[17] D.A. Boysen, T. Uda, C. R. I. Chisholm, and S. Haile. High-performance solid acid fuel cells through humidity stabilization. *Science*, **303**:68–70, (2004).

[18] M. Nagao, T. Kamiya, P. Heo, A. Tomita, T. Hibino, and M. Sano. Proton Conduction in In^{3+}-Doped SnP_2O_7 at Intermediate Temperatures. *Journal of the Electrochemical Society*, **153**:A1604–A1609, (2006).

[19] S. M. Haile, D. A. Boysen, C. R. I. Chisholm, and R. B. Merle. Solid acids as fuel cell electrolytes. *Nature*, **410**:910–913, (2001).

[20] J. Otomo, T. Tamaki, S. Nishida, S. Wang, M. Ogura, T. Kobayashi, C.-Ju Wen, H. Nagamoto, and H. Takahashi. Effect of water vapor on proton conduction of cesium dihydrogen phosphate and application to intermediate temperature fuel cells. *Journal of Applied Electrochemistry*, **35**:865–870, (2005).

[21] T. Uda and S. M. Haile. Thin-membrane solid-acid fuel cell. *Electrochemical and Solid-State Letters*, **8**:A245–A246, (2005).

[22] `USPatentSpecificationAppl.Publ.2005221143Al20051006,.`

[23] Y. Jin, Y. Shen, and T. Hibino. Proton conduction in metal pyrophosphates (MP_2O_7) at intermediate temperatures. *Journal of Materials Chemistry*, **20**:6214–6217, (2010).

[24] M.-V. Le, D.-S. Tsai, C.-Y. Yang, W.-H. Chung, and H.-Y. Lee. Proton conductors of cerium pyrophosphate for intermediate temperature fuel cell. *Electrochimica Acta*, **56**:6654–6660, (2011).

[25] S. Wang X. Sun, Z. Wang, X. Ye, T. Wen, and F. Huang. Proton conductivity of CeP_2O_7 for intermediate temperature fuel cells. *Solid State Ionics*, **179**:1138–1141, (2008).

[26] X. Wu, A. Verma, and K. Scott. A Sb-doped SnP_2O_7 solid proton conductor for intermediate temperature fuel cells. *Fuel Cells*, :453–458, (2008).

[27] P. Heo, H. Shibata, M. Nagao, Hibino T, and M. Sano. Performance of an intermediate temperature fuel cell using a proton-conducting $Sn_{0.9}In_{0.1}P_2O_7$ electrolyte. *Journal of The Electrochemical Society*, **153**:A897–A901, (2006).

[28] P. Heo, N. Kajiyama, K. Kobayashi, M. Nagao, M. Sano, and T. Hibino. Proton conduction in $Sn_{0.95}Al_{0.05}P_2O_7$-PBI-PTFE composite membrane. *Electrochemical and Solid-State Letters*, **11**:B91–B95, (2008).

[29] T. Matsui, S. Takeshita, Y. Iriyama, T. Abe, M. Inaba, and Z. Ogumi. Proton conductivity of $(NH_4)_2TiP_4O_{13}$-based material for intermediate temperature fuel cell. *Electrochemitry Communications*, **6**:180–182, (2004).

[30] S. Haufe, D. Prochnow, D. Schneider, O. Geier, D. Freude, and U. Stimming. Polyphosphate composite: conductivity and NMR studies. *Solid State Ionics*, **176**: 955–963, (2005).

[31] T. Uma, H. Y. Tu, D. Freude, D. Schneider, and U. Stimming. Characterisation of intermediate temperature polyphosphate composites. *Journal of Materials Science*, **40**:227–230, (2005).

[32] T. Matsui, N. Kasuza, Y. Kato, Y. Iriyama, T. Abe, K. Kikuchi, and Z. Ogumi. Effect of pyrophosphates as supporting matrices on proton conductivity for NH_4PO_3 composites at intermediate temperatures. *Journal of Power Sources*, **171**:483–488, (2007).

[33] C. Sun and U. Stimming. Synthesis and characterization of NH_4PO_3 based composite with superior proton conductivity for intermediate temperature fuel cells. *Electrochimica Acta*, **53**:6417–6422, (2008).

[34] T. Matsui, T. Kokino, R. Kikuchi, and K. Eguchi. Intermediate-temperature fuel cell employing CsH_2PO_4/SiP_2O_7-based composite electrolytes. *Journal of The Electrochemical Society*, **153**:A339–A342, (2006).

[35] V. G. Ponomareva and G. V. Lavrova. Influence of dispersed TiO_2 on protonic conductivity of $CsHSO_4$. *Solid State Ionics*, **106**:137–141, (1998).

[36] V. G. Ponomareva, B. V. Merinov, and V. V. Dolbinina. Composite protonic electrolytes in the system $(NH_4)_3H(SO_4)_2$-SiO_2. *Solid State Ionics*, **145**:205–210, (2001).

[37] V. G. Ponomareva and G. V. Lavrova. The investigation of disordered phases in nanocomposite proton electrolytes based on $MeHSO_4$ (Me = Rb, Cs, K). *Solid State Ionics*, **145**:197–204, (2001).

[38] V.G. Ponomareva and E.S. Shutova. High-temperature behavior of CsH_2PO_4 and CsH_2PO_4-SiO_2 composites. *Solid State Ionics*, **178**:729–734, (2007).

[39] N. K. Beck and L. C. De Jonghe. Proton conduction in SnP_2O_7-LaP_3O_9 composite electrolytes. *Electrochemical and Solid State Letters*, **12**:B11–B13, (2009).

[40] Y. Jin, K. Fujiwara, and T. Hibino. High temperature, low humidity proton exchange membrane based on an inorganic-organic hybrid structure. *Electrochemical and Solid-State Letters*, **13**:B8–B10, (2010).

[41] Y. Jin and T. Hibino. A proton-conducting composite membrane: $Sn_{0.95}Al_{0.05}P_2O_7$. *Electrochimica Acta*, **55**:8371–8375, (2010).

[42] N. Kitamura, K. Amezawa, Y. Tomii, and N. Yamamoto. Protonic conduction in rare earth orthophosphates with the monazite structure. *Solid State Ionics*, **162**:161–165, (2003).

[43] G. Harley, R. Yu, and L. C. De Jonghe. Proton transport paths in lanthanum phosphate electrolytes. *Solid State Ionics*, **178**:769–773, (2007).

[44] V. Nalini, R. Haugsrud, and T. Norby. Defects and transport properties of Sr-doped LaP_3O_9. *Solid State Ionics*, **181**:1264–1269, (2010).

[45] T. Norby and N. Christiansen. Proton conduction in Ca- and Sr-substituted $LaPO_4$. *Solid State Ionics*, **77**:240–243, (1995).

[46] K.-D. Kreuer. Proton conductivity: Materials and applications. *Chem. Mater.*, **8**: 610–641, (1996).

[47] R. Lan and S. Tao. Conductivity of new pyrophosphate $Sn_{0.9}Sc_{0.1}(P_2O_7)_{1-\delta}$ prepared by an aqueous solution method. *Journal of Alloys and Compounds*, **486**:380–385, (2009).

[48] S. Tao. Conductivity of SnP_2O_7 and In-doped SnP_2O_7 prepared by an aqueous solution method. *Solid State Ionics*, **180**:148–153, (2009).

[49] T. Uda, D. A. Boysen, C. R. I. Chisholm, and S. M. Haile. Alcohol fuel cells at optimal temperatures. *Electrochemical and Solid-State Letters*, **9**:A262–A264, (2006).

[50] S. Fukuzumi, H. Kotani, H. R. Lucas, K. Doi, T. Suenobu, R. L. Peterson, and K. D. Karlin. Mononuclear copper compex-catalyzed four-electron reduction of oxygen. *Journal of the American Chemical Society*, **132**:6874–6875, (2010).

[51] E. Antolini and E. R. Gonzales. Tungsten-based materials for fuel cell applications. *Applied Catalysis B: Environmental*, **96**:245–266, (2010).

[52] H. Muroyama, K. Katsukawa, T. Matsui, and K. Eguchi. Tungsten-based carbides as anode for intermediate-temperature fuel cells. *Journal of The Electrochemical Society*, **158**:B1072–B1075, (2011).

[53] P. Heo, M. Nagao, M. Sano, and T. Hibino. A high-performance Mo_2C-ZrO_2 anode catalyst for intermediate-temperature fuel cells. *Journal of The Electrochemical Society*, **154**:B53–B56, (2007).

[54] P. Heo, H. Shibata, M. Nagao, and T. Hibino. Pt-free intermediate-temperature fuel cells. *Solid State Ionics*, **179**:1446–1449, (2008).

[55] A. B. Papandrew and T. A. Zawodzinski Jr. Nickel catalysts for hydrogen evolution from CsH_2PO_4. *Journal of Power Sources*, **245**:171–174, (2014).

[56] E. Antolini and E. R. Gonzales. Ceramic materials as supports for low-temperature fuel cell catalysts. *Solid State Ionics*, **180**:746–763, (2009).

[57] Y. J. Huang, Q. Li, C. Pan, T. Anfimova, J. O. Jensen, and N. J. Bjerrum. Metal phosphates as intermediate temperature proton conducting electrolytes. *ECS Transactions*, **45**:99–104, (2012).

[58] A. Heinzel and V. M. Barragán. A review of the state-of-the-art of the methanol crossover in direct methanol fuel cells. *Journal of Power Sources*, **84**:70–74, (1999).

[59] X. Ren, M. S. Wilson, and S. Gottesfeld. High performance direct methanol polymer electrolyte fuel cells. *Journal of The Electrochemical Society*, **143**:l2–L15, (1996).

[60] M. K. Neylon, S. Choi, H. Kwon, K. E. Curry, and L. T. Thompson. Catalytic properties of early transition metal nitrides and carbides: n-butane hydrogenolysis, dehydrogenation and isomerization. *Applied Catalysis A General*, **183**:253–263, (1999).

[61] S. Brunauer, P. H. Emmett, and E. Teller. Adsorption of gases in multimolecular layers. *Journal of the American Chemical Society*, **60**:309–319, 1938.

[62] Peter J. Goodhew, John Humphreys, and Richard Beanland. *Electron microscopy and analysis*. Taylor and Francis, New York, 3 edition, 2001. ISBN 0-203-18425-4.

[63] Southampton Electrochemistry Group. *Instrumental methods in electrochemistry*. E. Horwood, Chichester, 6th edition, 2001. ISBN 9781898563808.

[64] M. Kouril, E. Christensen, C. Pan, S. Eriksen, and B. Gillesberg. Corrosion rate of construction materials in hot phosphoric acid with contribution of anodic polarization. *Materials and Corrosion*, **63**:310–316, (2012).

[65] A. Adamson. *Physical chemistry of surfaces*. Wiley, New York, 6th ed. edition, 1997. ISBN 9780471148739.

[66] A. Berman, C. Drummond, and J. Israelachvili. Amonton's law at the molecular level. *Tribology Letters*, **4**:95–101, 1998.

[67] K. Feng, Z. Li, X. Cai, and P. K. Shu. Corrosion behavior and electrical conductivity of niobium implanted 316L stainless steel used as bipolar plates in polymer electrolyte membrane fuel cells. *Surface and Coatings Technology*, **205**:85–91, (2010).

[68] M. P. Brady, H. Wang, J. A. Turner, H. M. Meyer, K. L. More, P. F. Tortorelly, and B. D. McCarthy. Pre-oxidized and nitrided stainless steel alloy foil for proton exchange membrane fuel cell bipolar plates: Part 1. corrosion, interfacial contact resistance, and surface structure. *Journal of Power Sources*, **195**:5610–5618, (2010).

[69] S. Lecuyer, A. Quemerais, and G. Jezequel. Composition of natural oxide-films on polycrystalline tantalum using xps electron take-off angle experiments. *Surface and Interface Analysis*, **18**:257, (1992).

[70] K. Shimizu, G. M. Brown, H. Habazaki, K. Kobayashi, P. Skeldon, G. E. Thompson, and G. C. Wood. Direct observation of anodic films formed on tantalum in concentrated phosphoric and sulphuric acid solutions. *Corrosion Science*, **40**:963–973, (1998).

[71] J. Ribeiro and A. R. De Andrade. Characterization of RuO_2-Ta_2O_5 coated titanium electrode - microstructure, morphology, and electrochemical investigation. *Journal of The Electrochemical Society*, **151**:D106–D112, (2004).

[72] A. Kraytsberg, M. Auinat, and Y. Ein-Eli. Reduced contact resistance of PEM fuel cell's bipolar plates via surface texturing. *Journal of Power Sources*, **164**:697–703, (2007).

[73] Martin Kalmar Hansen. PEM Water Electrolysis at Elevated Temperatures. *PhD Thesis*, (2012).

[74] X. Chen, C. Wang, E. A. Payzant, C. Xia, and D. Chu. An oxide ion and proton co-ion conducting $Sn_{0.9}In_{0.1}P_2O_7$ electrolyte for intermediate-temperature fuel cells. *Journal of the Electrochemical Society*, **155**:B1264–B1269, (2008).

[75] Y. k. Taninouschi, T. Uda, Y. Awakura, A. Ikeda, and S. Haile. Dehydration behavior of the syperprotonic conductor CsH_2PO_4 at moderate temperatures: 230 to 260 °C. *Journal of Materials Chemistry*, **17**:3182–3189, (2007).

[76] J. Otomo, N. Minagawa, C. ju Wen, K. Eguschi, and H. Takahashi. Protonic conduction of CsH_2PO_4 and its composite with silica in dry and humid atmospheres. *Solid State Ionics*, **156**:357–369, (2003).

[77] S. M. Haile, C.R.I. Chisholm, K. Sasaki, D.A. Boysen, and T. Uda. Solid acid proton conductors: from laboratory curiosities to fuel cell electrolytes. *Faraday Discussions*, **134**:17–39, (2007).

[78] J. Zhang, Y. Tang, C. Song, J. Zhang, and H. Wang. PEM fuel cell open circuit voltage (OCV) in the temperature range of 23 °C to 120 °C. *Journal of Power Sources*, **163**:532–537, (2006).

[79] A. B. Papandrew, C. R. I. Chisholm, R. A. Elgammal, M. Ösera, and S. K. Zecevic. Advanced electrodes for solid acid fuel cells by platinum deposition on CsH_2PO_4. *Chemistry of Materials*, **23**:1659–1667, (2011).

[80] Á. Varga, N. A. Brunelli, M. W. Louie, K. P. Giapis, and S. M. Haile. Composite nanostructured solid-acid fuel cell *via* electrospray deposition. *Journal of Materials Chemistry*, **20**:6309–6315, (2010).

[81] A. G.-Urtiga, K. Scott, S. Cavaliere, D. J. Jones, and J. Rosiére. A new fabrication method of an intermediate temperature proton exchange membrane by the electrospinning of CsH_2PO_4. *Journal of Materials Chemistry A*, **1**:10875, (2013).

[82] A. B. Yaroslavtsev. Modification of solid state proton conductors. *Solid State Ionics*, **176**:2935–2940, (2005).

[83] H. Iwahara, T. Esaka, H. Uchida, and N. Maeda. Proton conduction in sintered oxides and its application to steam electrolysis for hydrogen production. *Solid State Ionics*, **3**:359–363, (1981).

[84] H. Iwahara, T. Yajima, T. Hibino, K. Ozaki, and H. Suzuki. Protonic conduction in calcium, strontium and barium zirconates. *Solid State Ionics*, **61**:65–69, (1993).

[85] V. G. Ponomareva, N. F. Uvarov, G. V. Lavrova, and E. F. Hairetdinov. Composite protonic solid electrolytes in the $CsHSO_4$-SiO_2 system. *Solid State Ionics*, **90**:161–166, (1996).

[86] A.I. Baranov, V.V. Grebenev, A.N. Khodan, V.V. Dolbinina, and E.P. Efremova. Optimization of superprotonic acids salts for fuel cell applications. *Solid State Ionics*, **176**:2871–2874, (2005).

[87] P. Bocchetta, R. Ferraro, and F. D. Quarto. Advances in anodic alumina membranes thin film fuel cell: CsH_2PO_4 pore filler as proton conductor at room temperature. *Journal of Power Sources*, **187**:49–56, (2009).

[88] G.V. Lavrova, E.S. Shutova, V.G. Ponomareva, and L.A. Dunyushkina. Proton conductivity and interphase interaction in CsH_2PO_4-$SrZrO_3$ composites. *Russian Journal of Electrochemistry*, **49**:801–807, (2013).

[89] S. y. Oh, I. K. Insani, V. H. Nguyen, G. Kawamura, H. Muto, M. Sakai, and A. Matsuda. CsH_2PO_4-$H_3PW_{12}O_{40}$ composites as proton-conducting electrolytes for fuel

cell systems in a dry atmosphere. *Science and Technology of Advanced Materials*, **12**:1–6, (2011).

[90] J. Otomo, T. Ishigooka, T. Kitano, H. Takahashi, and H. Nagamoto. Phase transition and proton transport characteristics in csh_2po_4/sio_2 composites. *Electrochimica Acta*, **53**:8186–8195, (2008).

[91] T. Anfimova, Q. Li, and N. J. Bjerrum. Thermal stability and proton conductivity of rare-earth orthophosphate hydrates. *International Journal of Electrochemical Science*, **9**:2285–2300, (2014).

[92] J. B. Davis, D. B. Marshall, and P. E. D. Morgan. Monazite-containing oxide/oxide composites. *Journal of the European Ceramic Society*, **20** :583–587, (2000).

[93] Q. Li, R. He, J. O. Jensen, and N. J. Bjerrum. Approaches and recent development of polymer electrolyte membranes for fuel cells operating above 100 °C. *Chem. Mater.*, **15**:4896–4915, (2003).

[94] G. Qing, R. Kikuchi, A. Takagaki, T. Sugawara, and S. T. Oyama. CsH_2PO_4/polyvinylidene flouride composite electrolytes for intermediate temperature fuel cells. *Journal of The Electrochemical Society*, **161**:F451–F457, (2014).

[95] S. y Oh, G. Kawamura, H. Muto, and A. Matsuda. Mechanochemical synthesis of proton conductive composites derived from cesium dihydrogen phosphate and guanine. *Solid State Ionics*, **225**:223–227, (2012).

[96] S. y Oh, G. Kawamura, H. Muto, and A. Matsuda. Anhydrous protic conduction of mehcanochemically synthesized $CsHSO_4$-Azole-derived composites. *Electrochimica Acta*, **75**:11–19, (2012).

[97] Y. Huang, Q. Li, A. H. Jensen, M. Yin, J. O. Jensen, E. Christensen, C. Pan, N. J. Bjerrum, and W. Xing. Niobium phosphates as an intermediate temperature proton conducting electrolyte for fuel cells. *Journal of Materials Chemistry*, **22**:22452, (2012).

[98] Y. Huang, Q. Li, T. V. Anfimova, E. Christensen, M. Yin, J. O. Jensen, N. J. Bjerrum, and W. Xing. Indium doped niobium phosphates as intermediate temperature proton conductors. *International Journal of Hydrogen Energy*, **38**:2464–2470, (2013).

[99] I. Nowak and M. Ziolek. Niobium compounds: Preparation, characterization, and application in heterogeneous catalysis. *Chemical Reviews*, **99**:3603–3624, (1999).

[100] S. Okazaki, M. Kurimata, T. Iizuki, and T. Tanabe. The effect of phosphoric-acid treatment on the catalytic property of niobic acid. *Bulletin of the Chemical Society Japan*, **60**:37–41, (1987).

[101] M. Cantero, L. M. Real, S. Bruque, M. M. Lara, and J. R. R. Barrado. Proton conduction in some acid niobium phosphates. *Solid State Ionics*, **51**:273–279, (1992).

[102] Z. Chai, C. Wang D. Dong, H. Zhang, P. A. Webley, D. Zhao, and H. Wang. Nanoporous niobium phosphate electrolyte membrane for low temperature fuel cell. *Journal of Membrane Science*, **356**:147– 153, (2010).

[103] Y. Shen, K. Kojima, M. Nishida, P. Heo, K. H. Choi, H. Chang, and T. Hibino. Proton conduction in $A^{III}_{0.5}B^{V}_{0.5}P_2O_7$ compounds at intermediate temperatures. *Journal of Materials Chemistry*, **22**:14907–14915, (2012).

[104] Y. Shen, P. Heo, C. Pak, H. Chang, and T. Hibino. Intermediate-temperature, non-humidified proton exchange membrane fuel cell with a highly proton-conducting $Fe_{0.4}Ta_{0.5}P_2O_7$ electrolyte. *Electrochemistry Communications*, **24**:82–84, (2012).

[105] M. Nagao, A. Takeuchi, P. Heo, T. Hibino, M. Sano, and A. Tomita. A Proton-Conducting In^{3+}-Doped SnP_2O_7 Electrolyte for Intermediate Temperature Fuel Cells. *Electrochemical and Solid-State Letters*, **9**:A105–A109, (2006).

[106] P. Heo, M. Nagao, T. Kamiya, M. Sano, A. Tomita, and T. Hibino. $Sn_{0.9}In_{0.1}P_2O_7$-based organic/inorganic composite membranes - application to intermediate temperature fuel cells. *Journal of The Electrochemical Society*, **154**:B63–B67, (2007).

[107] Y. Jiang, X. Xu, R. Lan, L. Zhang, and S. Tao. Stability and conductivity of NH_4PO_3-PTFE composites at intermediate temperatures. *Journal of Alloys and Compounds*, **480**:874–877, (2009).

[108] S. A. Grigoriev, P. Millet, and V. N. Fateev. Evaluation of carbon supported Pt and Pd nanoparticles for the hydrogen evolution reaction in PEM water electrolysers. *Journal of Power Sources*, **177**:281–285, (2008).

[109] Z. Wu, Y. Yang, D. Gu, Q. Li, D. Feng, Z. Chen, B. Tu, P. A. Webley, and D. Zhao. Silica-templated synthesis of ordered mesoporous tungsten carbide/graphitic carbon composites with nanocrystalline walls and high surface areas via a temperature-programmed carburization route. *small*, **23**:2738–2749, (2009).

[110] R. B. Levy and M. Boudart. Platinum-like behavior of tungsten carbide in surface catalysis. *Science*, **181**:547–549, (1973).

[111] S. Decker, A. Löfberg, J.-M. Bastin, and A. Frennet. Study of the preparation of bulk tungsten carbide catalysts with C_2H_6/H_2 and C_2H_4/H_2 carburizing mixtures. *Catalysis Letters*, **44**:229–239, (1997).

[112] X. Cui, H. Li, L. Guo, D. He, H. Chen, and J. Shi. Synthesis of mesoporous tungsten carbide by an impregnation-compaction route, and its NH_3 decomposition catalytic activity. *Dalton Transactions*, :6435–6440, (2008).

[113] X. Cui, X. Zhou, H. Chen, Z. Hua, H. Wu, Q. He L. Zhang, and J. Shi. *In-Situ* carbonization synthesis and ethylene hydrogenation activity of ordered mesoporous tungsten carbide. *International Journal of Hydrogen Energy*, **36**:10513–10521, (2011).

[114] Y. Hara, N. Minami, and H. Itagaki. Synthesis and characterization of high-surface area tungsten carbides and application to electrocatalytic hydrogen oxidation. *Applied Catalysis A: General*, **323**:86–93, (2007).

[115] L. Hu, S. Ji, T. Xiao, C. Guo, P. Wu, and P. Nie. Preparation and characterization of tungsten carbide confined in the channels of SBA-15 mesoporous silica. *Jornal of Physical Chemistry B*, **111**:3599–3608, (2007).

[116] C. Ma, N. Brandon, and G. Li. Preparation and formation mechanism of hollow microspherical tungsten carbide with mesoporosity. *Journal of Physical Chemistry C*, **111**:9504–9508, (2007).

[117] L. Volpe and M. Boudart. Compounds of molybdenum and tungsten with high specific surface area. *Journal of Solid State Chemistry*, **59**:332–347, (1985).

[118] M. B. Zellner and J. G. Chen. Potential application of tungsten carbides as electrocatalysts: Synergistic effect by supporting Pt on C/W(110) for the reactions of methanol, water and CO. *Journal of The Electrochemical Society*, **152**:A1483–A1494, (2005).

[119] X. G. Yang and C. Y. Wang. Nanostructured tungsten carbide catalysts for polymer electrolyte fuel cells. *Applied Physics Letters*, **86**:224104–1–3, (2005).

[120] Y. Shao, J. Liu, Y. Wang, and Y. Lin. Novel catalyst support materials for PEM fuel cells: current status and future prospects. *Journal of Materials Chemistry*, **19**:46–59, (2009).

[121] Y. Liu and W. E. Mustain. Evaluation of tungsten carbide as the electrocatalyst support for platinum hydrogen evolution/oxidation catalysts. *International Journal of Hydrogen Energy*, **37**:8929–8938, (2012).

[122] R. D. Armstrong and M. F. Bell. Tungsten carbide catalysts for hydrogen evolution. *Electrochimica Acta*, **23**:1111–1115, (1978).

[123] G. Bianchi, F. Mazza, and S. Trasatti. Anodic behavior and passivity of some interstitial niobium, tantalum, titanium and tungsten compounds. *Zeitschrift Fur Physikalische Chemie*, **226**:40–58, (1964).

[124] A. V. Nikiforov, I. M. Petrushina, E. Christensen, N. V. Alexeev, A. V. Samokhin, and N. J. Bjerrum. WC as non-platinum hydrogen evolution electrocatalyst for high temperature PEM water electrolyzers. *International Journal of Hydrogen Energy*, **37**:18591–18597, (2012).

[125] E. Antolini and E. R. Gonzalez. Tungsten-based materials for fuel cell applications. *Applied Catalysis B*, **96**:245–266, (2010).

[126] A. L. T. Garcia, Q. Li, J. O. Jensen, and N. J. Bjerrum. High surface area tungsten carbides: Synthesis, characterization and catalytic activity towards the hydrogen evolution reaction in phosphoric acid at elevated temperatures. *International Journal of Electrochemical Science*, **9**:1016–1032, (2014).

[127] Z. Yan, M. Cai, and P. K. Shen. Nanosized tungsten carbide synthesized by a novel route at low temperatures for high performance electrocatalysts. *Scientific Reports*, **3**:1–7, (2013).

[128] J. B. Claridge, A. P. E. York, A. J. Brungs, and M. L. H. Green. Study of the temperature-programmed reaction synthesis of early transition metal carbide and nitride catalyst materials from oxide precursers. *Chem. Mater*, **12**:132–142, (2000).

[129] A. T. L. Garcia. Transition metal carbides for high temperature pem water electrolysis. *PhD Thesis*, (2014).

[130] J. D. Voorhies. Electrochemical and chemical corrosion of tungsten carbide (WC). *Journal of The Electrochemical Society*, **119**:219–222, (1972).

Appendix A

Cell Construction - Appendix

In Chapter 4 the fabrication of the fuel cell was described. The endplates of the fuel cell were fabricated from a copper-aluminum alloy.
In the same chapter it was described that Kapton® HN was used as electrical insulation and gas sealing.
The datasheets for the copper aluminum alloy and Kapton® HN are attached in this Appendix.

COPPER ALLOY
JM 7

CuAl10Fe5Ni5-C

ÖREBRO - SWEDEN

Edition 8

Density 7,6

COMPOSITION

	Composition %								
	Cu	**Al**	**Fe**	**Ni**	**Mn**	**Pb**	**Si**	**Sn**	**Zn**
Nom	**80**	**10**	**5**	**5**					
Min	**Bal**	8,8 8,5*	3,5 3,5*	4,0 4,0*					
Max	**Bal**	10,5 11,0*	5,5 4,5*	6,0 6,0*	2,5	0,05	0,1	0,2	0,5

* JM7-20

MECHANICAL PROPERTIES

			Sandcast **JM7-03**	**Centrifugally- & continuously cast** **JM7-15**	**Extruded Rolled Forged** **JM7-20***
Rp0,2	Proof strength	N/mm^2	>=250	>=260	>=270
Rm	Tensile strenght	N/mm^2	>=540	>=590	>=630
A5	Elongation	%	>=10	>=10	>=10
HB	Hardness	10/1000	>=140	>=150	>=170
E	Young's modulus	N/mm^2	110 000	110 000	110 000
	Coeff. of thermal expansion	$X10^{-6}$,0-100°C	16,5	16,5	16,5
	Thermal conductivity	W/m °C	65	65	65
	Resistivity	nΩm,20°C	190	190	190
	Machinability		Good	Good	Good

*) JM7-20 is Johnson Metall's designation of material according to any of the standards shown below or equivalent standard.

Values given refer to separately cast test specimen to SIS 112152, or specimen cut from -15 castings or -20 material respectively with a wall thickness corresponding to the test specimen diameter.

Nearest equivalent standard				
Swedish standard	SS-EN 1982	CC333G-GS	CC333G-GC/GZ	
European standard	EN 1982	CC333G-GS	CC333G-GC/GZ	
US standard	UNS	C 95500	C 95500	C 63000
British standard (old)	BS	1400 AB2	1400 AB2	2872/2874, CA104
German standard (old)	DIN	1714, G-CuAl10Ni	1714, GZ/GC-CuAl10Ni	17665, CuAl10Ni

DuPont™ Kapton® HN

polyimide film

Technical Data Sheet

DuPont™ Kapton® HN general-purpose film has been used successfully in applications at temperatures as low as -269°C (-452°F) and as high as 400°C (752°F). HN film can be laminated, metallized, punched, formed or adhesive coated. Kapton® HN is the recommended choice for applications that require an all-polyimide film with an excellent balance of properties over a wide range of temperatures.

Applications

- Mechanical parts
- Electronic parts
- Electrical Insulation
- Pressure sensitive tape
- Fiber optics cable
- Insulation blankets
- Insulation tubing
- Automotive diaphragms sensors and manifolds
- Etching
- Shims

Product Specifications

Kapton® HN is manufactured, slit and packaged according to the product specifications listed in H-38479, Bulletin GS-96-7.

Certification

Kapton® HN meets ASTM D-5213 (type 1, item A) requirements.

DUPONT®

The miracles of science™

Table 1
Physical Properties of DuPont™ Kapton® HN at 23°C (73°F)

Property	Unit	1 mil 25µm	2 mil 50µm	3 mil 75µm	5 mil 125µm	Test Method
Ultimate Tensile Strength at 23°C, (73°F) at 200°C (392°F)	psi (MPa)	33,500(231) 20,000(139)	33,500(231) 20,000(139)	33,500(231) 20,000(139)	33,500(231) 20,000(139)	ASTM D-882-91, Method A*
Ultimate Elongation at 23°C, (73°F) at 200°C (392°F)	%	72 83	82 83	82 83	82 83	ASTM D-882-91, Method A
Tensile Modulus at 23°C, (73°F) at 200°C (392°F)	psi (GPa)	370,000 (2.5) 290,000 (2.0)	370,000 (2.5) 290,000 (2.0)	370,000 (2.5) 290,000 (2.0)	370,000 (2.5) 290,000 (2.0)	ASTM D-882-91, Method A
Density	g/cc	1.42	1.42	1.42	1.42	ASTM D-1505-90
MIT Folding Endurance	cycles	285,000	55,000	6,000	5,000	ASTM D-2176-89
Tear Strength-propagating (Elmendorf), N (lbf)		0.07 (0.02)	0.21 (0.02)	0.38 (0.02)	0.58 (0.02)	ASTM D-1922-89
Tear Strength, Initial (Graves), N (lbf)		7.2 (1.6)	16.3 (1.6)	26.3 (1.6)	46.9 (1.6)	ASTM D-1004-90
Yield Point at 3% at 23°C, (73°F) at 200°C (392°F)	MPa (psi)	69 (10,000) 41 (6,000)	69 (10,000) 41 (6,000)	69 (10,000) 41 (6,000)	69 (10,000) 41 (6,000)	ASTM D-882-91
Stress to produce 5% elong. at 23°C, (73°F) at 200°C (392°F)	MPa (psi)	90 (13,000) 61 (9,000)	90 (13,000) 61 (9,000)	90 (13,000) 61 (9,000)	90 (13,000) 61 (9,000)	ASTM D-882-92
Impact Strength at 23°C, (73°F)	N•cm•(ft lb)	78 (0.58)	78 (0.58)	78 (0.58)	78 (0.58)	DuPont Pneumatic Impact Test
Coefficient of Friction, kinetic (film-to-film)		0.48	0.48	0.48	0.48	ASTM D-1894-90
Coefficient of Friction, static (film-to-film)		0.63	0.63	0.63	0.63	ASTM D-1894-90
Refractive Index (sodium D line)		1.70	1.70	1.70	1.70	ASTM D-542-90
Poisson's Ratio		0.34	0.34	0.34	0.34	Avg. three samples, elongated at 5, 7, 10%
Low temperature flex life		pass	pass	pass	pass	IPC-TM-650, Method 2.6.18

*Specimen size 25 x 150 mm (1.6 in); jaw separation 100 mm (4 in), jaw speed, 50mm/min (2 in/min). Ultimate refers to the tensile strength and elongation measured at break.

Appendix B

Tungsten Carbide as Non-noble Catalyst - Appendix

In Chapter 8.1 tungsten carbides were investigated. Precursors prepared from silica templates were used for the preparation of two of the carbides (WC-mW_2N and WC-mWO_3). This Appendix presents the IR spectra and TEM images of the precursors.

B.1 SiO_2 removal with HF

IR spectra were made to see whether there was any SiO_2 left in the two precursors after treatment with hydrofluoric acid. IR measurements were carried out on a Biorad FTS 575C in the spectral range of 550-4000 cm^{-1} with a resolution of 0.5 cm^{-1}. The spectra were analyzed using WIN-IR Pro 2.7. These are presented in Figure B.1.

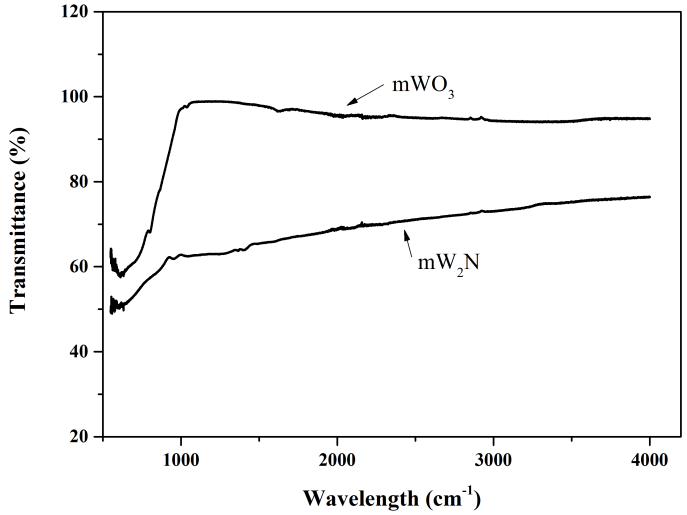

Figure B.1: *IR spectra of WO_3 and W_2N after treatment with hydrofluoric acid.*

B.2 TEM images of tungsten carbide precursors

Figure B.2 shows TEM images of the two precursors WO_3 and W_2N.

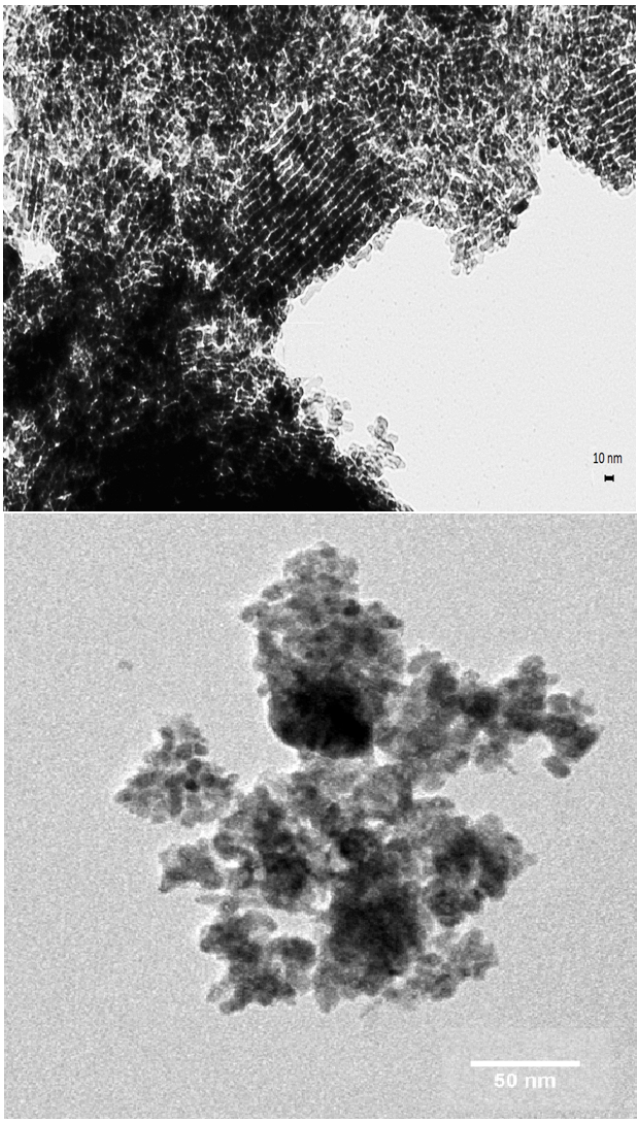

Figure B.2: *TEM images of mWO_3 and W_2N. Scale bars are indicated on the images. Kindly provided by Simon Meyer.*

Appendix C

List of Publications and Contributions

All publications conducted throughout the three years are listed below.

C.0.1 Publications

- "Contact Resistance of Tantalum Coatings in Fuel Cells and Electrolyzers using Acidic Electrolytes at Elevated Temperatures"
  Annemette Hindhede Jensen*, Erik Christensen and Jens von Barner, *ECS Electrochemistry Letters*, **3**, F50, (2014).

- "Intermediate Temperature Fuel Cell Using CsH_2PO_4/ZrO_2-Based Composite Electrolytes"
  Annemette Hindhede Jensen*, Qingfeng Li, Erik Christensen and Niels J. Bjerrum, *Journal of The Electrochemical Society*, **161**, F72 (2014).

- "$CsH_2PO_4/NdPO_4$ Composites as Proton Conducting Electrolytes for Intermediate Temperature Fuel Cells"
  Tatiana Anfimova, Annemette Hindhede Jensen, Erik Christensen, Jens Oluf Jensen, Niels J. Bjerrum, Qingfeng Li, *Journal of The Electrochemical Society* **162**, F1 (2015).

- "CsH_2PO_4/Melamine Cyanurate Composites for Intermediate Temperature Fuel Cell Applications"
  Annemette Hindhede Jensen*, Qingfeng Li**, Erik Christensen and Niels J. Bjerrum, to be submitted to *Journal of The Electrochemical Society*.

- "Tungsten carbide as electrocatalyst for fuel cells and electrolyzers"
  Annemette Hindhede Jensen, Simon Meyer, Antonio Luis Tomas Garcia, Erik Christensen, Klaus Köhler, Niels J. Bjerrum and Qingfeng Li, to be submitted to *Journal of The Electrochemical Society*.

- "Niobium phosphates as an intermediate temperature proton conducting electrolyte for fuel cells"
  Yunjie Huang, Qingfeng Li, Annemette Hindhede Jensen, Min Yin, Jens Oluf Jensen,

Erik Christensen, Chao Pan, Niels Bjerrum, Wei Xing, *Journal of Materials Chemistry*, **42**, 22452 (2012).

- "1,2,4-Triazolium perfluorobutanesulfonate as an archetypal pure protic organic ionic plastic crystal electrolyte for high temperature polymer electrolyte membrane fuel cells"
  Jiangshui Luo,* Annemette Hindhede Jensen, Neil R. Brooks, Jeroen Sniekers, David Aili, Qingfeng Li,* Martin Knipper, Bram Vanroy, Michael Wübbenhorst, Feng Yan, Luc Van Meervelt, Zhigang Shao, Jianhua Fang, Zheng-Hong Luo, Dirk E. De Vos, Koen Binnemans,* and Jan Fransaer*, Accepted in *Energy and Environmental Science*.

- "Electrodepositions on Tantalum in Alkali Halide Melts"
  Jens H. von Barner, Annemette Hindhede Jensen and Erik Christensen, *ECS Transactions*, **50**, 221 (2012).

C.0.2 Conference contributions

- "Fabrication and Characterizations of Materials and Components for Intermediate Temperature Fuel Cells and Water Electrolysers"
  Annemette Hindhede Jensen, Carsten Brorson Prag, Qingfeng Li, Erik Christensen, Niels Bjerrum, *International Symposium on Water Electrolysis and Hydrogen as part of the future Renewable Energy System*, Copenhagen, 2012. (Poster presentation).

- "Fabrication and characterization of proton conducting composite materials for electrolytes in intermediate temperature fuel cells and water electrolysers"
  Annemette Hindhede Jensen, Katrine Elsøe, Tatiana Anfimova, Erik Christensen, Jens H. von Barner and Niels Bjerrum, *3rd CARISMA International Conference on Medium and High Temperature Proton Exchange Membrane Fuel Cells*, Copenhagen 2012. (Poster presentation).

- "Niobium Phosphates as Intermediate Temperature Proton Conductor"
  Yunjie Huang, Qingfeng Li, Chao Pan, Jens Oluf Jensen, Erik Christensen, Lars Nilausen Cleeman, Annemette Hindhede Jensen, Tatiana Anfimova and Niels Bjerrum, *3rd CARISMA International Conference on Medium and High Temperature Proton Exchange Membrane Fuel Cells*, Copenhagen 2012. (Poster presentation).

- "Proton Conductive Niobium Phosphates as Electrolytes for Fuel Cells Operating with Renewable Biofuels"
  Yunjie Huang, Qingfeng Li, Tatiana Anfimova, Annemette Hindhede Jensen, Jens Oluf Jensen, Erik Christensen and Niels Bjerrum, , *Pacific Rim Meeting on Electrochemical and Solid-State Science*, Honolulu 2012, (Oral presentation/conference paper).

- "Interfacial Contact Resistance of Tantalum Coated Construction Materials for High Temperature Steam Electrolysers and Fuel Cells"
  Annemette Hindhede Jensen, Erik Christensen and Jens H. von Barner, *Pacific Rim Meeting on Electrochemical and Solid-State Science*, Honolulu 2012, (Poster presentation).

- "Fabrication and Characterization of Proton Conducting Phosphate Electrolytes for Intermediate Temperature Fuel Cell Assembling"
  Annemette Hindhede Jensen, Qingfeng Li, Tatiana Anfimova, Erik Christensen, Jens H. von Barner and Niels Bjerrum, *Nordic Conference on Ceramic and Glass Technology*, Roskilde 2012 (Oral presentation).

- "Physicochemical properties of 1,2,4-triazolium perfluorobutanesulfonate as an archetypal pure protic organic ionic plastic crystal electrolyte"
  Jiangshui Luo, Neil R. Brooks, Jeroen Sniekers, Annemette Hindhede Jensen, Qingfeng Li, Martin Knipper, Bram Vanroy, Michael Wübbenhorst, Chengzhen Shi, Feng Yan, Jianhua Fang, Luc Van Meervelt, Koen Binnemans and Jan Fransaer, , *Electrochemical Conference on Energy & the Environment* (Shanghai, 2014).